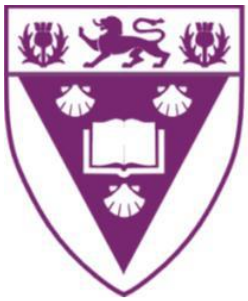

RHODES UNIVERSITY

Where leaders learn

Sulphide textures and compositions associated with the hydrothermal/magmatic system of the Twangiza gold deposit (South Kivu, DRC)

A thesis submitted in partial fulfilment of the requirements of the degree of

Master of Science

At

Rhodes University

By

Emmanuel Busane Aganze

Submitted in August 2018

Department of Geology, Rhodes University

South Africa

Supervisor: Prof. Steffen H. Büttner

Abstract

Twangiza mine is a gold deposit situated in the eastern Democratic Republic of Congo. The rock types at the Twangiza Mine consist of black shale, including carbonaceous mudstone and thin intercalated layers of siltstone, and feldspar-rich granitoid intrusive sills, referred to as albitite, folded into a major antiformal structure. The gold mineralization at the mine is commonly found associated with sulphides. The sulphide textures and compositions of mineralized and unmineralized samples of black shales, albitite sills and hydrothermal veins in the mine are considered for the understanding of the spatial association of gold with sulphides and gold mineralization history of the mine.

The sulphides within the Twangiza mine consist of pyrite, arsenopyrite, pyrrhotite, chalcopyrite and rare cobaltite.

The primary pyrite texture occurs in unmineralized black shale and is interpreted to be diagenetic. It consists of fine-grained anhedral pyrite crystals aggregating into spherical nodules and formed in replacement of organic material during the diagenesis process. The secondary pyrite textures resulted from the hydrothermal fluids activity and include (i) aggregates of annealed anhedral crystals into sulphide-rich lenses; (ii) elongated anhedral pyrite in the form of short stringers; (iii) fine-grained subhedral to euhedral pyrite randomly distributed within the rock matrix; (iv) euhedral zoned pyrite crystals occurring within veins; (v) aggregations of fine-grained anhedral pyrite, locally distributed in the matrix; (vi) abundant dissemination of fine-grained subhedral to anhedral pyrite crystals within the vein selvedge in the host rock; (vii) and coarse-grained massive pyrite bodies. The pyrite major elemental composition does not vary significantly in the different textures and sample types. The Fe content ranges from 44.57 to 46.40 wt. %, and the S content

ranges from 53.75 to 55.25 wt. %. Pyrite from mineralized black shale and hydrothermal veins contains relatively higher concentrations of As (~ 1 wt. %) than pyrite from other sample types.

The arsenopyrite commonly occurs as fine-grained anhedral crystals as inclusions within pyrite, medium-grained crystal intergrowing with pyrite and/or as coarse-grained massive arsenopyrite bodies in the massive sulphide veins. The arsenopyrite composition is uniform in all textural and sample type with Fe content ranging from 33.44 to 35.20 wt. %, S content ranging from 21.13 to 22.55 wt. % and As content ranging from 42.20 to 43.97 wt. %. In mineralized black shale and unmineralized black shale, the arsenopyrite shows, however, minor concentrations of Ni with 0.39 and 0.70 wt. % respectively.

The pyrrhotite occurs as fine-grained anhedral patchy crystals randomly distributed within the rock matrix of unmineralized black shale and unmineralized granitoid, and / or as inclusions within pyrite in mineralized granitoid. The pyrrhotite shows a uniform composition in all samples and textural types, though minor concentrations of Ni (2.06 wt. %) content are reported in unmineralized granitoid.

Chalcopyrite occurs as fine-grained crystals in inclusions within pyrite; and cobaltite occurs as rare fine-grained anhedral crystals occasionally disseminated in the albitite sill matrix. The chalcopyrite composition does not vary considerably in all sample and textural types, and cobaltite shows minor concentrations of Ni (4.55 wt. %) and Fe (3.45 wt. %).

Native gold grains are commonly found associated with the secondary pyrite texture especially within the sulphide-rich lenses and in the massive sulphide veins, and are almost pure with ~97 wt. %.

A Na-rich hydrothermal fluid from low-grade metamorphism associated with the E-W compressive tectonic event, which caused formation of the antiform structure which control the

mineralization in the deposit area, led to the albitization of the deposit rocks and specially the alteration of the granitic assemblage to form albitite, and the deposition of aggregates of fine-grained anhedral crystals and growth and annealing of pyrite in sulphide-rich lenses.

Afterward, the CO_2-rich hydrothermal fluids influx circulated through reactivated structures, including quartz veins, and led to the precipitation of dolomite, ankerite, siderite and magnesite. They also led to the precipitation of pyrite of secondary textures as well as arsenopyrite, chalcopyrite and formation of pyrrhotite from the desulphurization of early pyrite. The CO_2-rich hydrothermal fluids probably leached gold and other trace elements such as As, Co, etc. from the sedimentary host rocks and deposited them into suitable traps, such as the sulphide-rich lenses and massive sulphide bodies, preferably within the hinge zone of anticline axis constituting a hydrothermal fluid pathway.

Table of contents

List of Figures

List of Tables

ACKNOWLEDGEMENTS

I am most grateful to my supervisor Professor Steffen Büttner for his invaluable devotion to this work. His guidance, encouragement and permanent support were highly appreciated and led to the completion of this work.

Special thanks to all the Rhodes University geology department's staff, especially to Professor Jock Harmer, the director of Exploration and Economic Geology MSc program, Professor Haris Tsikos, Professor Steve Prevec, Mr. Mike Skinner and all visiting professors and expert professionals for the assistance and teaching. I am grateful to Mrs. Ashley Goddard for her constant support, but also to Mrs. Andrea King, Mr. Andile Pikoli, and Mr. Thulani Royi of the Thin Sectioning Laboratory, and Shirley Pinchuck and Marvin Randall of the Electron Microscopy Unit for their constant laboratory assistance and guidance.

I would also like to extend my gratitude to Banro Corporation, particularly to its subsidiary of Twangiza Mining SA for having provided me with the required samples for this study and for having organized my leave schedule to enable me to complete my Msc program.

Very special thanks to my wife Pascaline Andema MUHIGWA and my son Noah-Gabriel BUSANE Birimwiragi for their endless encouragements and endeavors consented throughout the period of this study. Special thanks go also to my parents BUSANE Chentwali and Nabintu BUHENDWA, my brothers and sisters, Lefranc Busane and Bertille Busane for your invaluable support, Wenceslas Busane, Lola Busane and Bellarmin Busane for your encouragements and support during this study.

My gratitude to Bubaka Rudahya, the Chief Mine Geologist of Twangiza Mining, for the constant encouragement and support.

Lastly, I would like to thanks the fellow candidates of the 2016-2017 MSc Exploration Geology class of Rhodes University with special regards to the late Moses Mkwizu for the time spent together sharing knowledge and experiences, may his soul rest in eternal peace. Special thoughts go also to Thapelo Moloto for the laboratory practices and shared knowledge.

I. INTRODUCTION

Twangiza mine is a gold deposit situated around 45 km to the south-southwest of Bukavu city in the South-Kivu Province of the Democratic Republic of Congo (Figure 1). The Twangiza deposit is currently mined by Twangiza Mining SA, a subsidiary of Banro Corporation, which is a Canadian company, holding permits in the area covering 1,164 km^2 (Rautenbach et al., 2011).

The Twangiza deposit was discovered in the 1950s by Minière des Grands Lacs (MGL) from an alluvial gold upstream investigation along the Mwana River. Banro Corporation acquired the control of the Twangiza property in 1996 after it had been explored by a number of companies such as Chartered Consolidated, SOMINKI and SAKIMA (Rautenbach et al., 2011). The estimated resources within the deposit are evaluated at 26.67 Mt @ 2.05g/t of mineral reserves and 99.35Mt @ 1.47 g/t of measured and indicated resources plus 9.38Mt @ 1.17 g/t of inferred resources (Banro, 2017).

The Twangiza deposit occurs along the core of an approximately 200 m wide antiformal structure oriented N-S and is subdivided into Main Pit, Central Pit and North Pit domains. Currently only the Main and the Central Pits are mined. The process plant started producing gold since October 2011 (commercial production) and its current operating capacity is 1.7 Mt per year (Banro, 2017).

The depositional age of the Twangiza deposit formations is of Neoproterozoic age. They are characterized by a sequence of black shales including thin intercalated siltstones layers and feldspar-rich porphyry intrusion sills, the latter referred to as albitites by Walemba (2001). Gold mineralization occurs within both lithological types. In either lithology it is associated with sulphides, but not all sulphide-bearing rocks are mineralized. High gold content is commonly found around intruded porphyry granitoids. The hydrothermal veins are abundant within the deposit, particularly in the axial zone of the antiform. Away from the fold core, gold grades drop, irrespective of the sulphide content of the rocks (Fall, 2007). However, the relationship between sulphide occurrence, hydrothermal activity, and gold mineralization remains poorly understood. Also the primary source, or sources, of gold in the Twangiza deposit have not been clearly identified.

Currently, few studies have been conducted in the area to define the mineralization process. Walemba (2001) identified four types of fluid inclusions in the area, H_2O-NaCl-CO_2-Salt; H_2O-NaCl-CO_2 and H_2O-NaCl-Salt; H_2O-NaCl, associated with two phases of gold mineralization and suggesting a range of fluids from meteoric to a mixture of meteoric and magmatic. In addition, a metasedimentary source of gold has been proposed by Buttner et al (2016) from isotopic analyses conducted on tourmaline bearing hydrothermal veins in the Kamituga and Lugushwa areas, and Moloto (2017) from S isotopic analyses conducted on vein pyrite and host rock pyrite of Twangiza area. The association of gold with magmatic fluids from the Kasika leucogranite, proposed by Walemba (2001) and the metasedimentary source gold proposed by Buttner et al. (2016) and Moloto (2017) are debatable, because fluids that may have carried gold may have been either primary magmatic fluids or metamorphic fluids mobilized in the host rock by contact metamorphic heat or during subsequent regional metamorphism and deformation.

I.1. Aim and objectives of this study

The aim of this study is to investigate the sulphide textures and compositions of mineralized and unmineralized samples of different rock types from Twangiza Mine for the understanding of the spatial association of gold with sulphides. The understanding of the spatial association of gold with sulphides will further enable as far as possible to understand the deposit and the nature and origin of the gold mineralization.

The objectives of this study are to:

(i) characterize different textures and compositions of sulphide phases from different lithological sources, such as black shales, albitite intrusions and hydrothermal veins; and

(ii) compare and contrast possible textural and compositional differences between mineralized and unmineralized samples.

The evaluation of possible mineralization events and primary sources of gold in the Twangiza deposit is not the primary target of the current study, but will be attempted as far as possible on the basis of the obtained data.

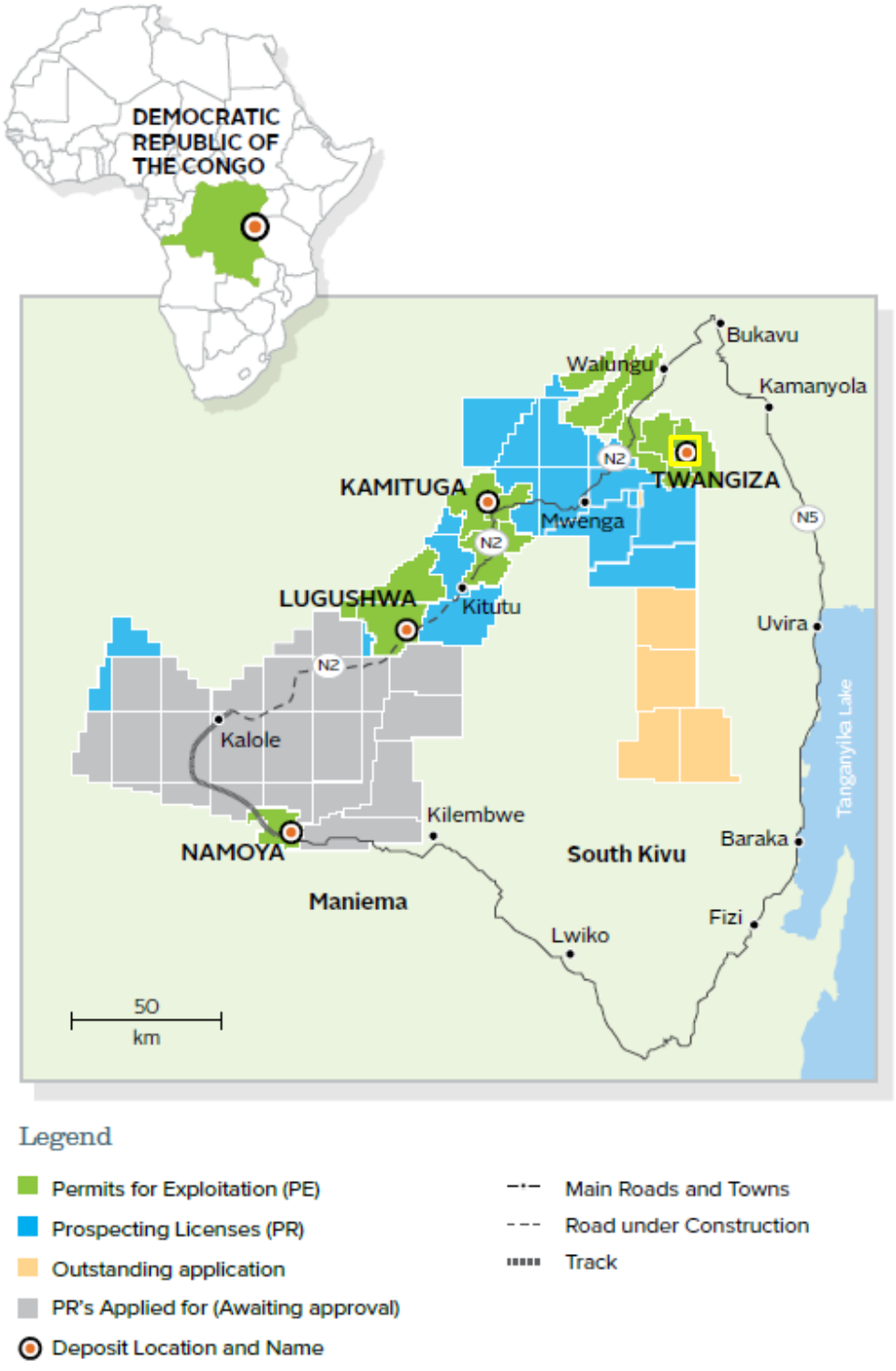

Figure 1. Location of the Twangiza Mine (Banro Corporation, 2017)

I.2. Research approach and structure of this study

The sample basis for this study includes 24 polished sections from 20 sulphide-rich drill core samples, with some samples subdivided into A and B samples, from different mineralized and unmineralized zones (Table 1). A careful microscopic investigation of the petrography and microstructures was followed by micro-chemical analysis using EDS (Energy Dispersive Spectroscopy) of sulphides and rock-forming silicates.

Eight samples were collected of mineralized and unmineralized black shale, six samples of mineralized and unmineralized granitoids, and six samples of mineralized hydrothermal veins. Depending on the complexity of the samples, several thin sections may have been cut per sample. Based on the petrographic analysis, fourteen thin sections were selected for EDS analysis.

The investigation of sulphide textures of samples from the Twangiza deposit has been conducted on the Olympus BX60 microscope from the Rhodes University's Microscopy Laboratory. The microscope was equipped with a PAXcam digital camera, which permitted the capturing of the mineral photomicrographs identified in the samples. The EDS analysis was performed on an Oxford Instruments INCA Energy350 microanalysis system Si-Li detector attached to a TESCAN Vega TS 5136LM SEM (Scanning Electron Microscope) of Rhodes University Electron Microscope Laboratory. Analyses were conducted at 20 kV and were calibrated to a cobalt standard sample's peak. The calculation of resulting mineral compositions was processed by Rock Maker software tool (Büttner, 2012).

This study is subdivided into five major sections. The first section is a short introduction, which presents Twangiza Mine, the aims, the approach, and the expected results of this study. The second section provides the geological background in which Twangiza Mine is located. The third section comprises the results of sulphide textural analysis and compositions associated with the Twangiza Mine. The fourth section discusses all the results obtained in the third section with the geological characteristics of the mine. Finally, the fifth section provides conclusions.

Table 1. Samples taken from the Twangiza Mine for thin section preparation and EDS analysis

Sample ID	Hole ID	Depth (m)	Au grade (g/t)	Sample type	Description
MBS1	TDD 057	112	0.55	Mineralized black shale	Pyrite rich lenses randomly distributed in black shale since pyrite and arsenopyrite are the only sulphide in the sample.
HVN2	TDD 057	115.5	2.96	Hydrothermal vein	Quartz-carbonate vein crosscutting bedding in black shale with disseminated pyrite along the vein contact selvedge.
MBS3A	TDD 057	121	2.13	Mineralized black shale	Laminated black shale with randomly distributed pyrite, arsenopyrite, chalcopyrite and gold in pyrite rich lenses.
MBS3B	TDD 057	121	2.13	Mineralized black shale	Randomly distributed pyrite and chalcopyrite with gold and rutile in laminated black shale crosscut by a quartz-carbonate veinlet with occasional pyrite and arsenopyrite.
UMBS4A	TDD 049	83.5	0.08	Unmineralized black shale	Pyrite rich lens crosscut by a quatz vein in black shale.
UMBS4B	TDD 049	83.5	0.08	Unmineralized black shale	Pyrite randomly distributed in black shale matrix.
HVN5	TDD 049	86.5	1.02	Hydrothermal vein	Quartz vein crosscutting bedding in black shale with abundant disseminated pyrite along and around the vein.
MBS6	TDD 040	170.5	1.69	Mineralized black shale	Randomly distributed pyrite in black shale crosscut by a quartz-plagioclase vein.
HVN7	TDD 040	171.5	4.27	Hydrothermal vein	Quartz-carbonate vein banded with host rocks fragments and pyrite-rich layers in the same trend as host rock bedding.
HVN8	TDD 036	106.5	4.97	Hydrothermal vein	Massive pyrite and arsenopyrite with gold in quartz-carbonates vein crosscutting the bedding in black shale.

UMBS9	TDD 036	316	0.005	Unmineralized black shale	Pyrrhotite and rare arsenopyrite randomly distributed in back shale.
UGR10	TDD 036	261.8	0.06	Unmineralized granitoid	A porphyritic feldspar granitoid with rutile and pyrite occasionally distributed in the matrix.
UMBS11	TDD 035	135.5	0.01	Unmineralized black shale	Pyrite-rich spherical bodies in the form of nodules randomly distributed in the black shale.
UMBS12A	TDD 078	188	0.16	Unmineralized black shale	Rare pyrite and pyrite rich lenses randomly distributed in black shale.
UMBS12B	TDD 078	188	0.16	Unmineralized black shale	Pyrite irregularly distributed in black shale crosscut by pyrite rich stringer and quartz- carbonate veinlets.
UGR13	TDD 078	264.1	0.04	Unmineralized granitoid	Pyrrhotite occasionally distributed in porphyritic feldspar granitoid.
UGR14	TDD 078	232.48	0.03	Unmineralized granitoid	Rare pyrite randomly distributed in feldspar porphyry granitoid.
MBS15	TDD 052	275.7	1.62	Mineralized black shale	Pyrite randomly distributed in black shale black shale crosscut by quartz-carbonate veinlets.
HVN16	TDD 054	103.2	2.98	Hydrothermal vein	Massive pyrite in quartz-carbonate vein in black shale with abundant disseminated pyrite along the vein selvedge.
MGR17	TDD 058	159.8	1.05	Mineralized granitoid	Randomly disseminated pyrite, arsenopyrite and chalcopyrite in feldspar porphyry granitoid crosscut by carbonate vein.
MGR18	TDD 079	111.8	2.56	Mineralized granitoid	Randomly disseminated pyrite in porphyritic feldspar granitoid.
HVN19	TDD 079	132.8	6.36	Hydrothermal vein	Massive pyrite and arsenopyrite in quartz-carbonate vein in porphyritic feldspar granitoid.
MGR20	TDD 229	416	2.24	Mineralized granitoid	Disseminated pyrite and chalcopyrite in porphyritic feldspar granitoid.

I.3. Previous work

Few studies have been conducted in the Twangiza area. Some of the most recent and relevant work in the area has been conducted by Walemba (2001) and Walemba and Master (2005). Walemba (2001) defined the tectono-metallogenic evolution of Neoproterozoic gold deposits in the Kadubu area where he suggested a tectonic evolution from compression phases to extension, and described different gold and tin deposits within the Kadubu area. He proposed a genetic model for the Twangiza deposit which suggests two phases of mineralization: an earlier phase consisting of sulphides veining within classic saddle reef structures; and a later, essentially fault-controlled, of quartz reef. He suggested that the hydrothermal mineralizing fluids were mobilized from the Neoproterozoic Kasika Leucogranite during the Pan-African cycle and deposited gold within the actual deposit.

However, Walemba and Master (2005) focused on the diamictites that overlie the mineralized formations of Twangiza Mine. They interpreted the diamictictes and lonestone-bearing iron-rich sedimentary rocks as glaciogenic strata correlated with other Neoproterozoic glacial sequences in the region and in the world.

Chuwa (2011) described different lithological, structural, mineralization, and alteration features of the TNGB (Twangiza-Namoya Gold Belt), which extends from Twangiza to Namoya, and suggested that deposits within the area include the reduced intrusive-related gold deposit and orogenic gold deposit types. He also pointed out that there is a strong structural control of the mineralization, and intense hydrothermal alteration is associated with zones of intense fracturing. He mentioned that mineralizing fluids responsible of gold mineralization in the area originated probably from the devolatisation of deeply buried greenstones of Archean to early Proterozoic formations channelled by major pathways to upper levels of the crust.

Büttner et al. (2016) proposed a sedimentary source for tourmaline-bearing hydrothermal veins within the TNGB by comparing hydrothermal tourmaline major elemental and the boron isotopic composition from Kamituga and Lugushwa areas with pegmatitic tourmaline from Kamituga.

Rautenbach et al. (2011) proposed a paragenetic model of Twangiza Mine suggesting that the intrusion of albitites occurred at ca. 750 Ma into the Kibaran belt, postdating G4 granites that were emplaced around 975 Ma and after which sedimentation continued throughout the Neoproterozoic

including glacial diamictites at ca. 800 Ma. During the Pan-African orogeny the sedimentary rocks and albitites were folded into N-S trending folds. Paleoproterozoic and Mesoproterozoic rocks and structures were overprinted. Thus, gold-bearing fluid from devolatisation of the lower crust entered structural traps due to the high heat flow and regional compression.

In earlier work, different authors described the area, but most of their research was on a regional scale basis, without much detailed information. Cahen (1954) defined two geological groups in the region based on the direction of structural features and lithostratigraphic sequences. He ascribed NW-SE structures to the Ruzizian Belt, which is related to the Paleoproterozoic Ubendian Belt, and NE-SW oriented structures to the Urundian Belt, related to the Mesoproterozoic Kibaran orogeny. He suggested that the Neoproterozoic Itombwe Synclinorium Supergroup lie unconformably on the Ruzizian Belt, which divides the Urundian Belt into two segments in the region.

Villeneuve (1987) suggested the presence of a Pan-African folded belt within the Great African Lakes Area, forming N-S linear structures of the Itombwe Synclinorium, similar to other tectonic Pan-African troughs from north-eastern DRC and western Uganda.

The characterization of sulphide textures to decipher the deposit history and evolution processes has been widely conducted on different deposits. It is, for instance, the characterization of sulphide textures conducted by MacLean (1991) on several deposits from Canada, South Africa, Ireland and Japan in order to infer processes responsible for the formation of the deposits.

Hammond et Tabata (1997) considered sulphide compositions of the Paleoproterozoic Birimian Greenstone Belt in Ghana in order to identify mineralized phases in different paragenetic stages. Altigani et al. (2016) studied sulphide textures of the Barberton Greenstone Belt in South Africa to identify different phases of hydrothermal events and the associated gold mineralization phases.

Tibane (2013) considered pyrite textures and compositions of the Ventersdorp Contact Reef (VCR) in order to investigate different mechanisms, depositional models and the nature of the ore-hydrothermal fluid, which occurred in reef formation. Takeshi (1999) differentiated pyrites from the Princeton gold mine in the Barberton Greenstone Belt based on texture into sedimentary and hydrothermal origin species and described the hydrothermal-related type as the mineralized phase.

The characterization of sulphide textures and related chemical composition in order to investigate the possible source of gold and / or the mineralization phase events of the Twangiza area has not yet been the subject of any particular study.

II. GEOLOGICAL BACKGROUND

II.1. REGIONAL GEOLOGICAL CONTEXT

II.1.1. Geological Setting of the Region

Twangiza Mine is located within the Western Branch of the East African Rift System. The East African Rift System (EARS) started to form at around 45 Ma and the rifting process is still on-going (Walemba, 2001; Harðarson, 2014). The EARS is formed of two branches: the Eastern Branch and the Western Branch. The Eastern Branch extends 2200 Km from the Afar-Ethiopian Rift via the Kenyan Rift to northern Tanzania. The Western Branch extends 2100 km from Lake Albert to Lake Malawi (Harðarson, 2014).

The Western Branch of the East African Rift System (WBEARS) has a sigmoidal shape and is segmented along its length into individual and asymmetric basins that are often filled with lakes. From north to south these are Lake Albert, Edward, Kivu, Tanganyika, Rukwa and Malawi. High angle faults surround the WBEARS with depth to detachment estimated at 20-30 km. They extend along the rift in the form of a series of en-echelon border fault segments interconnected by oblique-slip transfer faults, ramps and monoclines (Ebinger, 1989; Walemba, 2001).

The WBEARS is subdivided into three segments. First, the northern segment which is formed of a NW-SE striking basement ridge and border fault segments that are 60 to 120 km in length. The central segment is formed by NW-SE en-echelon marginal faults extending from 300 to 500 km in length, and covering a 150 km wide and 900 km long deformation zone. The study area is located within this segment. The southern segment comprises small basins further to the south (Walemba 2001).

Orogenic chains crop out in the WBEARS. The Kibaran Belt (ca. 1400-900 Ma), which is divided into two segments: the Kibara Belt in the SW and Karagwe Ankole Belt in the NE. NW-SE striking

Paleoproterozoic terranes in structural continuity with the Ubende Belt are referred to as the Ruzizian Belt. The Neoproterozoic Itombwe Synclinorium Supergroup (ca. 976-575 Ma) is overlain by recent formations (Tack et al., 2010).

Alkaline plutonic complexes of similar ages, rock types, and which are anorogenic in nature intrude the region. These alkaline complexes were emplaced in structurally weak zones and form two arrays along the WBEARS, comprising a Mesoproterozoic group (ca. 1250 Ma) and a Neoproterozoic group (ca. 750 Ma) (Tack et al., 1994; Walemba, 2001). Volcanic rocks in the eastern DRC occur principally in the Virunga, Bukavu and Mwenga-Kamituga areas (Figure 2). Volcanic rocks in the Bukavu area consist generally of rift-related tholeiitic rocks (ca. 18-6 Ma), Na alkaline lavas (ca. 8-1.6 Ma), and transitional lavas (10 000 years) (Walemba, 2001).

II.1.2. Kibaran belt

The Kibaran Belt is a Mesoproterozoic belt (ca. 1400-900 Ma) extending from Katanga (DRC) through the eastern part of DRC (Kivu and Maniema), Burundi, Rwanda, and Tanzania up to Uganda (Tack et al., 2010). It belongs to a roughly parallel series of Mesoproterozoic belts of eastern (Irumide, Malawi-Mozambique) or southern Africa (Lurio, Natal, and Namaqua belts) (Walemba, 2001).

The Kibaran orogen evolved between two Archean-Paleoproterozoic cratons: the Congo Craton to the west and the north, and the Tanzania Craton and Bangweulu Block to the east and the south (Figure 3). The Kibaran belt shows generally north-eastern structural trends, which in the Kivu area are separated into two segments by the Ruzizian belt considered as the extension of the Paleoproterozoic Ubende belt across Lake Tanganyika. The Kibaran belt is considered to have originated from different processes such as a collisional orogeny, or an intra-cratonic orogeny with different periods of extension and compression, and / or an intra-cratonic extensional detachment structure favoured by strike-slip reactivation of the NW-trending shear zone of the Paleoproterozoic basement (Dewaele et al., 2010).

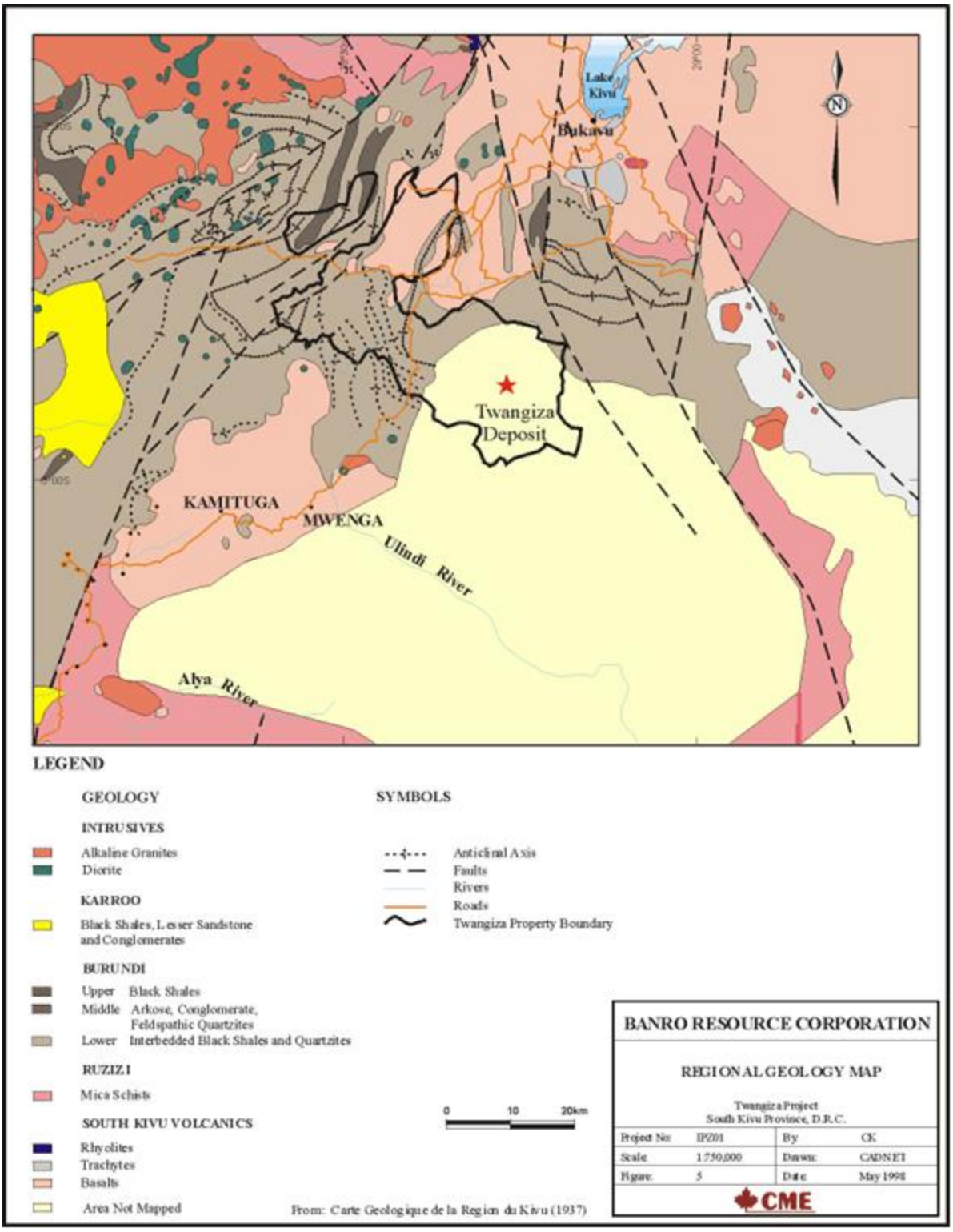

Figure 2. Regional geological map of the Twangiza area (BEEC, 2017).

The rocks of the Kibaran belt are broadly subdivided into three lithostratigraphic divisions: the Lower Group formed of a basal conglomerate and dark laminated pelite with siltstone, sandstone, and quartzite intercalations; the Middle Group is formed of reddish to purple arenaceous rocks with minor dacitic and basaltic volcanic rocks; and the Upper Group is preserved in major synclinoria structures containing a basal polymictic coarse conglomerate followed by ferruginous quartzite, siltstone, shale and immature clastic sediments (Pohl, 1994; Walemba, 2001).

The Kibaran orogen in central East Africa consists of Paleo- and Mesoproterozoic rocks intruded by four generations of granites (Dewaele et al., 2010). G1 and G2 are considered as syn-orogenic, whereas G3 and G4 are post-orogenic (Walemba and Masters, 2005);

- G1: ca. 1370±25 Ma granitoids, consisting of porphyritic gneissose two-mica or biotite adamellite (quartz monzonite);
- G2: dated at ca. 1310±25 Ma, consisting of a non-porphyritic peraluminous adamelitic orthogneiss;
- G3: dated at ca. 1094±50 Ma, this granitoid emplacement episode is composed of alkaline biotite granite;
- G4: 976±10 Ma, consisting of tin granite associated with abundant pegmatite and veins hosting Sn, Au, W, Nb, Ta, Be, Cu, Pb, P, U and tourmaline. G4 granites are related to the main contractional episode that resulted in the development of upright folds in metasediments and the regional S2 cleavage. They commonly occur in anticlinal structures (Walemba, 2001).

Four deformation phases are identified in the Kibaran belt: (i) D1 forming the S1 schistosity parallel to the bedding with minor isoclinal folds and thrusts, (ii) D2 corresponding to NW-SE trending folds and NW-SE shearing subparallel to the folding, (iii) D3 consisting of N-S oriented fold axes resulting from the reactivation of D2, and (iv) D4 corresponding to shear folding of alkaline and carbonatitic intrusions (Pohl, 1994; Walemba, 2001).

In the eastern part of the Kibara belt mafic-ultramafic layered complexes, for instance the Kabanga-Musongati and Kapalagulu intrusions, host Ni-Co-Cu-Ti-V-PGE deposits formed at around 1403±14 Ma, as estimated from U-Pb dating on zircon (Tack et al., 1994; Deblond, 2013; Pohl et al., 2013). They are interpreted to mark a pre-orogenic extensional phase with mantle

magma influx during the Kibaran basin formation (Pohl et al., 2013). These mantle magmas pre-date the G1-G4 granite emplacement episodes.

The rocks of the Kibaran belt in the eastern DRC underwent a widespread low-grade greenschist facies metamorphism, though medium- to locally- high-grade metamorphism is observed around granitic intrusions (Walemba, 2001). Two phases of metamorphism are recognized in the belt: an earlier phase related to the syn- to late-tectonic G1 and G2 granite batholiths with an intermediate pressure of 4 to 5 kbar and temperature of 500 to 600 °C, attested by staurolite-kyanite-sillimanite in metapelites and incipient melting in migmatites; and a later low-grade metamorphic phase associated with the 1 Ga granites at low pressure. The shallow emplacement depth of associated granites is marked by a contact aureole of andalusite in metapelite country rock and the occurrence of spodumene in associated rare-metal pegmatites (Pohl et al., 2013).

Büttner et al. (2016) conferred the source of the hydrothermal fluids system in the Kamituga and Lugushwa area in the eastern part of DRC, to metasedimentary host rocks, probably as a result of the heat influx produced during the early Pan-African event. Tourmaline-rich hydrothermal alteration at Lugushwa was dated as Pan-African with an age of 677±17 Ma, while a Kamituga pegmatite was dated at 981±16 Ma and ascribed to the G4 granites pulse (Rb-Sr mineral isochron analysis).

II.1.3. Itombwe Synclinorium Supergroup

The Itombwe Synclinorium Supergroup unconformably overlies the Kibaran belt. It is a Neoproterozoic entity that corresponds in depositional age to the Pan-African orogenic cycle (ca. 976-575 Ma; Walemba, 2001) (Figure 3). The Itombwe Synclinorium Supergroup is a narrow lithostratigraphic unit trending NNE over 160 km (Deblond, 2013), and is formed by a series of basins or troughs interpreted as intra-mountainous molasse or rift basins (Walemba, 2001; Walemba and Master, 2005). The current study area at Twangiza Mine is located within this belt.

The Itombwe Synclinorium Supergroup in the eastern DRC shows a lithostratigraphic subdivision into two groups: the Lower Kadubu Group and the Upper Kadubu Group (Walemba, 2001; Figure 4). The Itombwe Synclinorium Supergroup formations are composed of terrigenous sediments

comprising shales, quartzites and conglomerates with minor diamictites and marbles (Deblond, 2013). Four units are defined within the stratigraphic sequence (Walemba and Master, 2005) consisting of:

- Conglomerates with intercalation of phyllites and quartz phyllites, locally with tremolite- and wernerite-bearing marbles;
- Schists, in place phyllitic with arkose interlayers;
- Sandstones and thick quartzite layers;
- Schists with conglomerate layers and tillite.

The Itombwe Synclinorium Supergroup units are folded into a large synclinorium and show a low-grade metamorphic overprint. The Itombwe Supergroup has been assigned to the alignment of Neoproterozoic grabens that occur along the main tectonic structures of the Paleo- and Mesoproterozoic basement in Central Africa that were reactivated during the Pan-African and Palaeozoic events (Deblond, 2013).

The setting in which the Itombwe Synclinorium Supergroup sediments were deposited is an intracontinental extensional rift, hosting clastic detritus from the adjacent elevated Kibaran basement (Walemba, 2001). The broad synclinorium structure formed during the Pan-African cycle from contraction and metamorphism of the clastic detritus (Walemba, 2001).

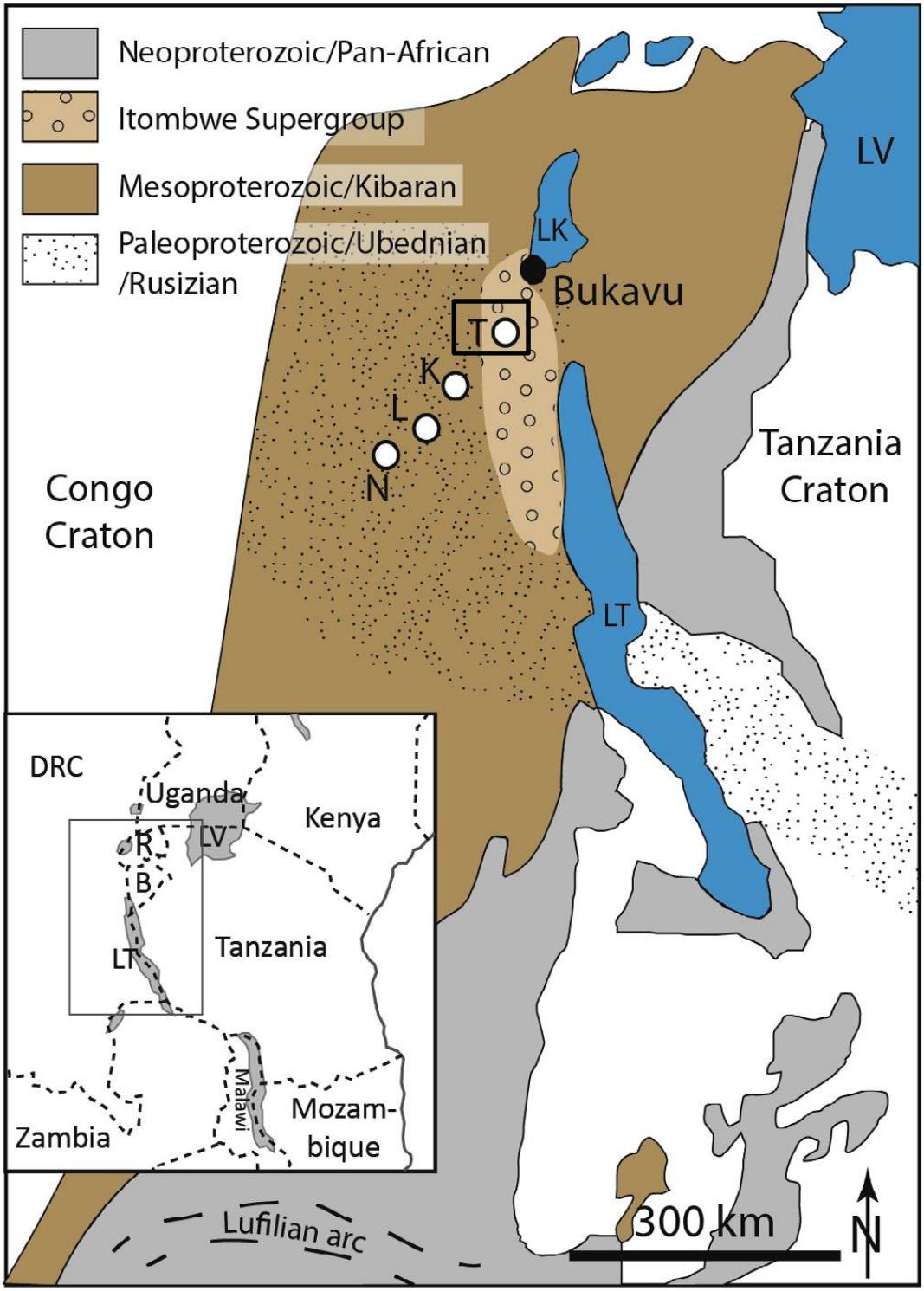

Figure 3. Regional geology map and location of Twangiza deposit in the TNGB belt (T: Twangiza, K: Kamituga, L: Lugushwa, N: Namoya, R: Rwanda, B: Burundi, DRC: Democratic Republic of the Congo, LT: Lake Tanganyika, LK: Lake Kivu, and LV: Lake Victoria) (modified from Büttner et al., 2016)

II.2. GEOLOGICAL FRAMEWORK OF KADUBU AREA

II.2.1. Geological Setting of the Kadubu Area

Twangiza Mine is located within the Kadubu area, which is covered by rocks that are part of the Itombwe Synclinorium Supergroup. The Kadubu area covers a large region extending over approximately 750 km^2 between 28°33' - 28°50' E and 2°45'-2°57' S (Figure 4) (Walemba, 2001).

The Kadubu area is constituted of a sequence of metasedimentary rocks intruded by metasomatised magmatic rocks (Figure 4) (Walemba, 2001). Walemba (2001) investigated the age of these intrusions in the Twangiza area using Sm- Nd and Rb - Sr isotope dating of feldspar that yielded an age of 1078±27 Ma. This relates these intrusions in time to the G3 granite emplacement episode. The $^{87}Sr/^{86}Sr$ and Sm/Nd isotopic data of these intrusive rocks suggested a crustal source. He referred these metasomatic intrusion rocks to albitite. However, this age is in disagreement with the age of the hosting Itombwe Supergroup sedimentary rocks, which are presumed to have a depositional age well within the Neoproterozoic (976-575 Ma; Walemba, 2001). Accordingly, either the depositional or the magmatic age may be incorrect and both need to be revised.

The rocks that cover the Kadubu area are bound by major thrust-faults. Bounding faults, major internal normal shear-faults, strike-slip faults, and reverse faults have listric geometry and are interpreted to flatten at depth (Walemba, 2001). They are related to an inferred detachment fault, which is interpreted to occur at the boundary of the Itombwe Synclinorium Supergroup and the Kibaran basement.

The rocks in the Kadubu area are subdivided into two geochemically and structurally distinct groups, the Lower Kadubu Group and Upper Kadubu Group, separated by the Tshondo fault/shear zone that forms a distinct tectonic, metamorphic and geochemical discontinuity (Walemba, 2001). However, Villeneuve (1987) suggested that the Tshondo fault constitutes the boundary between the Kibaran belt and the Pan-African belt.

The age of the mineralization within the Kadubu area has been estimated at 522±15 Ma from $^{40}Ar/^{39}Ar$ isotopes of hydrothermal muscovite (Walemba, 2001). This however seems not to be clearly related to the gold mineralisation, which, in addition, may have occurred in several episodes.

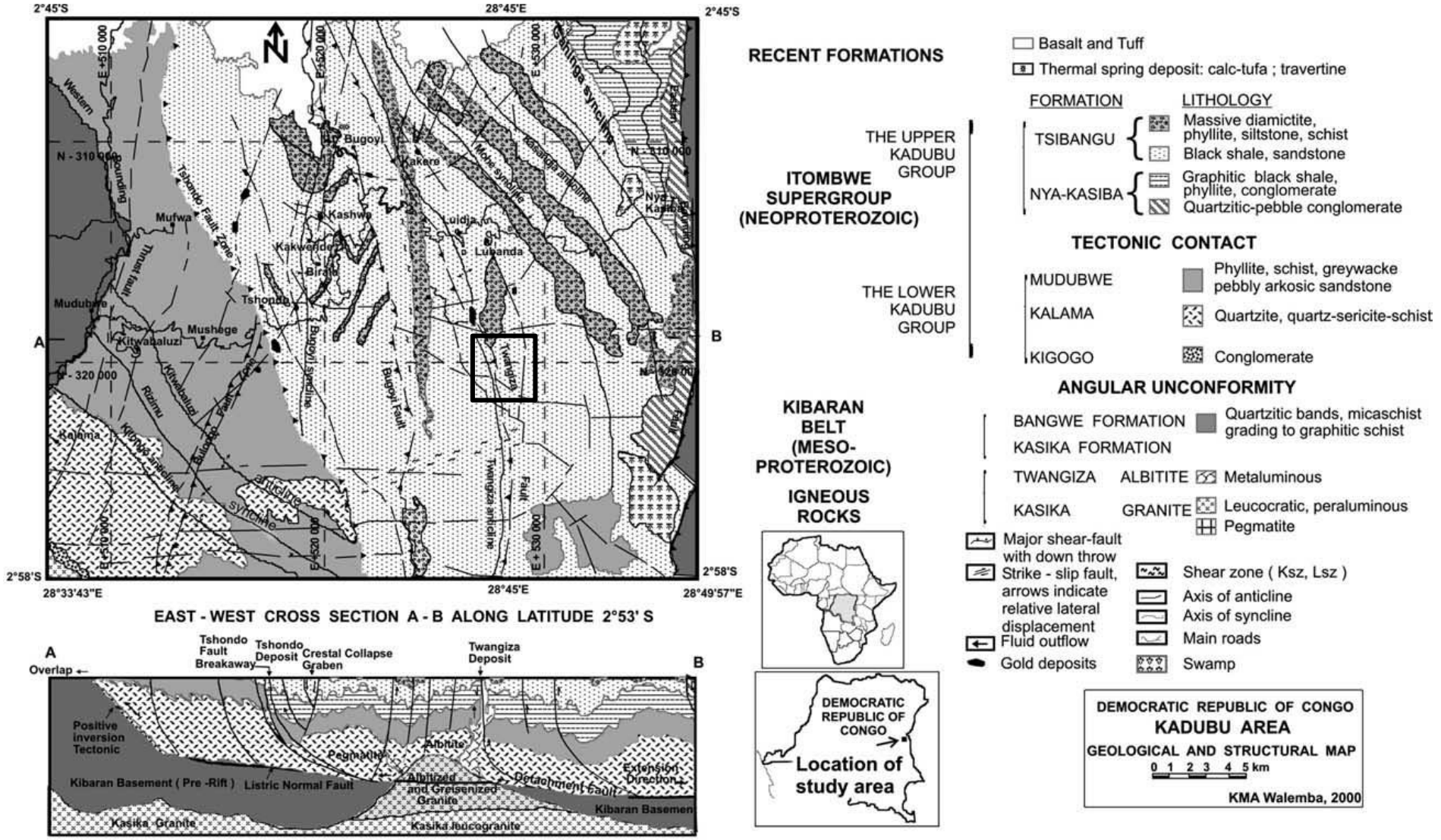

Figure 4. Geological map of the Kadubu Area (modified from Walemba and Master, 2005)

II.2.2. Lithostratigraphy of the Kadubu Area

The basement in the Kadubu area consists of Kibaran Belt rocks of Mesoproterozoic age with an estimated depositional age of 1.38 – 1.0 Ga. They are related to the Bangwe Formation in the east and the Kasika Formation in the west (Table 2; Figure 4; Walemba and Master, 2005).

The Bangwe Formation has an average thickness of >600 m and occurs along the Luzinzi River. It consists of quartz sericite schists containing two coarse-grained saccharoidal-textured white quartz layers displaying local planar crossbedding (Walemba and Master, 2005).

The Kasika Formation (Table 2) occurs in the western extremity of the Kadubu Area and consists of dark micaschist grading into black graphitic schists that are interbedded with ripple-marked white quartzitic layers. It is intruded by the Kasika Granite which is an S-type two-mica G4 tin granite (1020±50 Ma) with associated pegmatite swarms. This indicates that the depositional age of the hosting metasediments is Mesoproterozoic (>1000 Ma) or older. Along the contact aureole of the granite, metasedimentary rocks are metamorphosed into gneisses and biotite schists with garnet, kyanite and staurolite, and garnet- and tourmaline-bearing quartzites (Walemba and Master, 2005).

Table 2. Stratigraphy of the Kadubu Area (modified from Walemba, 2001)

Group	**Formation**	**Member**	**Thickness (m)**	**Lithology**
Upper Kadubu	Tsibangu	Diamictite	>800	Diamictite with schistose pelitic matrix
		Arkosic sandstone	3	Arkose, conglomerate
		Phyllite	600	Sericite schist
		Pyritic Black Shale	>600	Black shale (**Twangiza Mine**)
	Nya-Kasiba	Yellow Phyllite	500-750	Sericite schist, feldspathic Quartzites
		Graphitic Black Shale	50-100	Graphitic black shale
		Mukuka	100-200	Jaspilitic laminites Turbidites, conglomerates
		Quartzitic-pebble	0-500	Conglomerate, quartzite
Tectonic Contact				
Lower Kadubu	Mudubwe	Phyllite	>600	Phyllite, schists, quartzites
		Greywacke	>400	Greywackes
	Kalama		>2500	Sericite schist, quartzites
	Kigogo		2-7	Dolomite
			>250	Conglomerate, quartzites
Unconformity				
Basement: Kibaran	Kasika			Graphitic micashists and quartzites intruded by 1020 ± 50 Ma Kasika Granite
	Bangwe		>600m	Quartz sericite schists

The Lower Kadubu Group (Table 2) unconformably overlies the graphitic mica schists and quartzites of the Kibaran Kasika Formation and consists of three formations: the Kigogo Formation, Kalama Formation, and Mudubwe Formation. They form an overall thickness of ~3700 m. The Kigogo Formation has an overall thickness of >2000 m and consists, from the base to the top, of conglomerate overlain by a chloritic quartzite with quartz and cherts clasts in a chloritic matrix, followed by cream-colored dolomite on top of the formation. The Kalama Formation has an approximate thickness of about >2500 m and consists of dark sericite schist interbedded by quartzite. Finally, the Mudubwe Formation is >100 m thick and consists of a sequence of rhythmical alternating metagreywacke, quartzitic sandstone, schists, and phyllite from the base to the top (Walemba and Master, 2005; Villeneuve, 1987).

The Upper Kadubu Group (Table 2) is composed of the Nyakasiba and Tshibangu formations (Deblond, 2013). The Nyakasiba Formation has an overall thickness of 1000 m and comprises four members:

- Quartzitic-pebble conglomerate member,
- Mukuka Member consisting of laminated and normally graded turbidites with scoured bottom and ripple tops. It contains lenticular oligomictic conglomerates with rare subrounded to angular striated quartzitic pebbles and isolated lonestones overlain by iron-rich hematitic, and jaspilitic laminated sediments containing isolated quartzitic and exotic igneous lonestones,
- Graphitic Black Shale Member consisting of fine laminated phyllitic sericitic argillite rhythmically interbedded with oligomictic lenticular conglomerate,
- Yellow Phyllite Member comprising plane-laminated phyllitic sericite schist with intercalation of fine to medium-grained plane bedded and normally graded feldspathic quartzite (Walemba and Master, 2005).

The Twangiza deposit is hosted within the Tshibangu Formation, which also consists of four members:

- Pyritic black shale member consisting of moderate to strong graphitic, well bedded to thinly laminated fine-grained pyritic black shale and including quartz-sericite-schist with some indurated and / or silicified horizons with siltstone and sandstone beds.

- Phyllite member consisting of homogeneous greyish-brown silty phyllites rhythmically interbedded with quartzitic sandstone.
- Arkosic sandstone member composed of medium to coarse-grained arkose interbedded with black shale.
- Diamictite member formed of a polymictic matrix-supported conglomerate with unsorted pebbles of quartzite, schist, gneiss and granite in a dark schistose chloritic matrix (Walemba and Master, 2005; Villeneuve, 1987).

II.2.3. Structural context and metamorphism of the Kadubu area

The main structure of the Kadubu area is a detachment thrust stack that was formed by contractional tectonics. The thrusted sheets were later overprinted by strike-slip shearing. This structure is related to the Pan-African collisional history between the Congo and Tanzania cratonic plates (Walemba, 2001).

The Lower and Upper Kadubu area formations are folded into upright, north to north-west trending, tight to isoclinal folds. Three deformation phases are recognized in the area. D1 and D2 are contractional episodes, D3 an extensional phase. The D2 deformation phase age has been estimated at 575 ± 83 Ma from $^{40}Ar/^{39}Ar$ isotopic analysis, and corresponds to the Kasika leucogranite emplacement, whereas the D3 deformation phase is ascribed a Phanerozoic age (Walemba, 2001).

The Lower and Upper Kadubu Groups are affected by a lower to middle greenschist facies metamorphism. However, the metamorphic grade increases progressively towards the west through the Upper Kadubu Group from subgreenschist to greenschist facies (Walemba, 2001).

II.2.4. Mineralization in the Kadubu Area

The mineralization of the Kadubu area is generally marked by gold deposits at Twangiza, Tshondo, Mufwa, Kakere and Mwanza, as well as tin deposits at the Kashwa deposit hosted in pegmatites (Figure 4) (Walemba, 2001).

In the Twangiza deposit area, two separated phases of mineralization are considered. An earlier phase comprises sulphide-quartz veining in saddle reef structures related to the D2 folding phase. This mineralization shows the highest gold grades (Walemba, 2001). The second phase of hydrothermal gold mineralization forms quartz reefs during dextral strike-slip faulting related to D3 that overprinted the D2 folding phase (Walemba, 2001).

The gold mineralization phases are associated with different fluids inclusions studied in hydrothermal quartz occurring in quartz veins and in advanced argillic alteration (Walemba 2001). Four types of hydrothermal fluids were recognized; H_2O-NaCl-CO_2-halite, H_2O-NaCl-CO_2, H_2O-NaCl-halite, and H_2O-NaCl. The first phase of gold mineralization is associated with the fluid inclusions containing H_2O-NaCl-CO_2±halite. These fluid inclusions suggest a drop of pressure and veins accompanied by gold and arsenic ore deposition. The second phase of gold mineralization is associated with the fluid inclusions containing H_2O-NaCl±halite. These fluids are characterized by a drop in temperature and an opening in a hydrostatic regime associated with gold, As and Sb ore deposition. The hydrothermal fluids responsible for the gold mineralization are assumed to have originated from fluids from a meteoric source to a mixture of meteoric and magmatic source (Walemba, 2001).

Isotopic analyses of C, O, and S of pyrites and carbonates from the Twangiza and Tshondo quartz veins indicated that the fluids are exotic with regard to the Upper Kadubu Group and are thus considered to have originated form a magmatic source, especially fluids released from the Kasika leucogranite (Walemba, 2001). However, from petrographic, microchemical and S isotopic analyses conducted on the Twangiza deposit metapelites and pyrite, Moloto (2017) suggests that at least some primary Twangiza gold is contained in the host rock sedimentary sequence and may have been extracted into veins. S isotope signatures in vein pyrite are compatible with S isotope signatures from primary host rock pyrite. The Twangiza deposit S isotope values are near neutral and range from $\delta^{34}S$ of -2.2‰ to +3.0‰ with an average of 1.1‰ in pyrites from the host rock

without any relation with the hydrothermal activity. Hydrothermal veins show S isotope values in pyrite ranging from -5.2‰ to +3.0‰, with an average of -1.6‰ (Moloto, 2017).

Albitite porphyry intrusions in the Twangiza deposit are considered to have played a significant role by driving the ore-forming hydrothermal system. A spatial association of albitite and gold mineralization is recognized with higher Au-grades (> 10 g/t) being localized either in the proximity of albitite – black shale host rock contact zone or closely associated with fault – breccia along fault zone (Walemba, 2001). However, also here there is a disagreement between the presumed Pan-African mineralisation that is based on the hydrothermal white mica from the Twangiza deposit age of 522 ± 15 Ma, and the presumed Mesoproterozoic age of the albitites (1078 ± 27 Ma, Walemba, 2001)

Hence, Rautenbach et al. (2011) in the Banro Corporation technical report stated that in the Twangiza deposit, the hinge zones of anticlinal folds constituted the most important trap of the mineralization (Figure 5). Feeder structures might have been sub-vertical, limb-parallel structures and the most intense hydrothermal alteration is in the fold closure in the part of the sequence with abundant sills. This might be due to fluid migration into the low pressure hinge zone, more intense fracturing providing a better plumbing system for fluid flow and increasing fluid/wall rock interaction, and a relatively higher chemical reactivity of the albitite sills. Faulting with an orientation of approximately 55° to 80° post-dated the mineralization event, and displaced mineralizing zones and fold axes. However, if the hinge zone is the preferred site for gold mineralisation, this mineralisation would be younger than the folding. This in turn would rule out a genetic relationship of the mineralisation with the albitite magmatism which preceded folding.

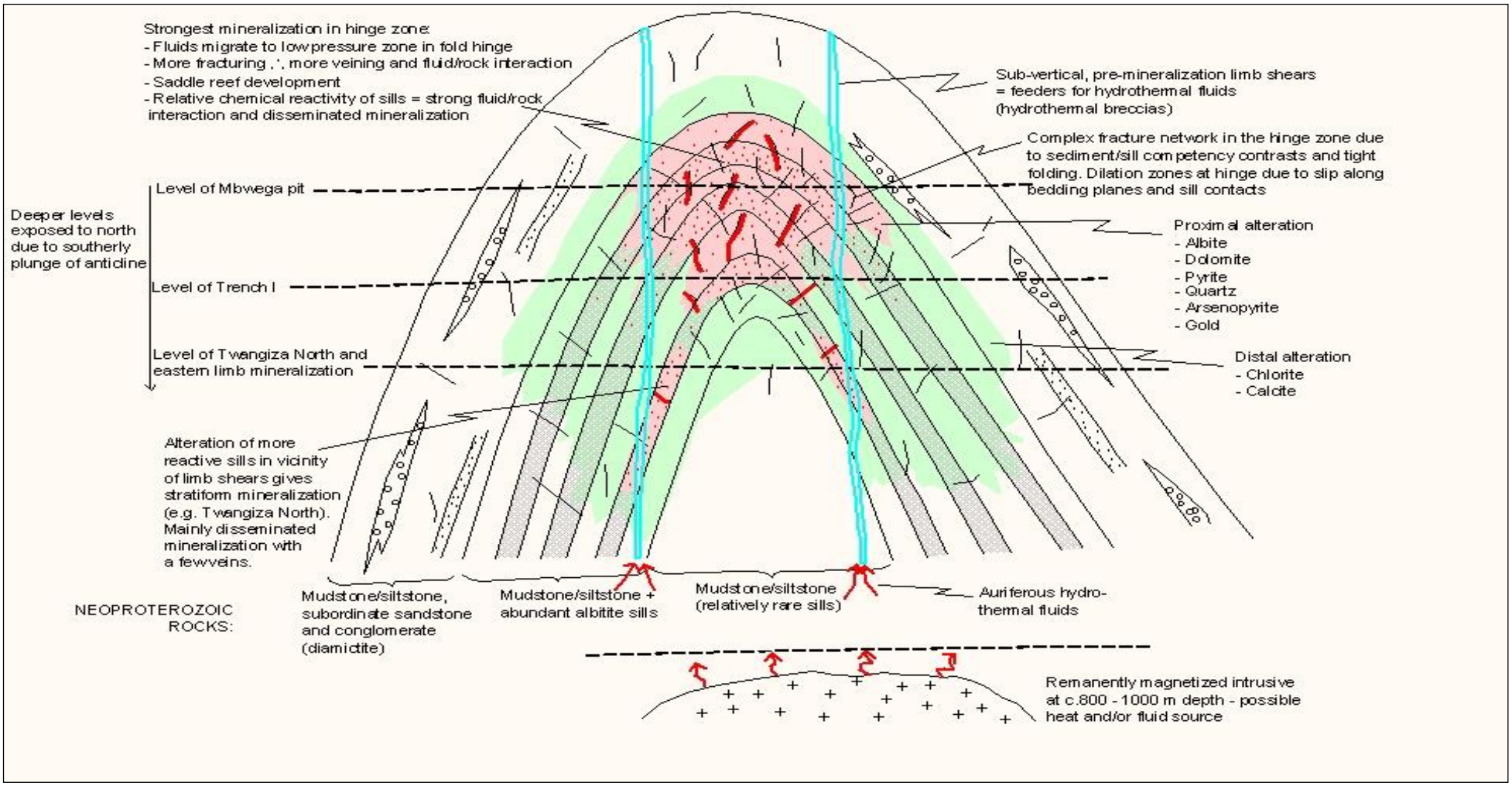

Figure 5. Mineralization model for the Twangiza deposit (after Chuwa, 2011)

II.3. TWANGIZA MINE DEPOSIT

The Twangiza gold deposit is hosted in black shale-type sediments including mudstone and intercalated siltstone. The black shale sediments are intruded by a series of feldspar porphyry granitoid sills folded along the anticline and syncline axis (Figure 6). These black shales belong to the Pyritic Black Shale Member of the Tshibangu Formation in the Upper Kadubu Group.

II.3.1. Lithological aspects of the deposit

Black shales consist of moderately to strongly graphitic, well-bedded and finely laminated rocks with some intercalations of indurated silicified horizons and slightly coarser-grained layers referred to as siltstone (Walemba, 2001 and Rautenbach et al, 2011). Fresh black shale is black in colour, commonly hard and locally siliceous. It contains pyrite and arsenopyrite, which occur as cubes, nodules, irregular spots or infillings along the cleavage. Once weathered, black shales become light greyish in colour and softer, with ferruginous veining associated with limonite-silica-rich veining, and staining on fracture planes. The black shale is fine-grained, carbon-rich, with abundant sericite and quartz. A crenulation cleavage is defined by a micaceous component and graphite that lies in the cleavage planes (Walemba, 2001).

The feldspar-porphyry granitoid, described as albitite by Walemba (2001), forms <1 m to ~50 m thick sills in the Twangiza area (Figure 7) (Rautenbach et al., 2011). Albitites are commonly mineralized in gold around the anticlinal hinge zone, but are barren out of it. These albitites have been metasomatised. Hence, Walemba (2011) defined three types of albitites: dolomitised, chloritised and magnesitised albitites. However, two types of albitites are referred to by mine geologists as “feldspar porphyry” and “mafic feldspar porphyry”. The feldspar porphyry shows a light colour with coarse-grained plagioclase and is commonly crosscut by ferruginous veinlets, whereas the mafic feldspar porphyry shows a dark colour with medium-grained plagioclase. The mafic feldspar porphyry is commonly considered as barren. Weathered albitites appear mottled, soft, flaky, and yellowish-brown to whitish in colour and are crosscut by ferruginous veinlets. Fresh albitites are compact, hard, mottled and appear granular, coarse- to medium-grained, with colour ranging from whitish (dolomitized albitite) to dark green (chloritised and magnesitised

albitite). According to Walemba (2001), albitite is composed of albite as the major component, followed by iron oxide, iron magnesium carbonate, chlorite and sericite. Occasional sulphides are disseminated in the albitite. This assemblage is not magmatic and documents the extensive alteration of the magmatic sills.

II.3.2. Structural aspects of the deposit

The Twangiza deposit structure is characterized by N-S to NNW-SSE trending folds that plunge either to the south or the north. The tightness of the folds vary significantly from open to almost isoclinal, with the mean interlimb angle between 50° to 80° (Rautenbach et al., 2011).

On a small scale, parasitic folds commonly plunge to the north or the south. At the central pit of the Twangiza ore body the plunge of the hosting main anticline changes from south to north. The folding is interpreted as being related to the E-W contractional phase of the Pan-African orogeny around 550 Ma (Chuwa, 2011; Rautenbach et al., 2011). Intrusive sills are concordant with the host sediments rock layering (Figure 7). The predominant orientation of the bedding planes in the two limbs of the anticline has an average strike/dip angle values from right-hand-rule of 145°/56° and 010°/69° whereas quartz-carbonate vein orientations are 081°/72° and 103°/59° as dominant orientations and 171°/70° and 186°/45° as minor orientations (Chuwa, 2011).

Faulting is characterized by NE-SW to E-W strike directions (Chuwa, 2011). Faults are randomly distributed in the area and are commonly not mineralized suggesting that they postdate the mineralization events. However, shear zones and/or breccia zones of approximately 1 m thickness are sub-parallel to the lithological layering, and are commonly enriched in gold (Rautenbach et al., 2011).

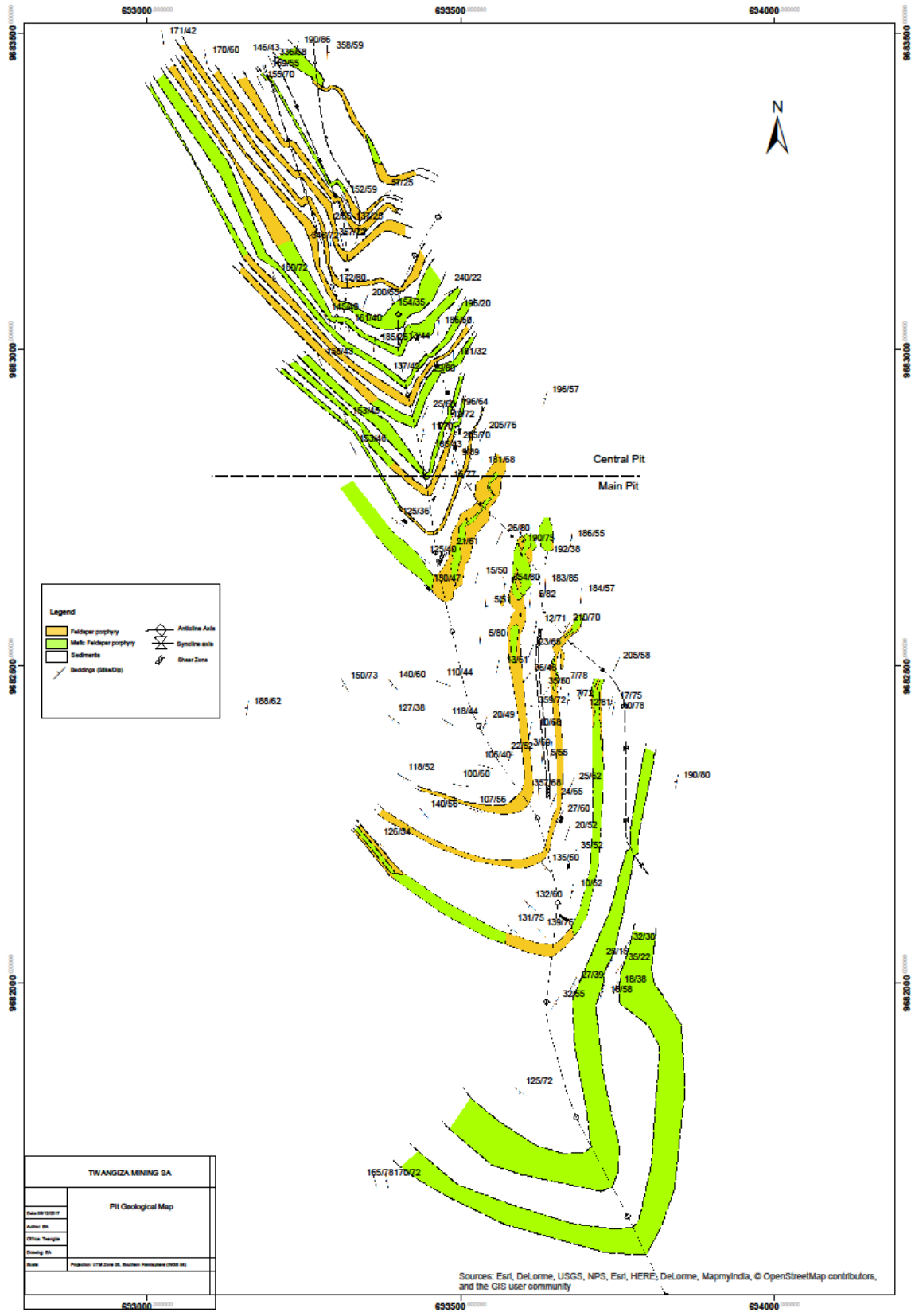

Figure 6. Geological map of the Twangiza Mine deposit

II.3.3. Mineralogy of the deposit

The gold mineralization in the Twangiza deposit is generally associated with disseminated sulphides and an irregular network complex of veins. However, most veins are parallel to the bedding and, accordingly, hydrothermal fluids caused dilation along bedding planes (Rautenbach et al., 2011).

The mineralization style varies between sedimentary hosts and sills. The mineralization within sills correlates with the presence of sulphides that account for approximately 3% of the rock. Locally, the sulphide content may reach up to 30% of a 1 m core sample. Sulphides consist of abundant pyrite and arsenopyrite with proportions of ~65% to ~35%. Sulphides occur in a variety of habits, including disseminated crystals, stringers, coarse-grained crystalline veins up to 10 cm in thickness, and irregular massive patches (Rautenbach et al., 2011).

In the sedimentary host rocks, the proportion of pyrite and arsenopyrite is the same as in sills, but their quantity is relatively low in sedimentary rocks than in sill. Disseminated sulphides are fine-grained and commonly associated with relatively porous siltstone units. Sulphide veins in sedimentary rocks contain more quartz which commonly occurs intergrown with pyrite and arsenopyrite (Rautenbach et al., 2011).

In the oxidized zone, the sulphide-rich veins are weathered to limonite-silica intergrowths with limonite-filled boxworks. Irregular limonite patches and coated vugs have been formed from oxidation of disseminated sulphides (Rautenbach et al., 2011).

The proximal hydrothermal alteration of the ore body in sills is characterized by the formation of albite, dolomite, pyrite, arsenopyrite and gold, whereas in sedimentary rocks it consists of albite, quartz, pyrite, arsenopyrite and gold. However, the distal alteration to the ore body is characterized in the sills by chlorite and calcite (Rautenbach et al., 2011).

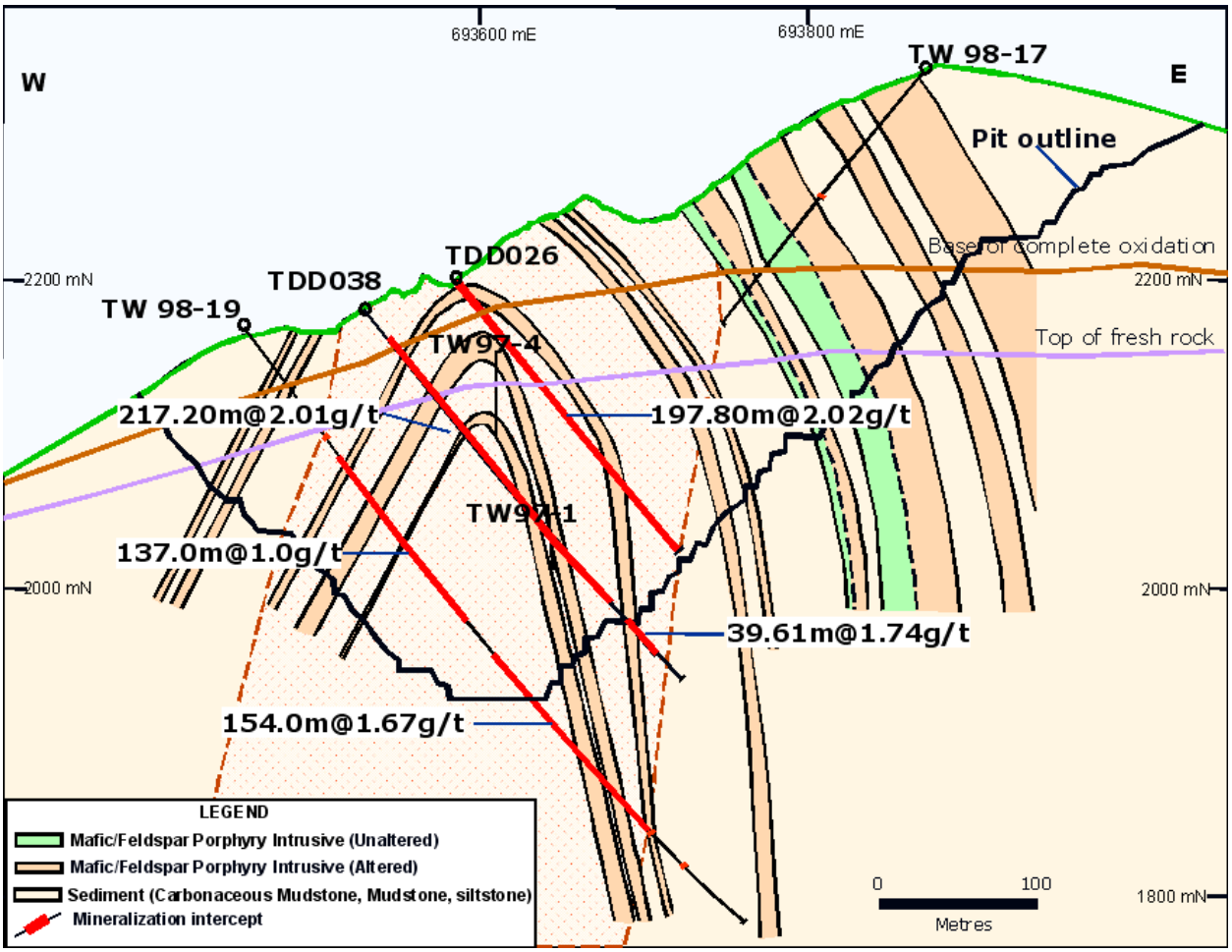

Figure 7. Twangiza Mine E-W pit section (after Chuwa, 2011)

II.4. OVERVIEW OF GOLD-BEARING SULPHIDES

In the metamorphic environment, pyrite (FeS_2) is the most abundant and widespread of sulphides, and most commonly it is found as the main sulphide phase in many ore deposits. Most sulphides lose their original textures during metamorphism, and thus it is difficult to decipher their original features in many metamorphosed deposits. However, pyrite has a high thermal stability (742°C; Craig and Vokes, 1993) and a high physical strength. These properties make it quite stable in the greenschist to amphibolite facies at which most ore bodies are metamorphosed. It is a refractory sulphide and therefore offers many chances of preserving some evidence of pre- and syn-metamorphic development (Craig and Vokes, 1993).

Pyrite has a strong tendency to crystallize in euhedral shape, forming cube-shaped crystals, but a large variety of habits are reported including the pyritohedron form. Pyrite may be affected by brittle deformation resulting in cataclastic texture. However, pyrite tends to recrystallize in response to deformation at greenschist facies and higher grades of metamorphism, resulting in annealed textures and change of grain size (Craig and Vokes, 1993). During metamorphism, the prograde heating of pyrite results in rise of sulphur activity and decomposition of pyrite to form pyrrhotite ($Fe_{(1-x)}S$ (x = 0 to 0.2)). In the same way, pyrite may be formed by retrograde cooling of pyrrhotite resulting in drop of sulphur activity, permitting the re-growth of pyrite as the pyrrhotite releases sulphur (Craig and Vokes, 1993).

Gold from hydrothermal deposits is commonly associated with sulphides, predominantly refractory sulphides such as pyrite (FeS_2) and arsenopyrite (FeAsS). It occurs either in a chemically bonded state and or as nano-size grains of metallic gold. Most refractory gold ore contains gold non-detectable and invisible by conventional optical microscopy or scanning-electron-microscopy techniques (Chen et al., 2002). The enrichment of gold in pyrite often correlates with anomalous arsenic content (Craig and Vokes, 1993) and Fe deficiency in pyrite, and with excess amounts of As along with Fe deficiency in arsenopyrite (Fleet and Mumin, 1997). Most pyrite, including pyrite which intergrows with arsenopyrite, does not contain much arsenic. However, in Au mineralized hydrothermal veins pyrite may contain as much as 8 wt. % arsenic in oscillatory zonal patterns (Craig and Vokes, 1993). Pyrite with high concentrations of As, usually ranging up to 9 wt. %, is referred to as arsenian pyrite (Fleet and Mumin, 1997). Arsenopyrite typically incorporates more invisible gold than pyrite, except when pyrite has more than 0.2 wt. % of arsenic in its structure (Andras and Chovan, 2005).

The incorporation of gold into sulphides depends on parameters such as stoichiometry, temperature, pressure, and the pH of ore-forming fluids in which gold is transported, typically in the form of sulphide or chloride complexes, and/or gold-colloids (Andras and Chovan, 2005). The charge and stability of the aqueous complexes, the surface charge on the sulphide substrate, and the availability of suitable bonding sites in sulphides are important factors to the precipitation of gold (Andras and Chovan, 2005). In arsenopyrite and pyrite, gold particles substitute for arsenic, most likely as a result of similarities in ionic radii of the two elements (Andras and Chovan, 2005).

Since the incorporation of trace elements is controlled by factors such as temperature, the partial pressure of sulphur gas, and pH, the pyrite trace element content may provide information on the physical and chemical environment in which pyrite has formed (Basori et al., 2018).

III. SULPHIDE TEXTURES AND COMPOSITION OF THE TWANGIZA DEPOSIT

III.1. SULPHIDE TEXTURES OF THE TWANGIZA DEPOSIT

III.1.1. Mineralized black shale (MBS) samples

1. **MBS1**

Black shale sample MBS1 was taken at 112 m depth from the TDD057 (Twangiza Diamond Drillhole) core from a 25.78 m thick fine-grained black shale unit (Figure 8.A) interlayered with an upper 10.72 m and a lower 0.47 m thick feldspar-rich granitoid intrusive sill. The sample was taken 2.3 m below the upper granitoid sill. The samples MBS3A and MBS3B (see sections below) come from the same section of this core but were taken some meters apart from each other. Macroscopically sample MBS1 is dark grey with abundant sulphides (Figure 8A and 8B). Sulphides are randomly distrubuted within the laminated dark grey and fine-grained matrix. Within 0.1 to 1.2 cm sized sulphide-rich lenses are formed along the lamination (Figure 8A). Quartz-rich vein and veinlets crosscut the lamination at high angle.

Microscopically, the laminated matrix is essentially formed by quartz, albite, extremely fine dark organic matter, and rare tourmaline (Figure 8D). Quartz occurs as fine-grained anhedral crystals that vary in size from 40 µm to 100 µm. Albite develops a well-defined twinning and occurs together with quartz. Albite grain sizes vary from 22 µm to 120 µm. Albite commonly shows sericitic alteration. The organic matter consists of fine and non-crystalline carbon commonly forming subparallel streaks along the lamination (Figure 8D). Rare muscovite crystals occur commonly aligned along the lamination by 300 µm length and 40 µm thick within the matrix. These crystals are most likely detrital. Euhedral to subhedral pyrite is randomly distributed in the

black shale matrix and is of generally 300 µm in size (Figure 8E). This pyrite commonly appears disintegrated. 10µm to 40µm fine-grained rutile is randomly distributed in the matrix.

Sulphide-rich lenses are elongated parallel to the lamination and vary from 0.1 to 1.2 cm thick (Figure 8A). They are composed essentially of aggregations of sulphide within a mica-rich, quartz-moderate, and albite-rich matrix (Figure 8C). Muscovite, with an overall size estimated at 200 µm x 500 µm, is wrapping around pyrite crystals. Quartz is anhedral in shape and ranges in size from 120 µm to 700 µm. Albite is generally 180 µm, forms anhedral crystals and is randomly distributed within the lens matrix. Albite is also found as inclusions of 150 µm size within sulphide minerals. Rare fine-grained tourmaline, measuring about 44 µm by 110 µm, is randomly distributed within the lens matrix. Abundant subhedral to anhedral pyrite is clustered in the pyrite lens and occurs in different sizes ranging from 80 µm to 2000 µm (Figure 8F). Large crystals of pyrite occur in the central part of the sulphide-rich lenses whereas finer-grained crystals occur towards the rims. Large crystals are abundant and are commonly annealed within the lens.

The vein and veinlets in sample MBS1 (Figure 8A) range in size from approximately 2.5 mm to 70 µm thick and are composed of abundant fine-grained crystals of quartz and minor albite commonly of 40 µm in veinlets. The vein and veinlets cut sulphide lenses at high angle, indicating its younger relative age.

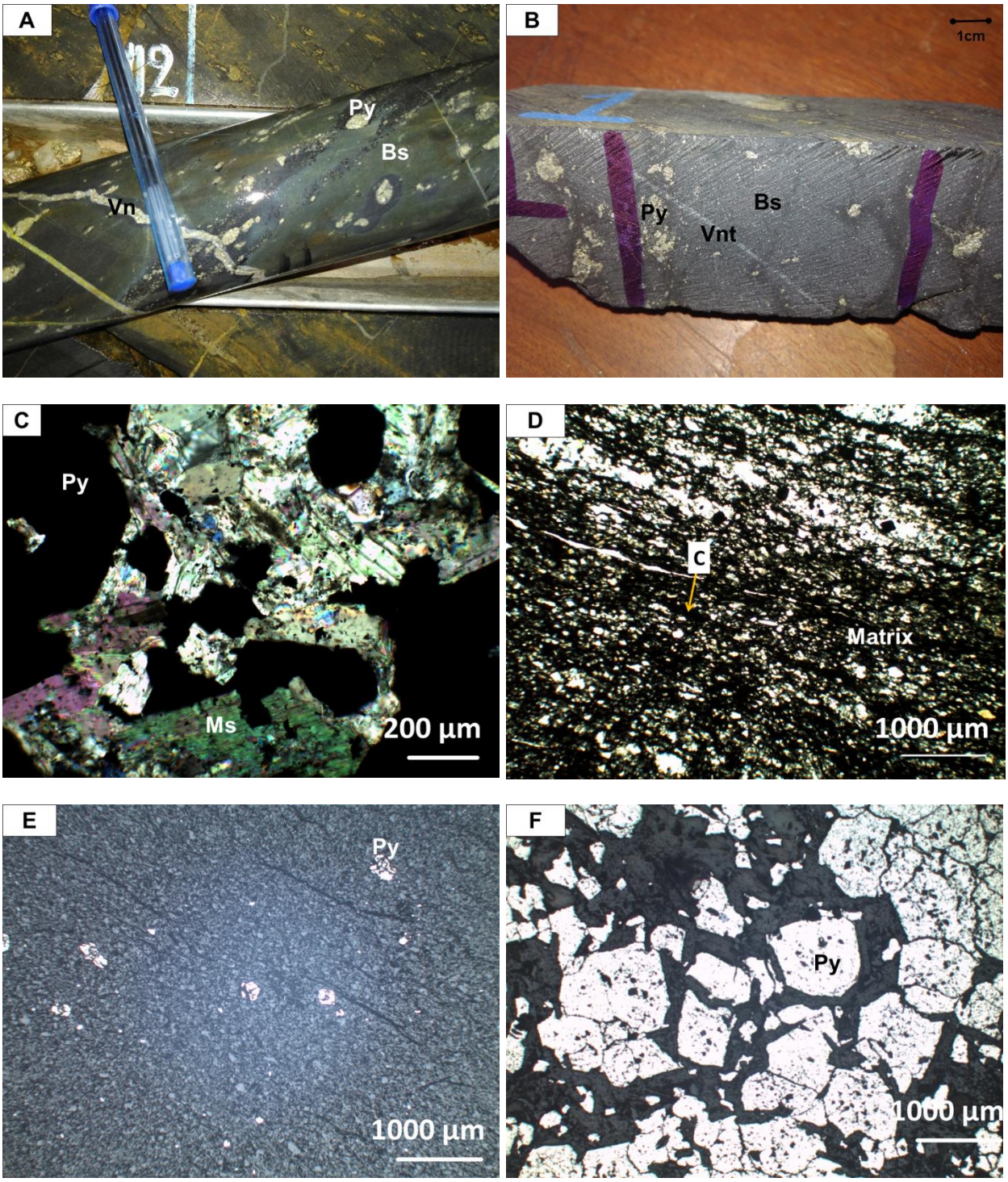

Figure 8. MBS1, black shale (Bs) sample. A. Lens-like nodules of pyrite (Py) and crosscutting quartz-pyrite-rich vein (Vn); B. Pyrite and crosscutting quartz veinlet (Vnt) in black shale rock matrix, suggesting sulphide growth prior to vein formation; C. Polished section in transmitted light showing pyrite (Py) in muscovite (Ms)-rich matrix within sulphide-rich lens; D. Laminated black shale matrix with carbon (C) streaks under transmitted light; E. Fine-grained euhedral and subhedral pyrite (Py) randomly distributed in the black shale matrix; F. Anhedral and subhedral pyrite within sulphide-rich lens nodule.

2. **MBS3A**

Black shale sample MBS3A was collected at 121 m depth from the TDD057 core from a 25.78 m thick fine-grained black shale unit (Figure 9A) interlayered with an upper 10.78 m thick and a lower 0.47 m thick feldspar-rich granitoid intrusive sill. The sample was taken at 11.7 m below the upper granitoid sill. The black shale is formed of laminated fine-grained matrix and sulphide-rich lenses. Thin quartz- and albite-rich veinlets crosscut the lamination at a high angle.

The black shale matrix consists of anhedral abundant fine-grained quartz of about 120 µm and albite of 220 µm in diameter, and extremely fine non-crystalline carbon occurring along the lamination. The carbon defines the lamination. Albite is commonly slightly altered to sericite. Rare fine-grained tourmaline measuring about 30 µm occurs occasionally in the matrix (Figure 9B). Subhedral to anhedral rutile of up to 160 µm size is randomly distributed within the matrix. Pyrite of predominantly subhedral and euhedral shape and with sizes between 30 to 400 µm is randomly distributed in the matrix.

Sulphide-rich lenses are characterized by pyrite clusters in a quartz-albite-rich matrix that also contains some fine-grained rutile (Figure 9C&F). Tourmaline is locally distributed in the albite-rich matrix and measures about 50 µm in size. Carbonate is occasionally distributed in the albite-rich matrix with approximately 300 µm of crystal size (Figure 9C). Pyrite in the lenses occurs as an aggregate of subhedral to anhedral crystals, often slightly elongated in the direction of the lens (Figure 9D). Pyrite in these lenses generally ranges in size from 40 µm to 1200 µm; however, large crystals are more abundant than fine-grained pyrite. 30 µm fine-grained rutile, albite and approximately 30 µm sized chalcopyrite are found in inclusions within pyrite in these lenses, suggesting growth at a time when metamorphism already had formed these matrix minerals. A 15 µm native **gold** grain is present along the contact zone between two pyrite crystals within the pyrite-rich lens (Figure 9E). There is a clear spatial relationship between this gold flake and pyrite, but this relationship is genetically inconclusive.

60 µm thick veinlets contain quartz and albite of approximately 40 µm grain size but no pyrite. They crosscut the lamination and the sulphide-rich lenses at a high angle, though overlying by pyrite in the sulphide-rich lenses (Figure 9C).

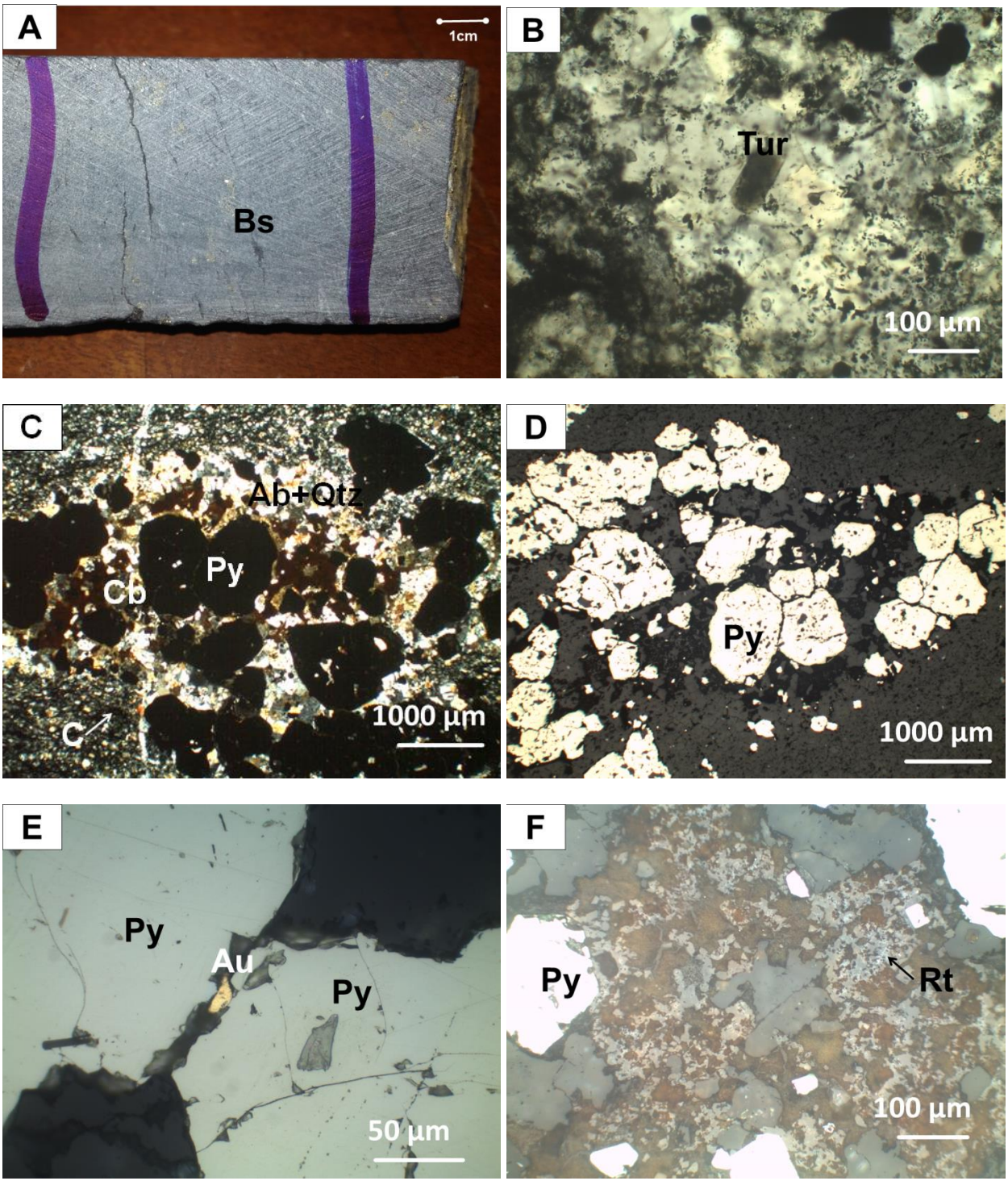

Figure 9. MBS3A; black shale sample. A. Black shale (Bs) sample (2.5 inch core); B. Tourmaline (Tur) in black shale rock matrix under transmitted light of the polished section; C. Polished section in transmitted light showing pyrite (Py) in albite (Ab), quartz (Qtz), carbonate (Cb) and carbon (C) matrix; D. Anhedral to subhedral disseminated pyrite(Py) in black shale under reflected light; E. Gold (Au) at the interface between pyrite crystals (Py); F. Fine-grained rutile (Rt) between pyrite.

3. **MBS3B**

Black shale sample MBS3B was collected at 121 m depth from the TDD057 core from a 25.78 m fine grained black shale unit (Figure 10A) interlayered with an upper 10.78 m thick and a lower 0.47 m thick feldspar-rich granitoid intrusive sill. The sample was taken 11.7 m below the upper granitoid sill. The section consists of black shale formed of laminated fine-grained matrix and sulphide-rich lenses. A 5.6 mm thick quartz- and carbonate-rich vein crosscuts the lamination and the sulphide-rich lenses at a high angle (Figure 10A). 60 µm to 20 µm thick quartz- and albite-rich veinlets crosscut the lamination at a low angle and some are sub-parallel to it.

The black shale matrix consists of anhedral fine-grained 120 µm quartz and 140 µm albite, and the organic matter consists of extremely fine non-crystalline carbon. Albite commonly shows an alteration to sericite. Fine-grained subhedral to euhedral pyrite crystals, commonly of cubic shape and generally disintegrated, are randomly distributed in the matrix and range in size from 40 to 400 µm (Figure 10D). 10 to 60 µm anhedral rutile occurs as inclusions in pyrite and / or randomly distributed in the matrix.

A 8.5 mm thick lamination-parallel sulphide-rich lens consists of an aggregate of annealed anhedral to subhedral pyrites within a albite-quartz-rich matrix. These annealed anhedral to subhedral pyrites range in size from 80 µm to 1040 µm whereas the albite matrix crystals are 30 to 150 µm thick in size. Up to 160 µm arsenopyrite is intergrown with the annealed anhedral to subhedral pyrite (Figure 10C). Fine-grained 70 µm rutile and 40 µm chalcopyrite occur as inclusions within the annealed anhedral to subhedral pyrite. Fine-grained quartz is randomly distributed in the albite-rich matrix and measures approximately 50 µm. The organic matter is less abundant or often absent in the lens. Rare tourmaline of approximately 20 µm by 70 µm size is randomly distributed in the albite-rich matrix. A 10 µm thick native **gold** grain forms an inclusion in anhedral pyrite of the sulphide lens (Figure 10E). Another 15 µm **gold** grain occurs in the lens' albite-rich matrix close to the crosscutting quartz- and carbonate-rich vein (Figure 10F).

60 µm to 20 µm thick veinlets consisting of anhedral quartz-rich and minor albite crystals are randomly distributed in the matrix. The quartz within the veinlet consists of crystals of approximately 40 µm size, whereas albite crystals ranges from 15 µm to 60 µm thick in size.

A 5600 µm thick quartz vein with abundant carbonate crosscuts the sulphide lens at a high angle (Figure 10B). Toward the rims of the vein, quartz crystals develop a comb structure with crystals sizes of approximately 1760 by 400 µm. In the core of the quartz vein large anhedral to euhedral carbonate crystals of about 1440 µm size form straight grain boundaries, with on one side, large quartz, suggesting their precipitation at the same time (Figure 10B), and, on the other side, fine-grained 720 to 160 µm fractured quartz associated with 640 to 200 µm albite, suggesting a tectonic reactivation process. Rare subhedral to euhedral pyrite, often associated with intergrown arsenopyrite, is randomly distributed in the quartz vein and range in size from 160 to 800 µm.

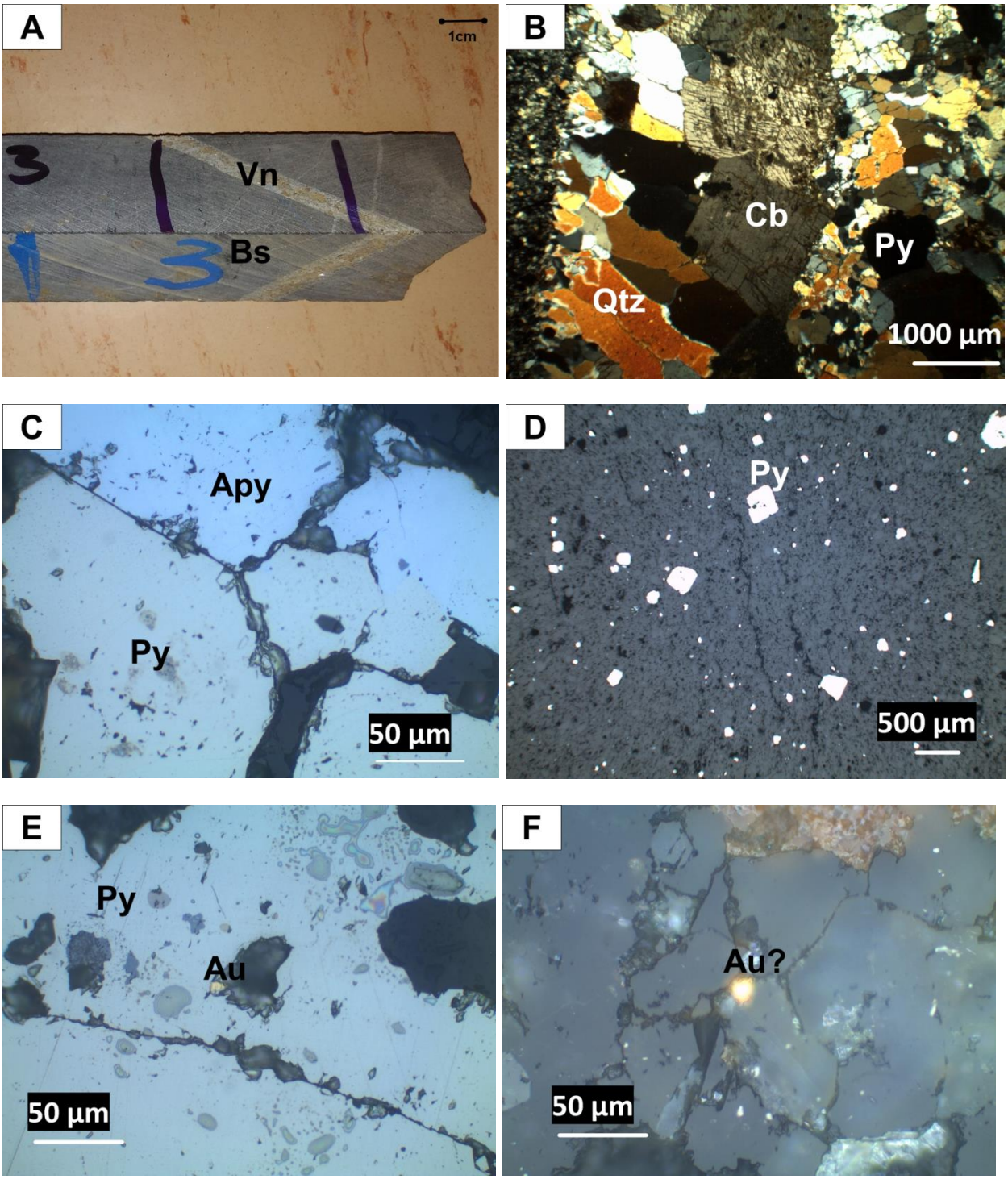

Figure 10. MBS3B; black shale sample. A. Black shale (Bs) rock sample crosscut by quartz vein (Vn); B. carbonate (Cb) in quartz (Qtz) vein hosted in black shale rock matrix under transmitted light; C. Polished section in reflected light showing pyrite (Py) and arsenopyrite (Apy); D. Euhedral to subhedral disseminated pyrite (Py) in black shale matrix under reflected light; E. Gold (Au) inclusion within pyrite (Py); F. Possible gold (Au?) within black shale matrix.

4. **MBS6**

Black shale sample MBS6 was collected at 170.5 m depth from the TDD040 core from a 219.57 m thick fine-grained black shale unit (Figure 11A) interlayered with an upper 5.9 m thick and a lower 28 m thick feldspar-rich granitoid intrusive sill. The sample was taken 86.47 m above the lower granitoid sill. The section consists of black shale comprising laminated fine-grained matrix and sulphide-rich lenses emplaced along the lamination trend. An albite-rich vein crosscuts the sulphide-rich lenses at high angle. Also, veinlets formed of quartz and albite crosscut the lamination (Figure 11A).

The fine-grained black shale matrix is formed of albite and quartz of 60-70 µm size, and extremely fine non-crystalline carbon. Muscovite is commonly oriented parallel to the lamination (Figure 11C) and ranges in size from 100-370 µm in length and 30-60 µm in width. Subhedral to euhedral pyrite grains of about 10-300 µm are randomly distributed in the fine-grained matrix (Figure 11F). Carbon is less abundant in the vicinity of the vein and abundant away from the vein, where it forms a major part of the matrix. Rutile is randomly distributed within the matrix and measures about 40 µm in size.

Sulphide-rich lenses of approximately 800 µm thickness consist of aggregates of sulphide, predominantly of pyrite, within a medium-grained 160 µm albite-rich and 100 µm quartz matrix. Pyrite in the lens occurs as annealed anhedral crystals (Figure 11E). About 80 µm arsenopyrite grains are intergrown with pyrite in the quartz and albite-rich matrix of the lens.

The albite-rich vein consists of anhedral to subhedral albite forming coarse-grained crystals in the core of the vein which are about 760 µm by 260 µm in size, and fine-grained crystals that are about 60 µm by 40 µm thick toward the contact of the vein with the black shale host rock. A coarse-grained muscovite grain of approximately 800 µm in size occurs in the core of the vein (Figure 11B). Rare muscovite of about 600 µm by 200 µm in size is randomly distributed in the albite vein. Rare fine-grained quartz of approximately 200 µm is scattered within the albite vein. Up to 450 µm size of subhedral to euhedral pyrite, commonly of pyritohedron shape, occurs in the vein predominantly near the contacts of the vein with sulphide-rich lenses (Figure 11D).

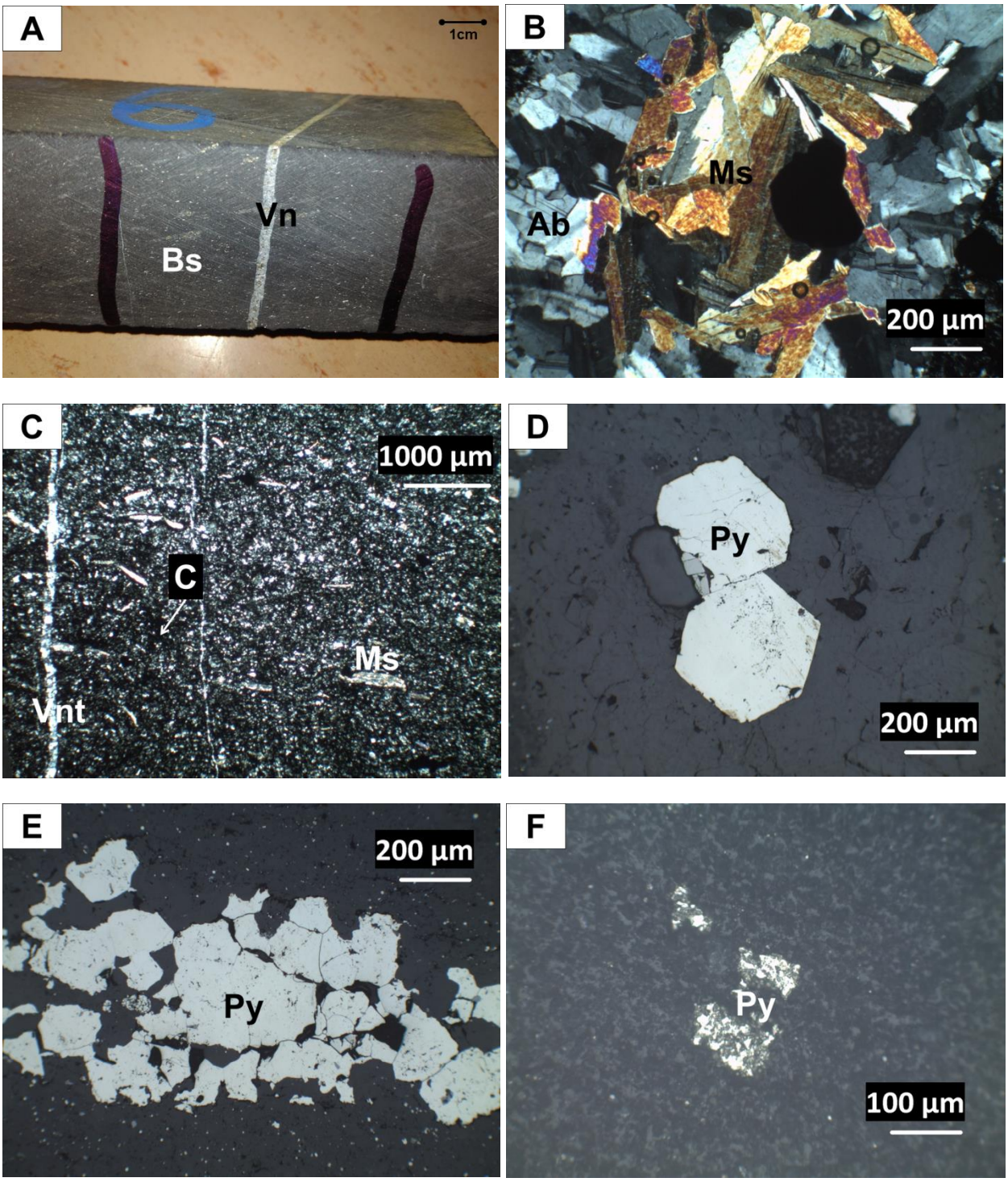

Figure 11. MBS6; black shale sample. A. Black shale (Bs) rock sample crosscut by albite vein (Vn) and hosting sulphide-rich lens; B. Muscovite-rich (Ms) crystal in albite (Ab) vein under transmitted light; C. Rock matrix with scattered muscovite (Ms) and carbon (C) and crosscut by veinlet (Vnt) in transmitted light; D. Euhedral pyrite (Py) in the albite vein under reflected light; E. Anhedral pyrite (Py) in the sulphide-rich lens body under reflected light; F. Euhedral to subheral pyrite (Py) within the rock matrix under reflected light.

5. **MBS15**

Black shale sample MBS15 was collected at 275.7 m depth from the TDD052 core from a 67.95 m fine-grained black shale unit (Figure 12A) interlayered with an upper 23.47 m thick and a lower 14.91 m thick feldspar-rich granitoid intrusive sill. The sample was taken 21 m below the upper granitoid sill. The section consists of black shale composed of laminated fine-grained matrix with randomly distributed sulphides and crosscut by a carbonate-rich vein and quartz-rich veinlets that are randomly oriented in the matrix (Figure 12A).

The black shale matrix is formed of fine-grained anhedral quartz, albite and organic matter. Quartz and albite in the black shale matrix have a size of approximately 100 µm. Tourmaline is randomly distributed in the matrix with an average size of 100 µm in length and 20 µm thickness (Figure 12B). Up to 1680 µm carbonate overgrows the matrix minerals and have fine-grained albite as inclusions. The organic matter consists of extremely fine non-crystalline carbon abundantly distributed in the matrix. Abundant subhedral to euhedral pyrite is randomly distributed within the matrix and measures approximately 16 µm to 300 µm. The subhedral to euhedral pyrite commonly appears as disintegrated by dissolution or as an aggregation of fine-grained crystals forming a broad euhedral form away from the vein selvedge (Figure 12E), whereas it is compact in the vein selvedge (Figure 12D). Rare fine-grained rutile (60 µm) is either intergrown with subhedral to euhedral pyrite, or is spread out in the matrix (Figure 12F).

The veinlet is composed of abundant 20 µm to 100 µm anhedral quartz crystals and minor fine-grained albite and carbonate. Thinner veinlets commonly merge into one thicker veinlet.

The vein shows a triangular texture and measures about 1280 µm in thickness. It consists of 1200 µm large carbonate crystals forming the core of the vein, and fine-grained quartz and albite occurring toward the contacts of the vein with the black shale. Quartz and albite grain sizes are approximately 120 µm and 560 µm respectiveley (Figure 12C).

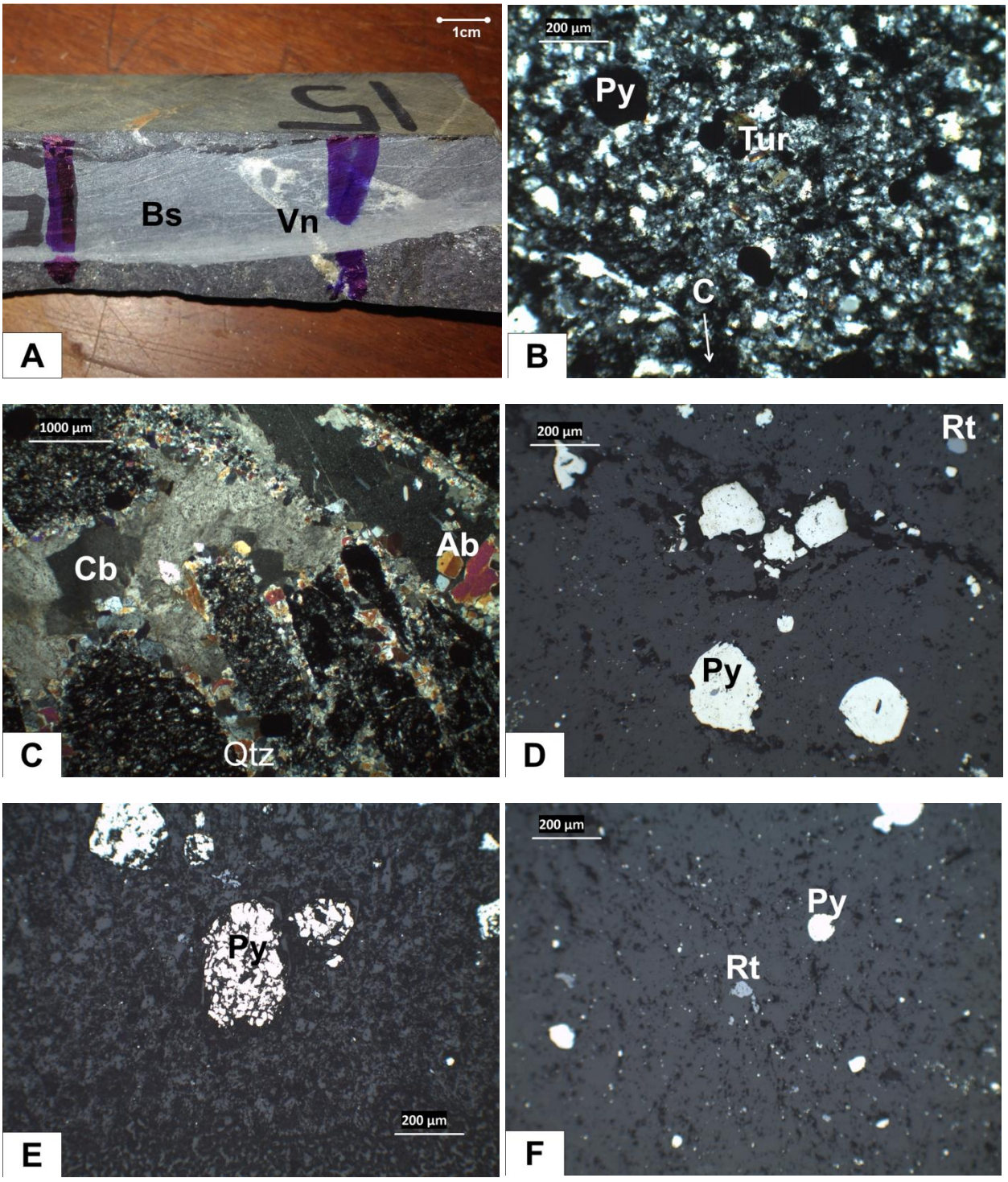

Figure 12. MBS15; black shale A. Black shale (Bs) rock sample crosscut by carbonate-rich vein (Vn); B. Quartz-albite-rich matrix with tourmaline (Tur), carbon (C) and pyrite (Py) under transmitted light; C. Carbonate-rich (Cb) vein with albite (Ab) in transmitted light; D. Anhedral pyrite (Py) under reflected light; E. Disintegrated euhedral pyrite (Py) in the black shale matrix under reflected light; F. Pyrite (Py) and rutile (Rt) within the rock matrix under reflected light.

III.1.2. Unmineralized black shale (UMBS) samples

6. UMBS4A

Black shale sample UMBS4A was collected at 83.5 m depth from the TDD049 core from a 62.65 m fine-grained black shale unit (Figure 13A) interlayered with an upper 1.34 m thick and a lower 0.75 m thick feldspar-rich granitoid intrusive sill. The sample was taken 7.52 m above the lower granitoid sill. This section is composed of black shale formed of laminated fine-grained matrix and a nearly spherical sulphide-rich lens. A quartz-rich vein crosscuts the sulphide-rich lens at a high angle (Figure 13A).

The black shale matrix consists of fine-grained anhedral crystals of quartz measuring approximately 60 µm, albite of about 80 µm and organic matter consisting of extremely fine non-crystalline carbon (Figure 13C). Albite in places shows sericitic alteration. Randomly distributed subhedral to euhedral pyrite is commonly disintegrated and measures about 80 µm to 640 µm (Figure 13E). Fine-grained quartz and albite are commonly found as inclusion within pyrite. Fine-grained anhedral rutile (<160x20 µm) is randomly distributed in the matrix or is intergrown with pyrite.

The sulphide-rich lens measures approximately 3200 µm in thickness and consists of an aggregate of pyrite in an anhedral albite-quartz matrix (Figure 13D). Within the lens-shaped segregation, quartz (~140 µm) and albite (~200 µm) are associated with pyrite. Carbon, which is abundant in the matrix, is absent in this segregation. Albite shows occasionally a sericitic alteration. The lens' pyrite consists of annealed anhedral crystals and commonly contains albite as inclusions.

The vein that intersects the black shale and a large pyrite lens (Figure 13A) is 2.5 mm thick and consists mainly of quartz and rare albitic plagioclase (Figure 13B). Quartz in the core of the vein is elongated and about 1.5 x 0.5 mm in size. Towards the vein margins the quartz grain size decreases to about 80 x 20 µm. Euhedral pyrite may show inclusion-rich cores and inclusion-free rim zones (Figure 13F). Inclusions in the core zone may outline angular surfaces, possibly indicating smaller euhedral grains. This may suggest that the core was formed by an agglomeration of crystals that were later overgrown by a single coherent grain.

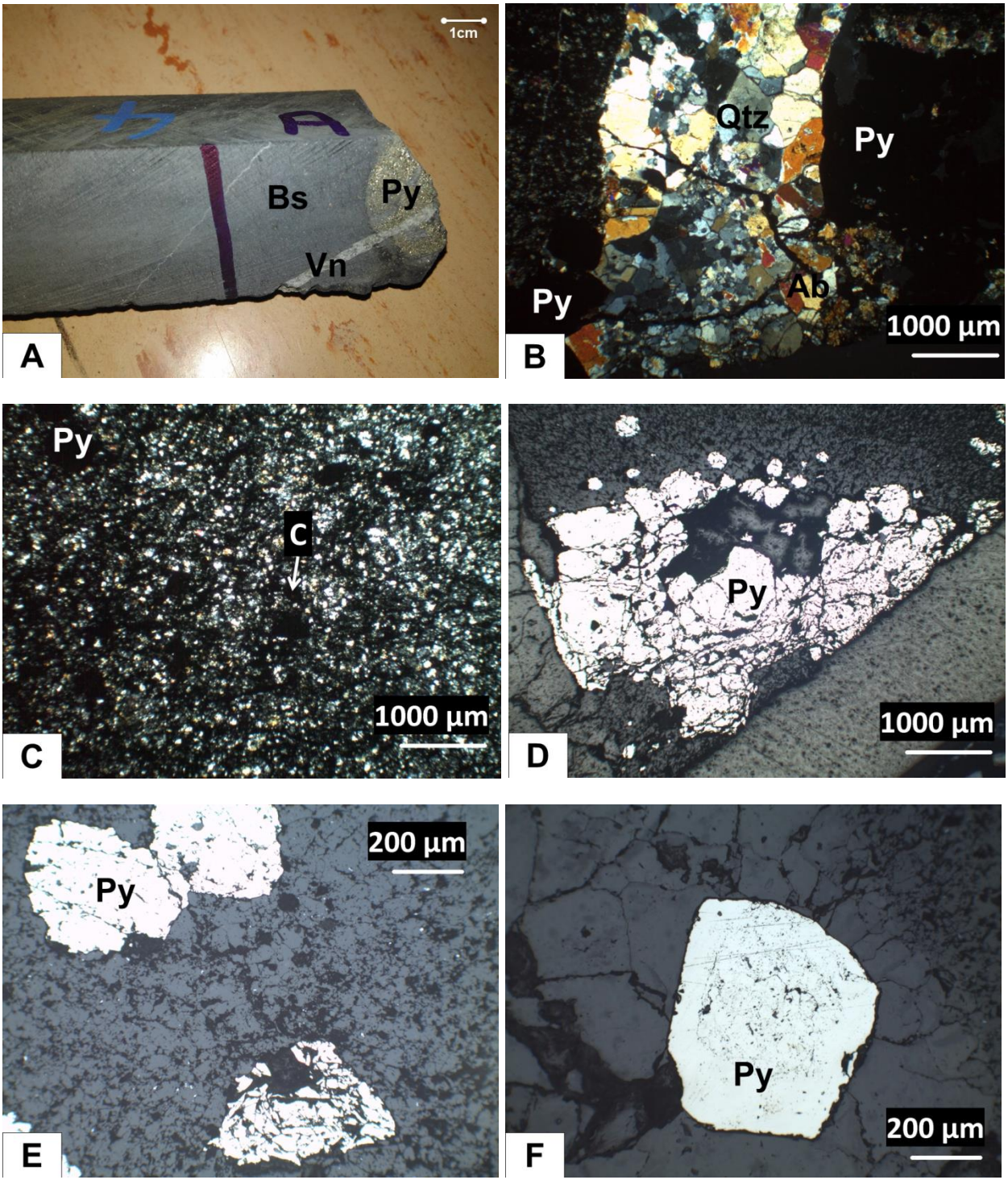

Figure 13. UMBS4A black shale. A. Black shale (Bs) rock sample crosscut by quartz vein (Vn) and hosting a sulphide-rich lens of predominantly pyrite (Py) phase; B. Quartz (Qtz) vein in contact with the sulphide-rich lens of predominantly pyrite (Py) phase under transmitted light in polished section; C. Quartz-albite-rich matrix with carbon (C) in transmitted light; D. Anhedral pyrite (Py) in the sulphide-rich lens under reflected light; E. Subhedral to euhedral pyrite (Py) in the black shale matrix under reflected light; F. Zoned pyrite (Py) with slightly disintegrated core zone within the vein under reflected light.

7. **UMBS4B**

Black shale sample UMBS4B was collected at 83.5 m depth from the TDD049 core from a 62.65 m fine-grained black shale unit (Figure 14A) interlayered with an upper 1.34 m thick and a lower 0.75 m thick feldspar-rich granitoid intrusive sill. The sample was taken 7.52 m above the lower granitoid sill. The section consists of black shale formed of laminated fine-grained matrix with randomly distributed sulphides.

The black shale matrix is composed of approximately 80 µm abundant anhedral quartz and 140 µm albite. Rare tourmaline of about 50 µm by 20 µm is randomly distributed within the matrix (Figure 14B). Abundant fine non-crystalline carbon is distributed in the matrix.

80 µm to 320 µm subhedral to euhedral pyrite is randomly distributed in the matrix. This pyrite is commonly fragmented and partly dissolved (Figure 14C&D). Rutile occurs as randomly distributed fine-grained anhedral crystals of approximately 18 µm in the matrix (Figure 14D).

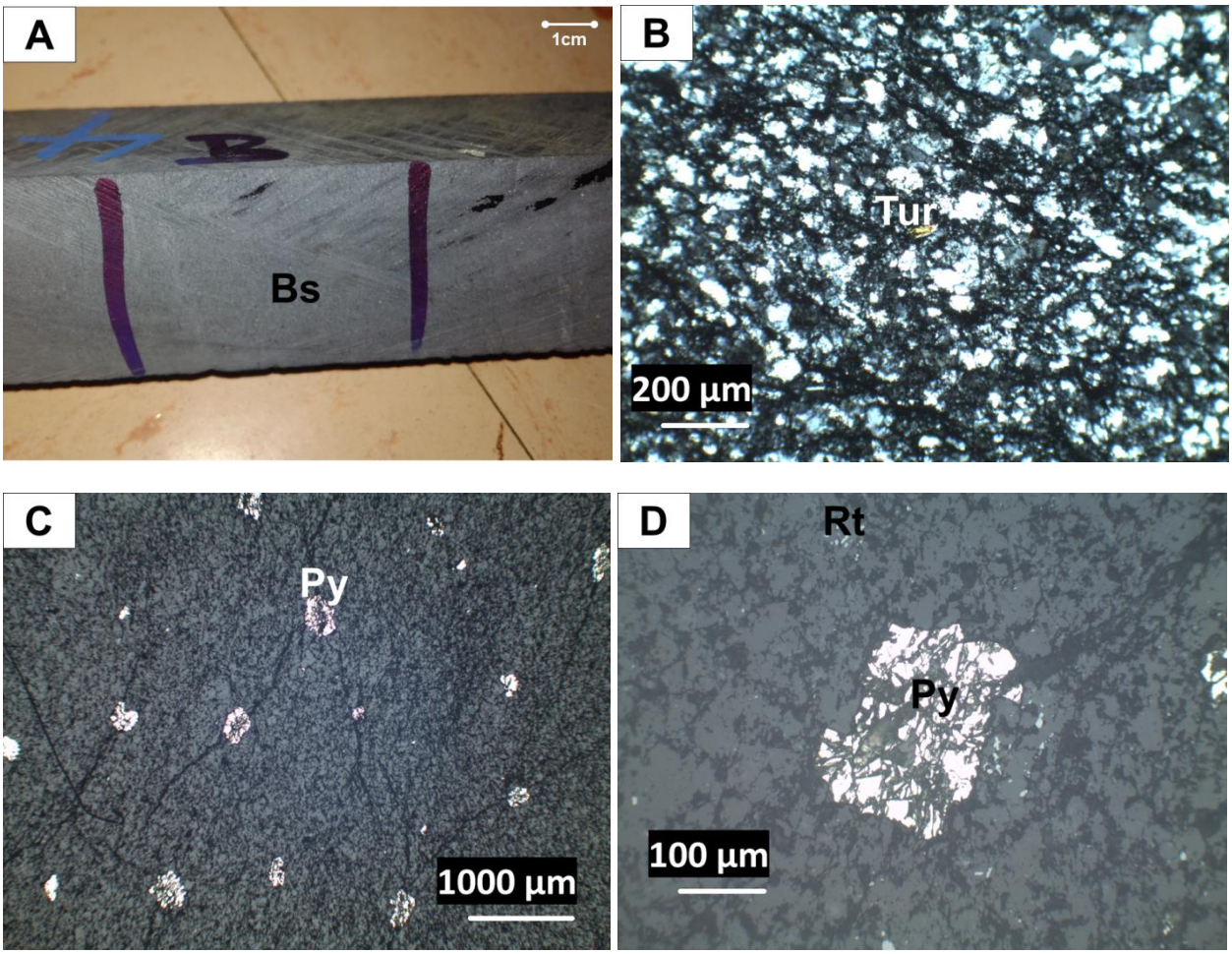

Figure 14. UMBS4B; black shale rock sample and associated polished sections. A. Black shale (Bs) rock sample; B. Tourmaline (Tur) within black shale matrix under transmitted light; C. Euhedral to subhedral pyrite (Py) within black shale matrix in reflected light; D. Euhedral disintegrated pyrite (Py) in the matrix under reflected light.

8. **UMBS9**

Sample UMBS9 was collected at 316 m depth from the TDD036 core from a 56.44 m fine grained black shale unit extending downward away from the end of the drill hole (Figure 15A) and interlayered with an 8.93 m thick feldspar-rich granitoid intrusion sill on top. The sample was taken 51.03 m below the granitoid sill. The section from which the sample was taken includes a sequence of black shale including carbonaceous mudstone and thin layers of siltstone, and granitoid units. The black shale shows a laminated fine-grained matrix with randomly distributed sulphides.

The black shale matrix consists of fine-grained quartz (20 to 100 µm) and organic matter. Rare muscovite, measuring about 160 µm by 50 µm, is commonly oriented parallel to the lamination (Figure 15B). The organic matter consists of extremely fine non-crystalline carbon forming subparallel streaks along the lamination.

Anhedral pyrrhotite is randomly distributed within the matrix. The pyrrhotite appears like patches of crystals locally elongated along the lamination (Figure 15C&D). The pyrrhotite crystals are generally 20 µm to 260 µm in size. Rare fine-grained rutile (~60 µm) is randomly distributed in the matrix and / or in contact with pyrrhotite. Euhedral arsenopyrite of about 150 µm is in contact with pyrrhotite (Figure 15F). Sample UMBS9 shows microscopically domains rich in phyllosilicates with low quartz proportions. Here the phyllosilicates are well-aligned, forming a penetrative foliation. These foliated layers alternate with quartz-rich layers where phyllosilicates are randomly oriented and form only small volume proportions (Figure 15E). This pattern is interpreted as in-situ segregation of quartz by dissolution and precipitation in presence of a hydrothermal fluid phase. In the quartz-rich layers sulphides (pyrrhotite and arsenopyrite) are also much more abundant than in the foliated layers (Figure 15D). This implies that the segregation of quartz also mobilized sulphides, which precipitated together with quartz close to their primary source.

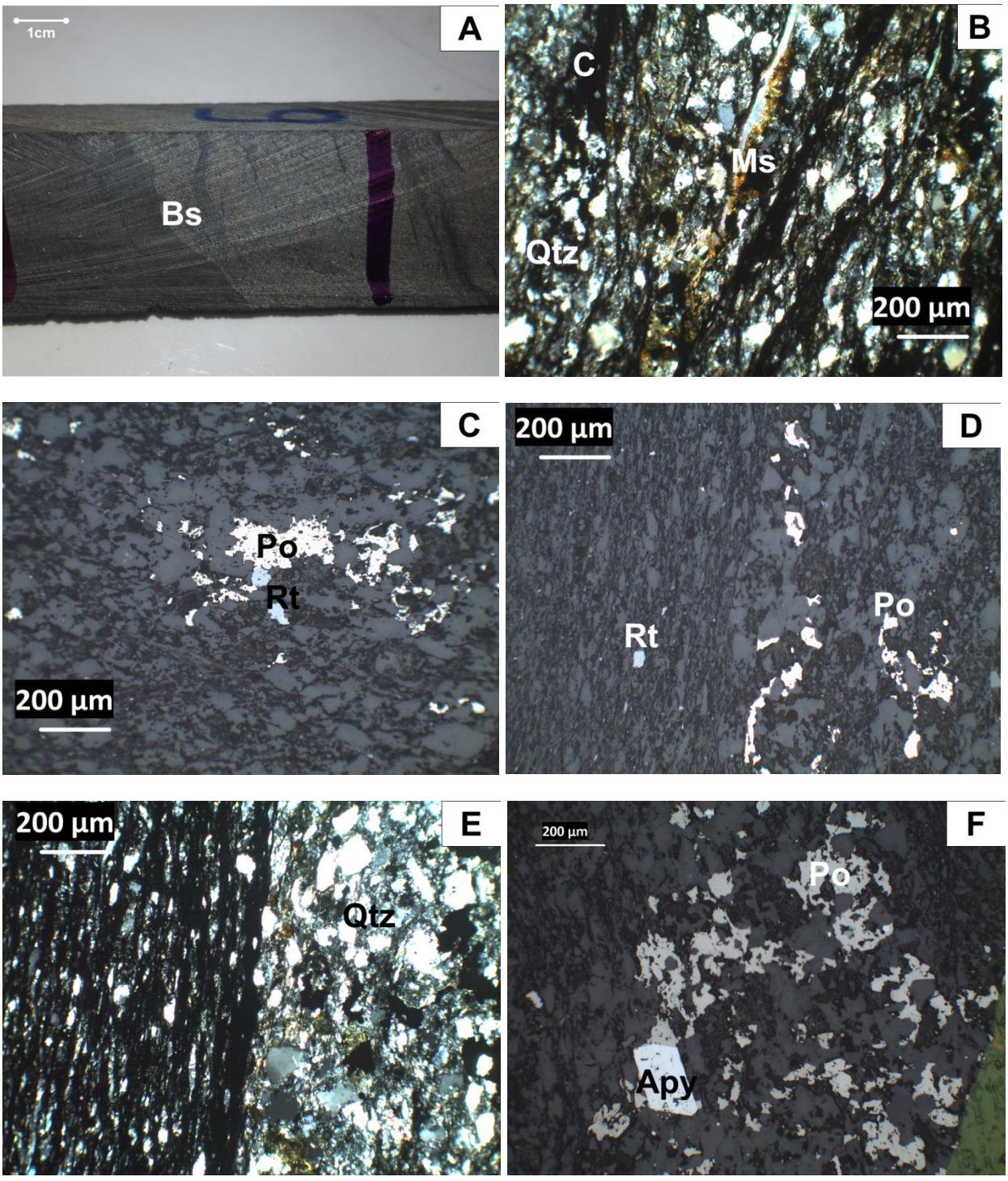

Figure 15. UMBS9 black shale. A. Black shale (Bs) rock sample; B. Muscovite (Ms) scattered in quartz-rich (Qtz) and carbon (C) matrix under transmitted light; C. Anhedral pyrrhotite (Po) and rutile (Rt) within the rock matrix in reflected light; D. Anhedral pyrrhotite (Po) -rich zone and pyrrhotite-free zone containing rutile (Rt) under reflected light; E. Phyllosilicate foliated layers alternating with quartz-rich layers in transmitted light; F. Arsenopyrite (Apy) in contact with pyrrhotite (Po) under reflected light.

9. **UMBS11**

Black shale sample UMBS11 was collected at 135.5 m depth from the TDD035 core from a 147.46 m thick fine-grained black shale unit (Figure 16A). In this section there are an upper 4.76 m thick and a lower 17.83 m thick feldspar-rich granitoid intrusive sills. The sample was taken 63.75 m below the upper granitoid sill and 83.91 m above the lower one. The thin section consists of black shale formed of laminated fine-grained matrix with spherical nodules randomly distributed in the matrix and commonly rich in sulphide.

The black shale matrix is composed of abundant anhedral fine-grained quartz of approximately 20 µm to 100 µm and fine non-crystalline carbon. ~300 µm muscovite grains are commonly oblique to the lamination of the matrix (Figure 16B), suggesting late growth under kinematically static conditions. About 80 µm subhedral pyrite is locally distributed in the matrix (Figure 16F). Rare fine-grained rutile is locally distributed in the matrix.

The spherical nodules consist of nodules of fine-grained anhedral quartz and abundant carbon with aggregates of fine-grained anhedral pyrite of approximately 100 µm in size (Figure 16C&D) suggesting a replacement of organic materials deposited during the sedimentation process. These spherical nodules are not deformed nor aligned parallel to the lamination as seen for sulphide-rich lenses. Also, pyrite crystals are not annealed and are of a small size compared to the sulphide-rich pyrite lenses (Figure 16E). The aggregation of anhedral pyrite is commonly found near the contact of the spherical nodules with the black shale matrix.

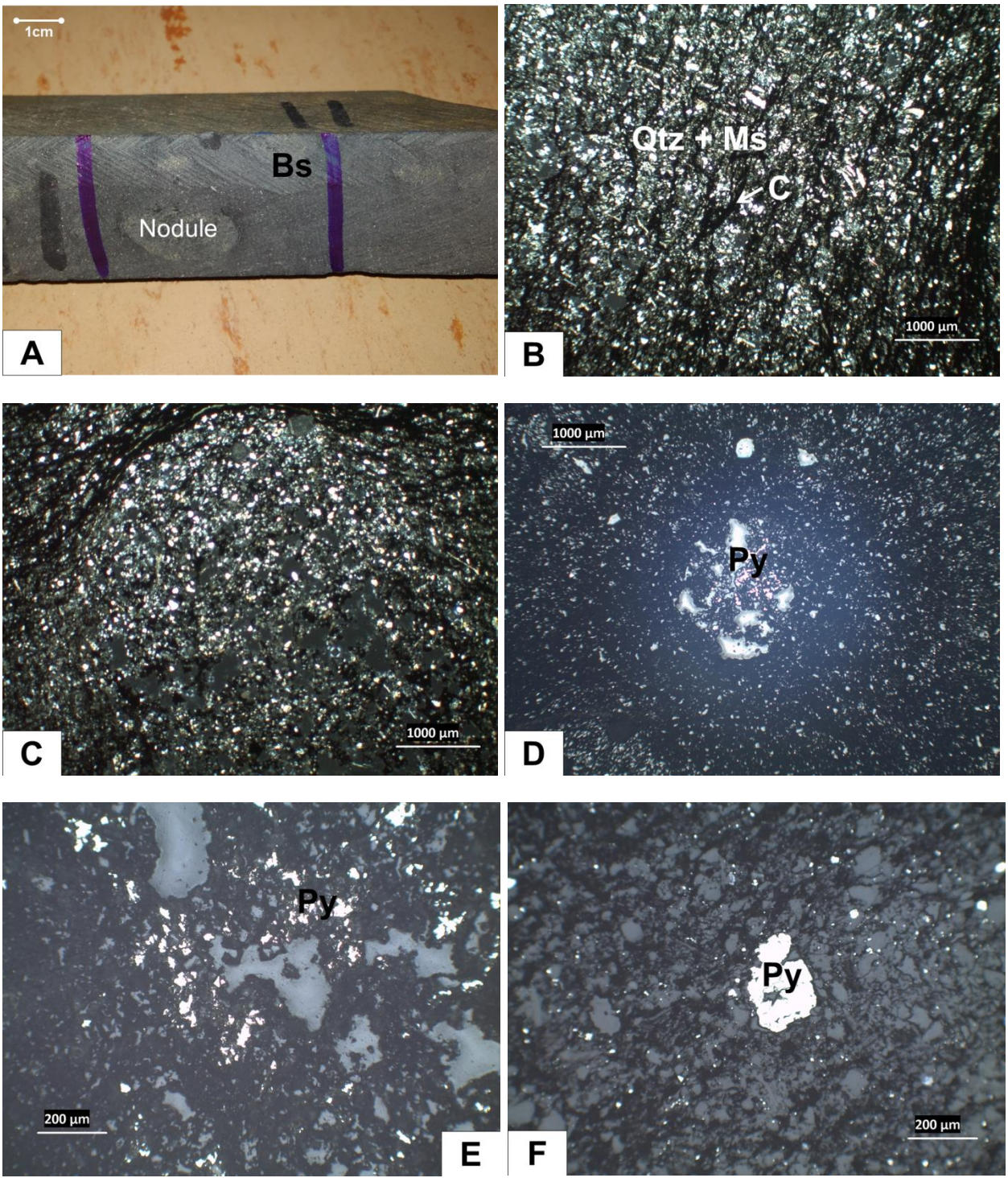

Figure 16. UMBS11 black shale. A. Black shale (Bs) with a ~1.5 cm nodule; B. Quartz-rich (Qtz) rock matrix with carbon (C) and scattered muscovite (Ms) under transmitted light; C. Nodule of quartz-rich matrix under transmitted light; D. Anhedral pyrite (Py) aggregation within the nodule under reflected light; E. Anhedral pyrite (Py) in reflected light; F. Disintegrated euhedral pyrite in the rock matrix under reflected light.

10. UMBS12A

Black shale UMBS12A was collected at 188 m depth from the TDD078 core from a 50.24 m fine-grained black shale unit (Figure 17A). This black shale unit is interlayered with an upper 14.75 m thick and a lower 11.27 m thick feldspar-rich granitoid intrusive sill. The sample was taken 7.74 m below the upper granitoid intrusive sill. The sample UMBS12B (see section below) comes from the same section and same depth of this core. The thin section shows the black shale, which is formed of laminated fine-grained matrix and sulphide-rich lenses which parallel the lamination.

The black shale matrix consists of fine-grained anhedral quartz, abundant albite and organic matter consisting of extremely fine non-crystalline carbon (Figure 17C). Quartz in the matrix has an approximate size of 80 µm to 250 µm, albite has an average size of 120 µm. Subhedral to euhedral pyrite is randomly distributed in the black shale matrix and measures about 20 µm to 170 µm (Figure 17F). Fine-grained anhedral rutile of about 40 µm is randomly distributed within the matrix.

The sulphide-rich lenses consist of aggregates of pyrite in approximately 200 µm quartz and 400 µm albite matrix (Figure 17B). Anhedral pyrite of approximately 2000 µm by 800 µm in size commonly occurs elongated in the direction of the lens (Figure 17D&E). This anhedral pyrite is commonly annealed and commonly has albite as inclusions. Rutile occurs in contact with the lens pyrite.

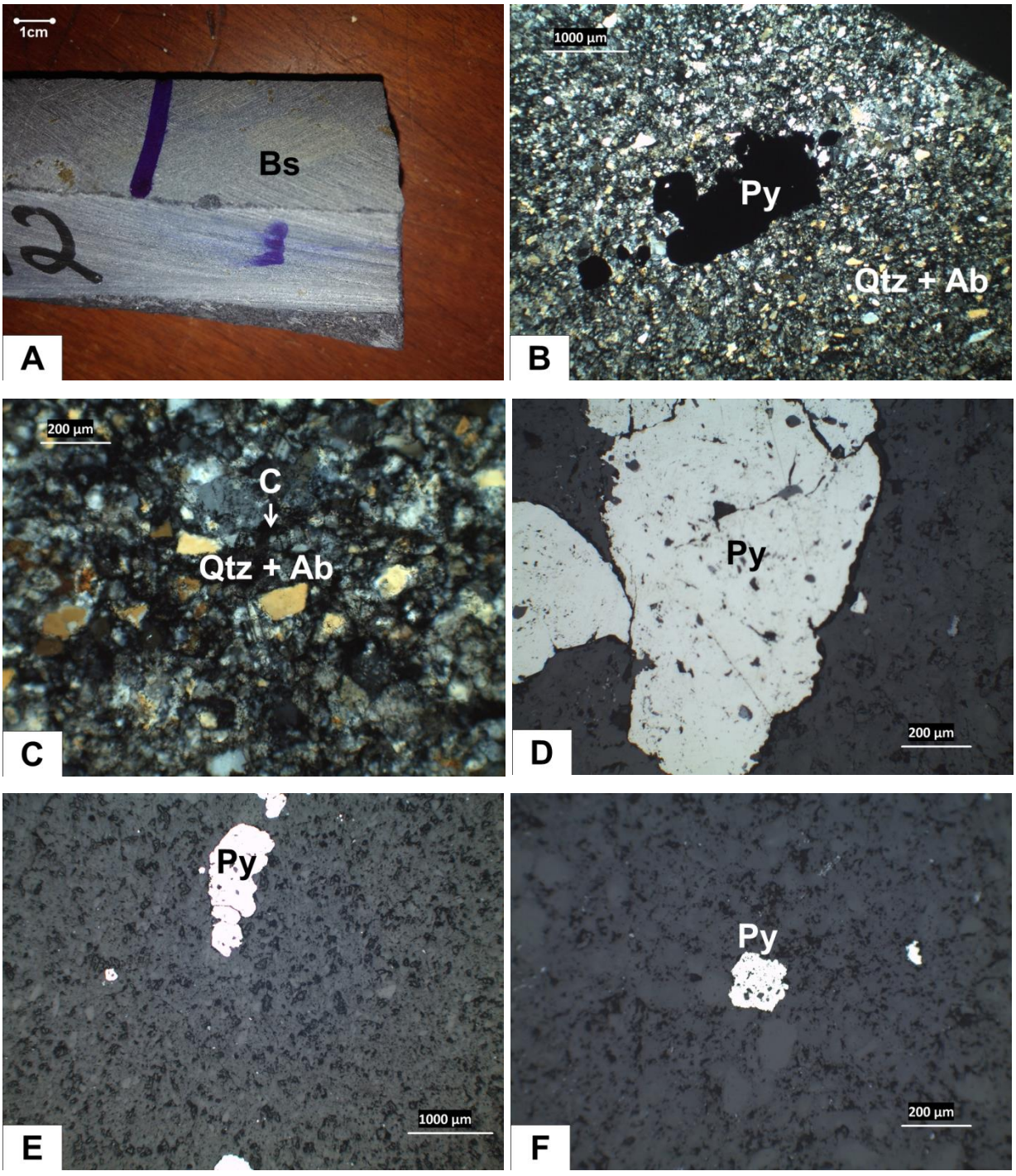

Figure 17. UMBS12A black shale. A. Black shale (Bs) rock sample; B. Pyrite (Py) within quartz (Qtz) and albite-rich (Ab) rock matrix under transmitted light; C. Quartz (Qtz) and albite (Ab) matrix minerals with carbon (C) in transmitted light; D. Anhedral pyrite (Py) in the lens body under reflected light; E. Anhedral pyrite (Py) in reflected light; F. Euhedral pyrite (Py) within the rock matrix under reflected light.

11. UMBS12B

UMBS12B was collected at 188 m depth from the TDD078 core from a 50.24 m fine-grained black shale unit (Figure 18A) interlayered with an upper 14.75 m thick and a lower 11.27 m thick feldspar-rich granitoid intrusive sill. The sample was taken 7.74m below the upper granitoid sill. The thin section consists of black shale formed of laminated fine-grained matrix with a sulphide stringer parallel to the lamination. In addition, quartz-rich veins crosscut the lamination at high and moderate angle (Figure 18A).

The black shale matrix is composed of abundant anhedral fine-grained quartz measuring 20 µm to 400 µm, approximately 200 µm albite and extremely abundant fine non-crystalline carbon. Approximately 140 µm sized anhedral carbonate overgrows both quartz and albite within the black shale matrix (Figure 18B). Rare tourmaline with a size of ~180 µm x 60 µm is randomly distributed in the matrix. Subhedral to euhedral pyrite is randomly distributed in the matrix with crystal sizes ranging from 80 µm to 250 µm (Figure 18F). Rare anhedral rutile, with an average size of 40 µm, is randomly distributed in the matrix.

The sulphide stringer consists of a clustering of anhedral pyrite along a structure parallel to the lamination. The stringer's pyrite occurs in a 100 µm quartz, 180 µm albite, and minor 120 µm carbonate matrix (Figure 18D). Rare tourmaline is found in the black shale matrix near the stringer. The anhedral pyrite commonly forms 160 µm by 100 µm crystals elongated in the direction of the stringer (Figure 18E).

The vein has an average thickness of 900 µm and is composed of abundant quartz, minor albite and carbonate (Figure 18C). Quartz forms a comb texture in the core of the vein with ~460 µm grains, whereas fine-grained quartz with about 40 µm of size occurs towards the rims. Anhedral carbonate overgrows quartz within the vein and measures up to 500 µm. 40 µm thick veinlets, composed almost exclusively of quartz, crosscut the laminated black shale matrix.

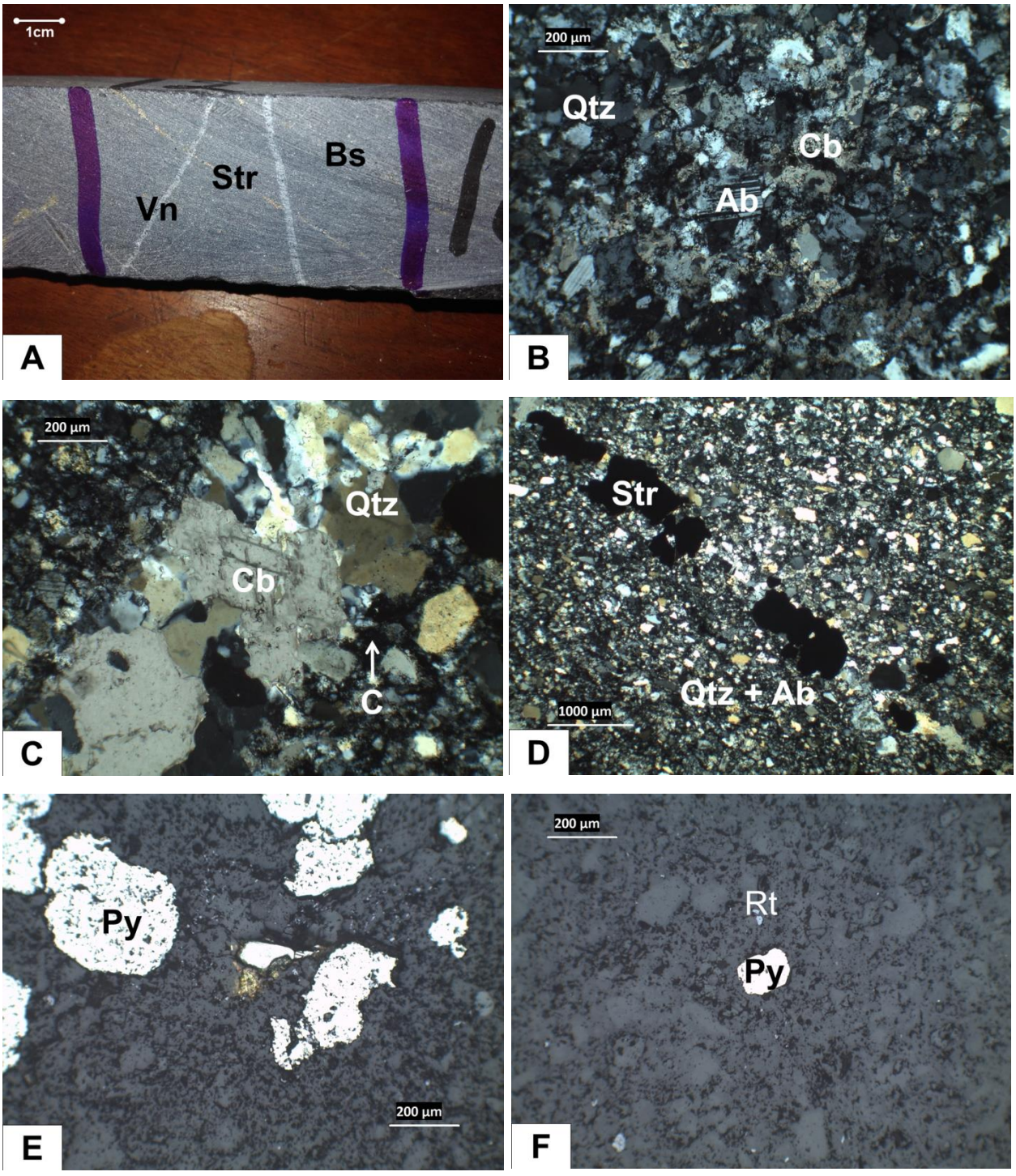

Figure 18. UMBS12B black shale. A. Black shale (Bs) with cross-cutting sulphide stringer (Str) and quartz veins (Vn); B. Quartz (Qtz), albite (Ab) and carbonate (Cb) rock matrix under transmitted light; C. Quartz (Qtz) vein with abundant overgrowing carbonate (Cb) crosscutting the black shale matrix with carbon (C) in transmitted light; D. Sulphide stringer (Str) layered with quartz (Qtz) and albite-rich (Ab) matrix; E. Anhedral pyrite (Py) in reflected light; F. Euhedral pyrite (Py) and rutile (Rt) within the matrix under reflected light.

III.1.3. Mineralized granitoid (MGR) samples

12. MGR17

MGR17 was collected at 159.8 m depth from the TDD058 core from a 9.66 m medium-grained light grey feldspar-rich granitoid intrusion unit (Figure 19A) that is overlain by 151.9 m and underlain by 22 m thick of black shale that also include some carbonaceous mudstone and thin layers of siltstone. The sample was taken 1.76 m above the lower sill contact. The section from which the sample was taken includes a sequence of black shale and other granitoid sills. The thin section shows a porphyritic feldspar-rich granitoid matrix with disseminated sulphides, and a crosscutting carbonate vein.

The granitoid matrix consists of subhedral to euhedral albite with abundant overgrowing anhedral carbonate (Figure 19B). Muscovite is also found locally distributed in the matrix or bordering the carbonate vein. Muscovite occurring around the carbonate vein measures approximately 260 by 50 µm (Figure 19D). Albite varies in size from 140 by 60 µm to 2000 by 1200 µm. Coarse-grained albite crystals commonly show a sericitic alteration. Carbonate crystals range in size from 100 µm to 2000 µm. 150 by 70 µm fine-grained albite crystals are commonly found as inclusions within carbonate crystals. Subhedral to anhedral pyrite of approximately 160 µm to 1040 µm is randomly distributed in the matrix, and is slightly fractured (Figure 19E). Albite is commonly found as inclusions within the pyrite. Pyrite is commonly found in carbonate-rich zones (Figure 19D) suggesting that both pyrite and carbonate precipitated during the same episode. Anhedral pyrite occurs commonly elongated and aligned in the form of stringers (Figure 19F). Rutile is randomly distributed in the matrix. About 20 µm chalcopyrite occurs commonly as inclusions in pyrite.

The carbonate vein consists almost exclusively of carbonate and varies in thickness from 800 µm to 4400 µm (Figure 19C).

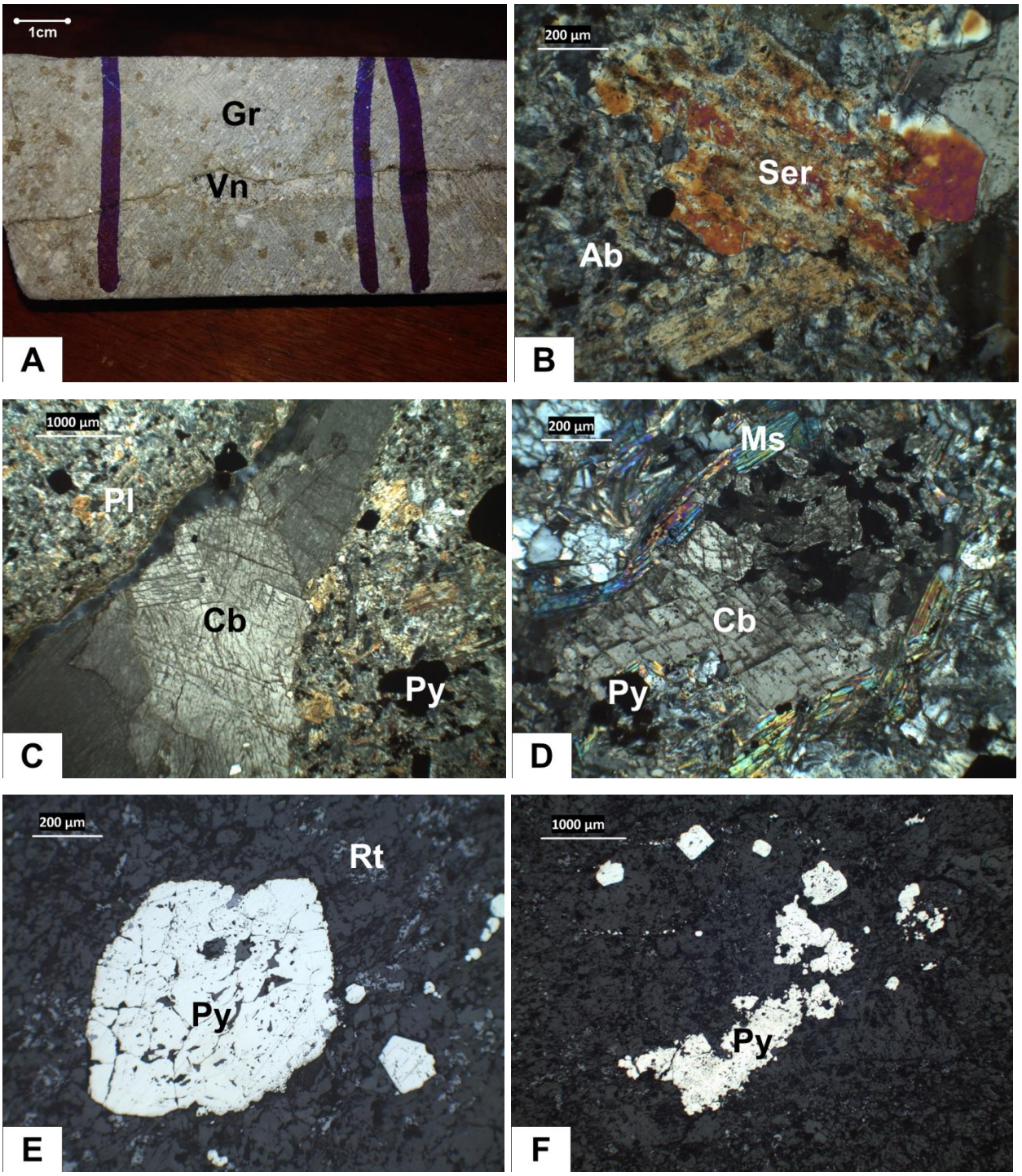

Figure 19. MGR17 granitoid sample. A. Porphyry granitoid (Gr) crosscut by carbonate vein (Vn); B. Albite (Ab) and an alteration of albite to sericite (Ser) under crossed polarized transmitted light; C. Carbonate (Cb) vein in albite-rich (Ab) matrix and disseminated pyrite (Py) in crossed polarized transmitted light; D. Carbonate (Cb) vein containing pyrite (Py) and bordered by muscovite (Ms) under crossed polarized transmitted light; E. Euhedral and subhedral pyrite (Py) in reflected light; F. Anhedral pyrite (Py) commonly elongated in the form of a stringer under reflected light.

13. MGR18

MGR18 was collected at 111.8 m depth from TDD079 core from an 84.77 m medium-grained light grey feldspar-rich granitoid intrusion unit (Figure 20A). In this section there are an upper 48.23 m thick and a lower 41.92 m thick of black shale host rock units that include carbonaceous mudstone and thin layers of siltstone. The sample was taken 1.76 m above the lower black shale unit. The section from which the sample was taken includes a sequence of black shale and granitoid sill units. The thin section consists of a porphyritic medium-grained granitoid matrix with disseminated sulphides.

The granitoid matrix consists of abundant subhedral to euhedral albite with anhedral overgrowing carbonate and rare muscovite (Figure 20B). The albite crystals vary in size from 176 by 120 µm to 2000 by 1600 µm. Coarse-grained albite commonly shows a sericitic alteration. Carbonate overgrows the albite-rich matrix with crystal size varying from 200 µm to 1200 µm. Muscovite of about 300 by 120 µm in size is randomly distributed within the matrix where is mainly associated with pyrite (Figure 20C).

Subhedral to euhedral pyrite, measuring 320 µm to 560 µm of crystal size, is randomly disseminated in the matrix (Figure 20E). Anhedral pyrite commonly occurs aligned in the form of short stringers suggesting an aggregation of sulphide in zones of weakness (Figure 20D). Anhedral pyrite is intergrown with rutile (Figure 20F). Pyrite is commonly found in the vicinity of carbonate crystals. Fine-grained rutile is randomly distributed in the matrix with higher concentrations occurring around altered albite. Rare arsenopyrite occurs in the matrix.

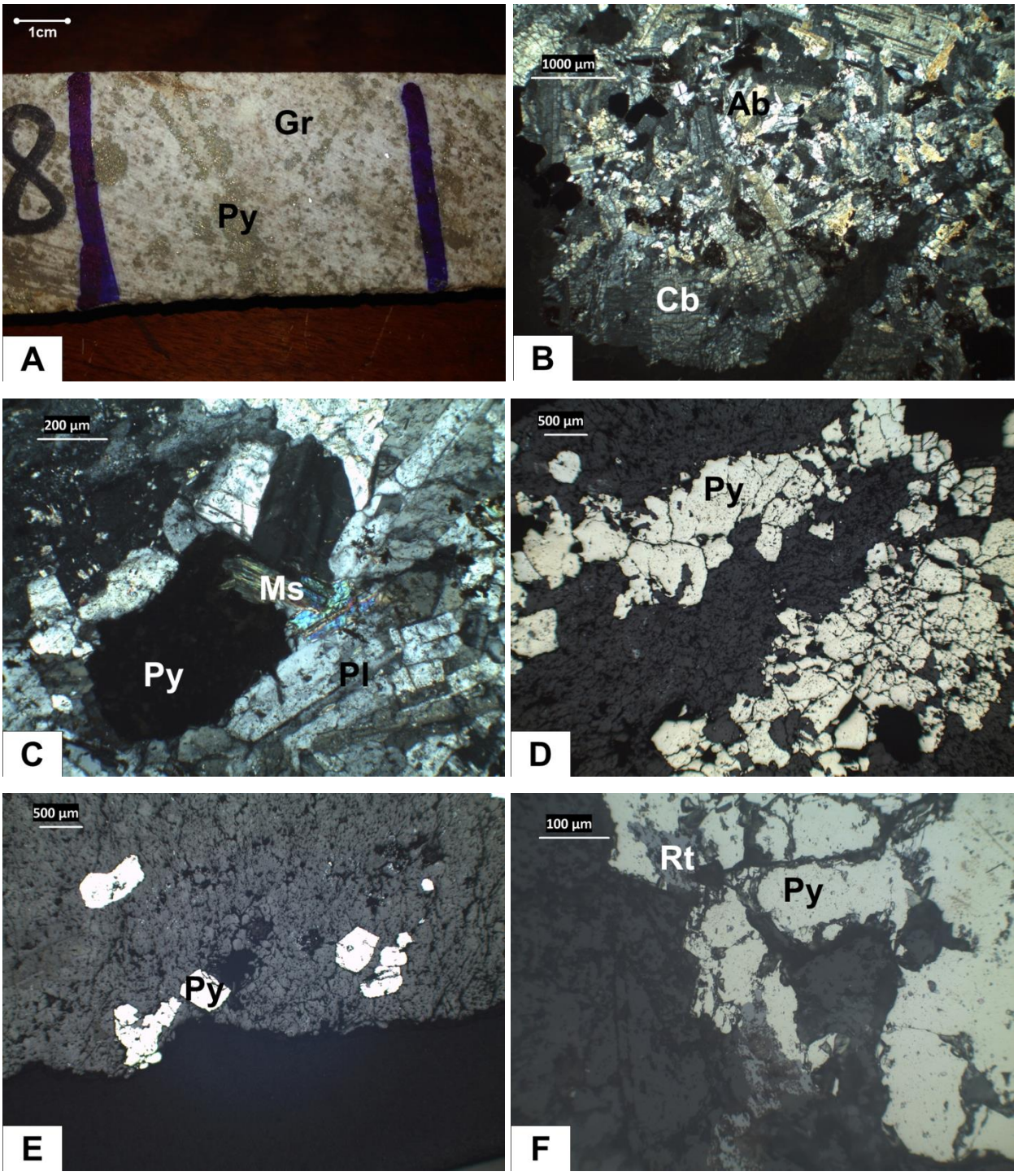

Figure 20. MGR18; granitoid rock sample. A. Porphyry granitoid (Gr) with pyrite stringers and lenses; B. Euhedral albite (Ab) and overgrowing carbonate (Cb) under transmitted light; C. Pyrite (Py), muscovite (Ms) and albite (Ab) in granitoid matrix under transmitted light; D. Anhedral pyrite (Py) in the granitoid matrix under reflected light; E. Euhedral pyrite (Py) in albite-rich matrix under reflected light; F. Intergrowing rutile(Rt) and pyrite (Py) under reflected light.

14. MGR20

MGR20 was collected at 416 m depth of the TDD229 core from an 11.04 m medium-grained light grey feldspar-rich granitoid (Figure 21A) interlayered with an upper 94.26 m thick and a lower 46.27 m thick sequence of black shale, carbonaceous mudstone and intercalated thin layers of siltstone. The sample was taken 3.14 m below the upper black shale unit. The thin section consists of a porphyritic medium-grained feldspar-rich granitoid with disseminated sulphide and carbonate.

The granitoid matrix is constituted of subhedral to euhedral abundant albite with anhedral carbonate and rare quartz (Figure 21B&C). Albite is the major component of the rock matrix and measures approximately 1600 x 2800 µm to 120 x 160 µm. Coarse-grained albite commonly shows an alteration to sericite (Figure 21D). Approximately 100 µm quartz occurs irregularly between the albite crystals. 280 µm to 1700 µm carbonate overgrows small ~80 µm albite. Rutile is randomly distributed in the matrix and mostly concentrated near altered albite.

Subhedral to euhedral pyrite, varying in size from 80 µm to 680 µm, is randomly distributed in the matrix (Figure 21E). Anhedral pyrite in about 20 µm to 290 µm aggregates within the granitoid matrix (Figure 21F).

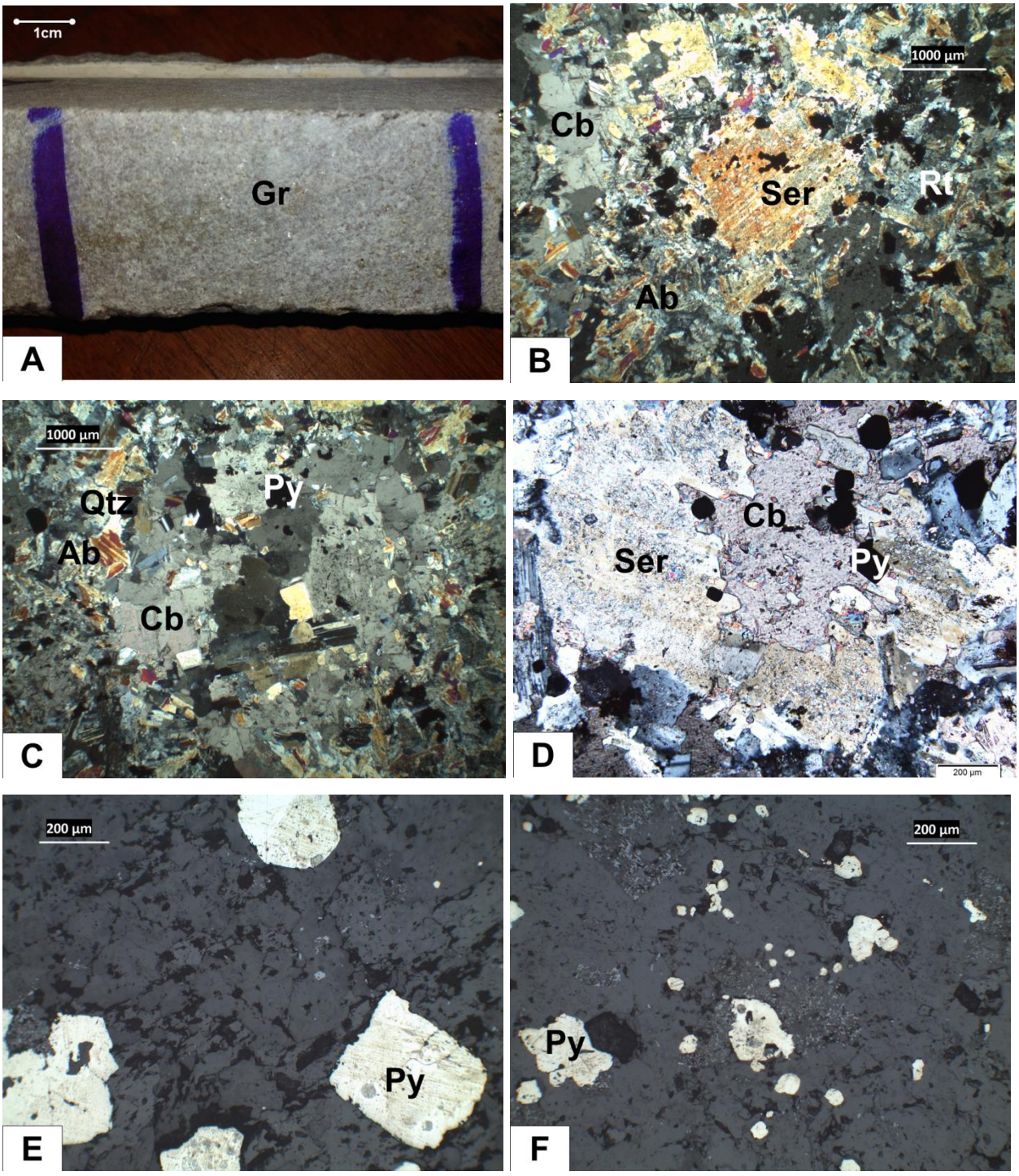

Figure 21. MGR20; granitoid rock sample. A. Porphyry granitoid (Gr) rock sample; B. Albite altered to sericite (Ser), carbonate (Cb), albite (Ab), and rutile in the granitoid matrix under transmitted light; C. Albite (Ab), carbonate (Cb), quartz (Qtz), and pyrite (Py) in the granitoid matrix under transmitted light; D. Alteration of albite to sericite (Ser), carbonate (Cb) and pyrite (Py) in granitoid matrix under transmitted light; E. Euhedral pyrite (Py) within the rock matrix under reflected light; F. Anhedral pyrite (Py) in the matrix under reflected light.

III.1.4. Unmineralized granitoid (UGR) samples

15. UGR10

UGR10 was collected at 261.8 m depth from the TDD036 core from an 8.93 m medium-grained light grey feldspar-rich granitoid (Figure 22A) interlayered with an upper 41.1 m thick and a lower 56.44 m thick black shale with carbonaceous mudstone sequence and intercalated thin layers of siltstone. The sample was taken 3.71 m above the lower black shale unit. The thin section consists of a porphyritic medium-grained granitoid with rare disseminated sulphides.

The granitoid matrix is composed of albite and overgrowing carbonates (Figure 22B&C). Albite is the major component of the rock appearing in the form of subhedral to euhedral crystals. Albite crystal sizes vary from 220-200 µm × 2400-1440 µm. Coarse-grained albite commonly shows an alteration to sericite. Carbonate occurs as anhedral crystals overgrowing the albite-rich matrix. Carbonate crystals measure approximately 100 µm to 640 µm. Fine-grained albite is commonly found as inclusions within carbonates. About 40 µm anhedral rutile is randomly distributed in the matrix, but particularly, near altered albite occurs 80 µm to 400 µm rutile grains size (Figure 22F).

Pyrite consists of anhedral to subhedral crystals of approximately 10 µm to 340 µm that are irregularly distributed in the matrix (Figure 22D). The pyrite may also form small stringers suggesting a precipitation of pyrite in zones of weakness (Figure 22E).

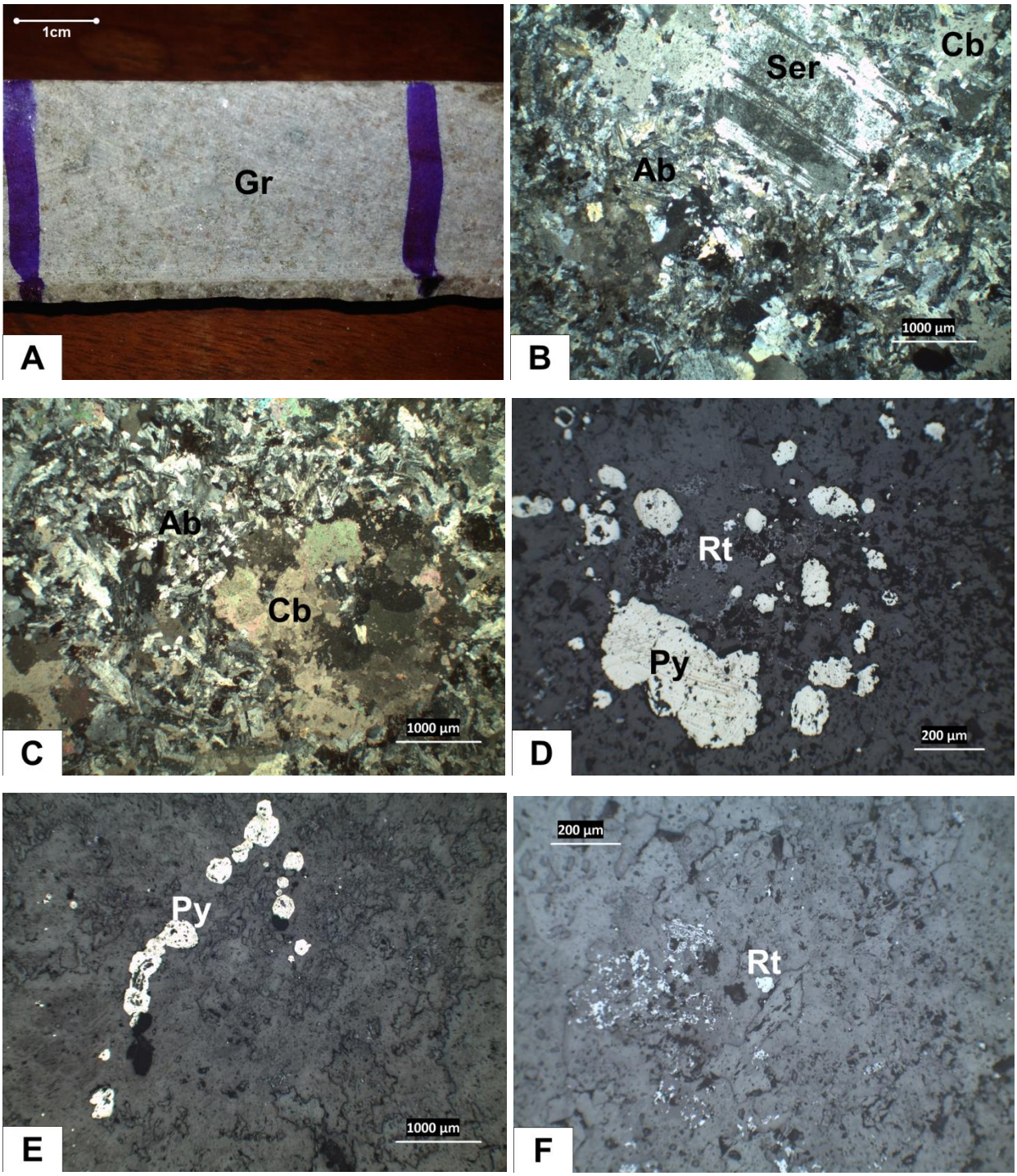

Figure 22. UGR10; granitoid rock sample. A. Granitoid (Gr) rock; B. Euhedral albite (Ab), secondary carbonate (Cb), and the albite showing an alteration to sericite (Ser) in the granitoid matrix under crossed polarized transmitted light; C. Carbonate (Cb) within albite-rich (Ab) matrix in crossed polarized transmitted light; D. Anhedral pyrite (Py) and rutile (Rt) under reflected light; E. anhedral pyrite (Py) aligned in the form of a short and non-continuous stringer in reflected light; F. Rutile (Rt) in the altered albite area.

16. UGR13

UGR13 was collected at 264.1 m depth from the TDD078 core from a 49.02 m thick medium-grained light grey feldspar-rich granitoid intrusion unit (Figure 23A) interlayered with an upper 17.43 m thick and a lower 28.73 m thick black shale with carbonaceous mudstone and intercalated thin layers of siltstone. The sample was taken 4.5 m below the upper black shale unit. The thin section consists of a porphyritic medium-grained granitoid matrix with rarely distributed sulphide.

The granitoid matrix consists of abundant albite with overgrowing carbonate (Figure 23B). Albite consists of subhedral to euhedral crystals ranging in size from 160 × 240 µm to 2800 × 4160 µm. Coarse-grained albite commonly shows an alteration to sericite (Figure 23C). Carbonate consists of anhedral crystals overgrowing albite. Carbonate crystals range in size from ~160 to 3200 µm. Fine-grained albite is commonly found as inclusions in carbonate.

Pyrrhotite consists of 120 µm anhedral patches of crystals that have grown as isolated crystals in the matrix (Figure 23E). Pyrrhotite is commonly intergrown with rutile (Figure 23D). Rutile commonly occurs near altered albite (Figure 23D&F).

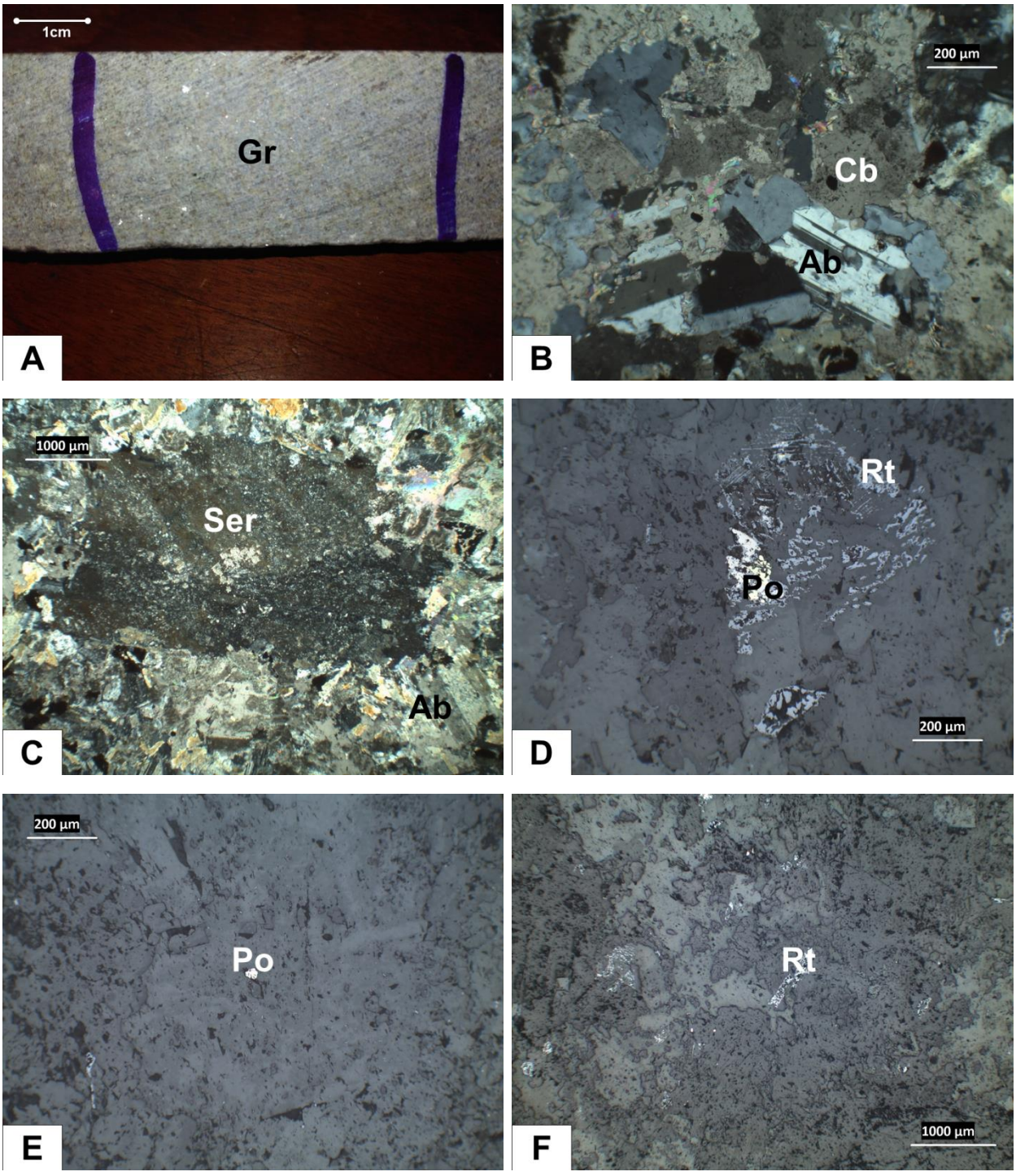

Figure 23. UGR13; granitoid sample. A. Porphyry granitoid (Gr) sample; B. Euhedral albite (Ab) and overgrowing carbonate (Cb) under transmitted light; C. Albite alteration to sericite (Ser) and albite (Ab) in the granitoid matrix under transmitted light; D. Anhedral pyrrhotite (Po) and rutile under reflected light; E. Rare pyrrhotite (Po) in the matrix in reflected light; F. Rutile in the granitoid matrix under reflected light.

17. UGR14

UGR14 was collected at 232.48 m depth of the TDD078 core from an 11.27 m medium-grained light grey feldspar-rich granitoid (Figure 24A) interlayered with an upper 50.24 m thick and a lower 17.83 m thick black shale. The sample was taken 1.98 m below the upper black shale. The thin section consists of a porphyritic medium-grained granitoid matrix with rare disseminated sulphides and clusters of carbonate minerals.

The granitoid matrix is composed of abundant albite with overgrowing carbonate (Figure 24B). Albite consists of subhedral to euhedral crystals commonly showing an alteration to sericite. Albite crystals vary in size from 3200 x 1600 µm to 160 x 120 µm. Carbonate consists of anhedral crystals overgrowing the albite-rich matrix with an average size of 1300 µm. Rare subhedral to anhedral pyrite is irregularly distributed within the matrix (Figure 24E). The pyrite ranges in size from 20 to 460 µm. Fine-grained rutile commonly occurs in contact with pyrite. Rutile is also commonly found near altered albite (Figure 24D).

The carbonate minerals cluster in a probably deformational structure occurring in the form of vein and having an average thickness of 640 µm (Figure 24C).

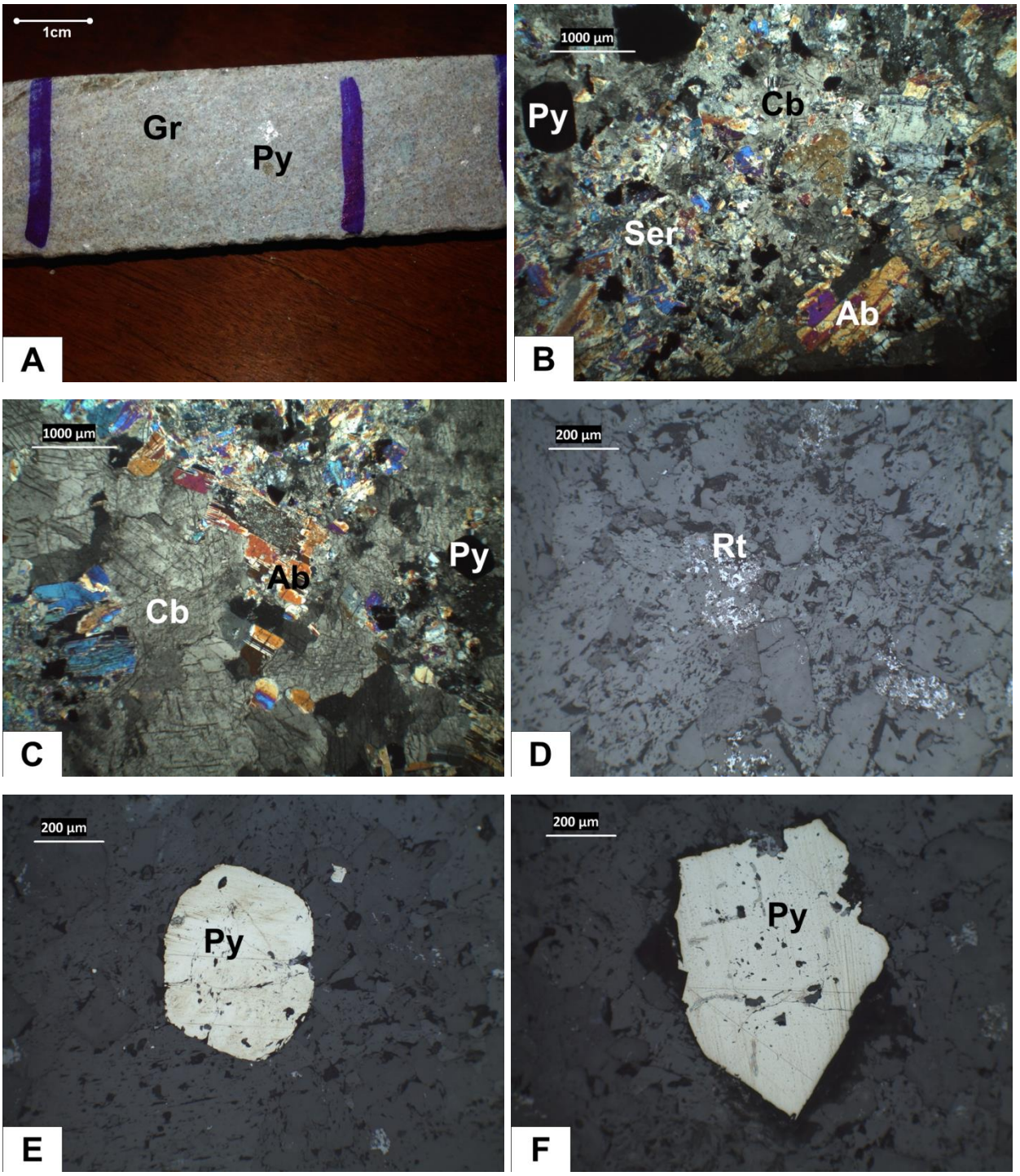

Figure 24. UGR14; granitoid sample. A. Porphyry granitoid (Gr) with disseminated pyrite (Py); B. Euhedral albite (Ab), sericite (Ser) and pyrite (Py) in granitoid matrix under transmitted light; C. Carbonate (Cb) cluster within albite-rich (Ab) matrix in transmitted light; D. Rutile (Rt) within the matrix under reflected light; E. Euhedral to subheudral pyrite (Py) in the matrix in reflected light; F. Subhedral pyrite (Py) occasionnally distibuted in the albite-rich matrix in reflected light.

III.1.5. Hydrothermal vein (HVN) samples

18. HVN2

HVN2 was taken at 115.5 m depth of TDD057 core from an approximately 15 cm quartz vein crosscutting a 25.78 m fine-grained black shale (Figure 25A&B) interlayered with an upper 10.72 m thick and a lower 0.47 m thick feldspar-rich granitoid intrusive sills. The sample was taken 5.3 m below the upper granitoid sill. The thin section consists of a quartz-rich vein associated with albite and carbonate, and crosscutting the black shale host rock. Along the vein, abundant sulphide is disseminated in the host rock forming a sulphide-rich zone.

The host rock consists of dark grey black shale formed of anhedral fine-grained quartz of approximately 50 µm in size, albite of about 80 µm size and organic matter formed of fine non-crystalline carbon. Albite in the host rock matrix is commonly found near sulphide crystals. Rare fine-grained tourmaline, measuring around 20 µm, is randomly distributed in the host rock matrix. Abundant anhedral to subhedral pyrite of about 320 µm in size is randomly disseminated within the contact selvedge of the host rock with the vein (Figure 25D). The disseminated anhedral to subhedral pyrite crystals have fine-grained albite and quartz crystals as inclusions. Rutile of ~200 µm occurs with pyrite crystals, whereas fine-grained rutile of approximately 8 µm to 20 µm is randomly distributed within the host rock matrix (Figure 25F).

The vein consists of abundant anhedral quartz, subhedral albite and anhedral carbonate varying in size from the core to the rims (Figure 25C). Coarse-grained quartz crystals of approximately 3200 µm are found in the core of the vein while fine-grained 400 µm quartz and albite of about 400 x 320 µm to 960 x 1500 µm overgrown by medium-grained carbonate crystals of about 1500 µm occur toward the contact with the host rock. A coarse-grained subhedral pyrite measuring about 2000 µm occurs in the core of vein. Rare fine-grained pyrite of approximately 300 µm is irregularly distributed toward the contact of the vein with the host rock (Figure 25E).

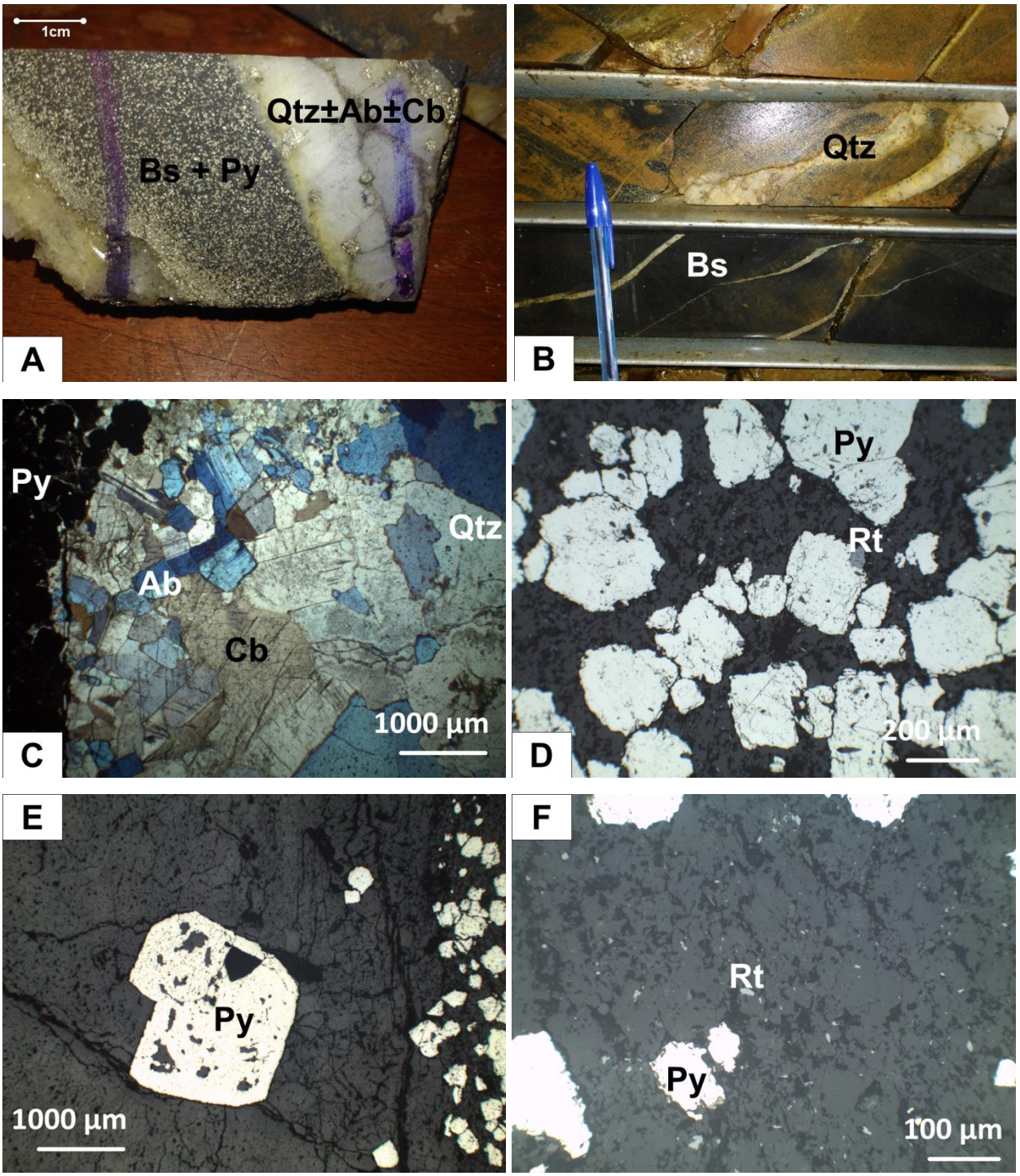

Figure 25. HVN2; hydrothermal quartz vein crosscutting the black shale. A. Quartz- (Qtz) carbonate- (Cb) rich vein sample in black shale (Bs) with disseminated pyrite (Py) along the contact zone with the host rock; B. Core section of the quartz- (Qtz) carbonate-rich vein crosscutting the black shale (Bs); C. Polished section in transmitted light showing disseminated pyrite (Py) in black shale matrix and abundant albite (Ab) and carbonate (Cb) on the contact with the quartz-rich (Qtz) vein; D. Anhedral to subhedral disseminated pyrite (Py) and rutile (Rt) in black shale matrix under reflected light; E. Subhedral pyrite (Py) in the quartz vein under reflected light; F. Disseminated pyrite (Py) and rutile (Rt) in the black shale matrix.

19. HVN5

HVN5 was taken at 86.5 m depth of the TDD049 core from an approximately 3 cm thick quartz vein crosscutting a 62.65 m fine-grained black shale unit (Figure 26A) interlayered with an upper 1.34 m and a lower 0.75 m thick feldspar-rich granitoid intrusive sill. The sample was collected 4.52 m above the lower granitoid sill. The thin section consists of a quartz-rich vein crosscutting the black shale host rock with abundant disseminated pyrite in the alteration selvedge in the host rock along the vein contact. Quartz-rich veinlets are randomly oriented in the host rock and crosscut the main vein at high and low angles.

The host rock consists of abundant fine-grained quartz, moderate albite and extremely fine-grained dark non-crystalline carbon (Figure 26C). Quartz and albite consist of anhedral crystals measuring 80 µm and 40 µm respectively.

The veinlet that crosscuts the main vein is composed of anhedral quartz and albite crystals varying in size from 40 µm to 800 µm (Figure 26C). A sulphide-rich zone occurs in the host rock matrix along the vein selvedge. The sulphide-rich zone consists of an aggregate of pyrite within a matrix composed of about 240 µm albite, 250 µm quartz, and 320 µm carbonate crystals (Figure 26E&F). Arsenopyrite of about 60 µm is intergrown with pyrite. Rutile of about 100 µm in size is either randomly disseminated in the matrix or occurs in contact with pyrite (Figure 26F).

The vein consists of abundant quartz showing comb texture (Figure 26B). Crystals are elongated perpendicularly to the vein's direction and commonly measure about 2000 x 560 µm. Towards the contact of the vein with the host rock fine-grained crystals of quartz occur measuring approximately 160 µm. Up to 3600 µm sized anhedral to euhedral pyrite is either locally distributed in the vein or forms aggregates. Abundant albite of 1360 x 560 µm size is commonly found within the vein where aggregates of pyrite are present (Figure 26D). Fine-grained albite is found as inclusions within the vein pyrite.

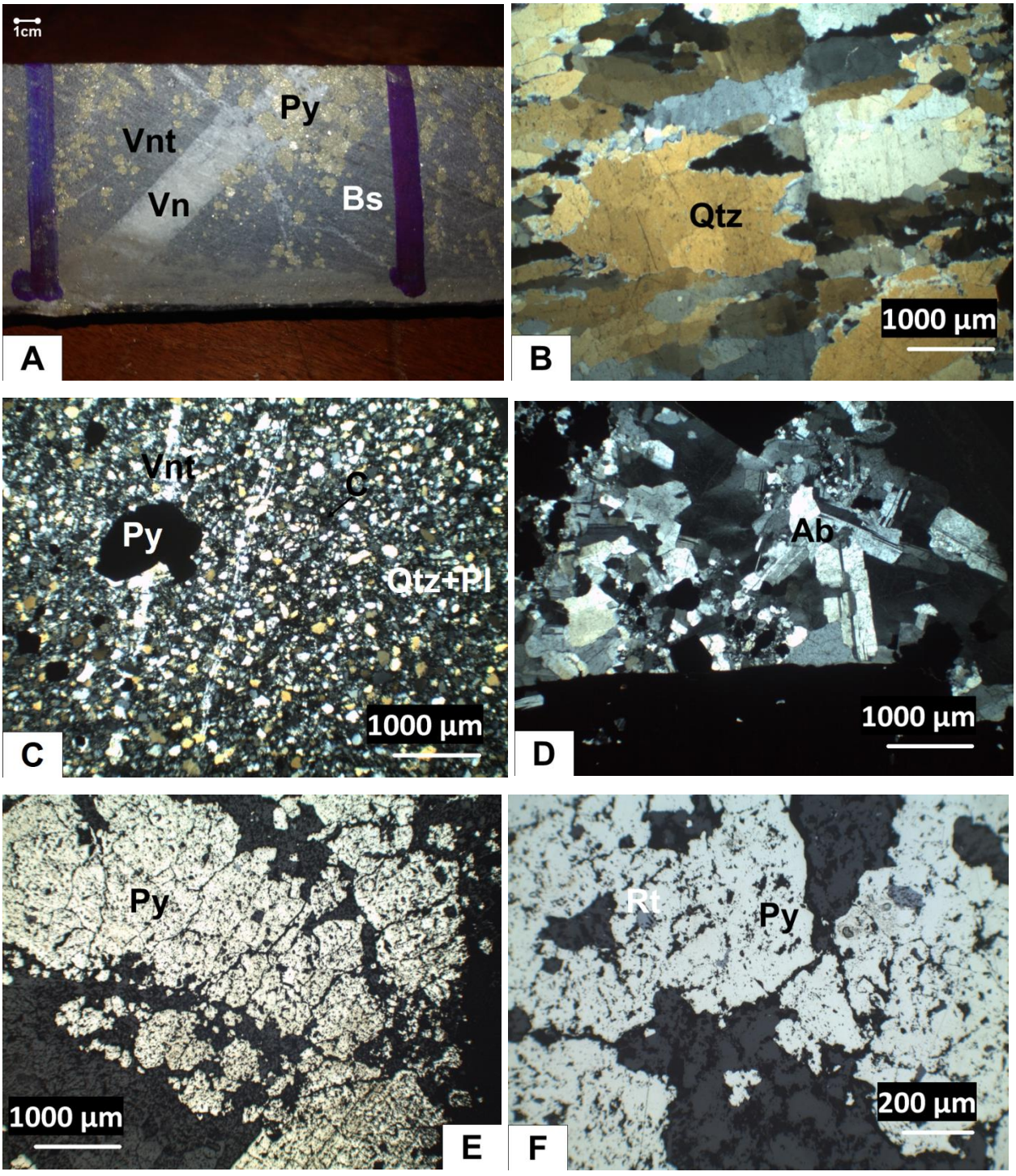

Figure 26. HVN5; hydrothermal vein. A. Quartz vein (Vn) and veinlets (Vnt) crosscutting the black shale (Bs) with abundant disseminated pyrite (Py); B. quartz (Qtz) vein under transmitted light; C. Quartz (Qtz) and albite (Ab) of host rock matrix with crosscutting veinlets (Vnt) and pyrite (Py) in transmitted light; D. Albite (Ab) in the contact between the main quartz vein and veinlets under transmitted light; E. Anhedral disseminated pyrite (Py) under reflected light; F. Anhedral pyrite (Py) and rutile (Rt) as an inclusion in reflected light.

20. HVN7

Hydrothermal vein HVN7 was taken at 171.5 m depth of TDD040 core from an approximately 20 cm quartz vein crosscutting a 219.57 m thick fine-grained black shale unit (Figure 27A). In this section there are an upper 5.9 m and a lower 28 m thick feldspar-rich granitoid intrusive sill. The sample was collected 85.47 m above the lower granitoid intrusive sill. The thin section consists of a zoned quartz-, muscovite-, and carbonate-rich vein crosscutting the black shale host rock.

The black shale host rock consists of a fine-grained matrix composed of anhedral quartz and albite-rich crystals of 80 µm and 60 µm respectively as well as organic matter consisting of dark fine non-crystalline carbon. Rare fine-grained pyrite is randomly distributed in the host rock matrix. Rutile is irregularly distributed within the matrix and measures approximately 20µm (Figure 27B).

The vein consists of different zones from the contact with the host rock to the core:

- Near the contact with the host rock lies a fine-grained 1200 µm thick zone composed of approximately 60 µm quartz, 60 µm albite, 70 µm carbonate and 200 µm muscovite (Figure 27C);
- Then follows a medium-grained ~1900 µm thick zone of abundant anhedral ~560 µm carbonate associated with minor ~480 µm albite and ~500 µm muscovite;
- Further inwards follows a fine-grained zone of abundant organic matter with fine-grained quartz, albite, carbonate and muscovite. Muscovite is often found along the edge of sulphide crystals;
- A coarse-grained zone composed of about 3000 µm carbonate with minor 240 x 400 µm albite and muscovite of 880 x 200 µm size (Figure 27D).
- A medium-grained 5600 µm thick pyrite-rich zone follows the carbonate-rich layer. The pyrite consists commonly of subhedral to euhedral crystals varying in size from 160 µm to 800 µm (Figure 27F).

In addition, pyrite, locally distributed within the vein, is commonly subhedral to euhedral in shape and measures about 400 µm to 1200 µm in size (Figure 27E).

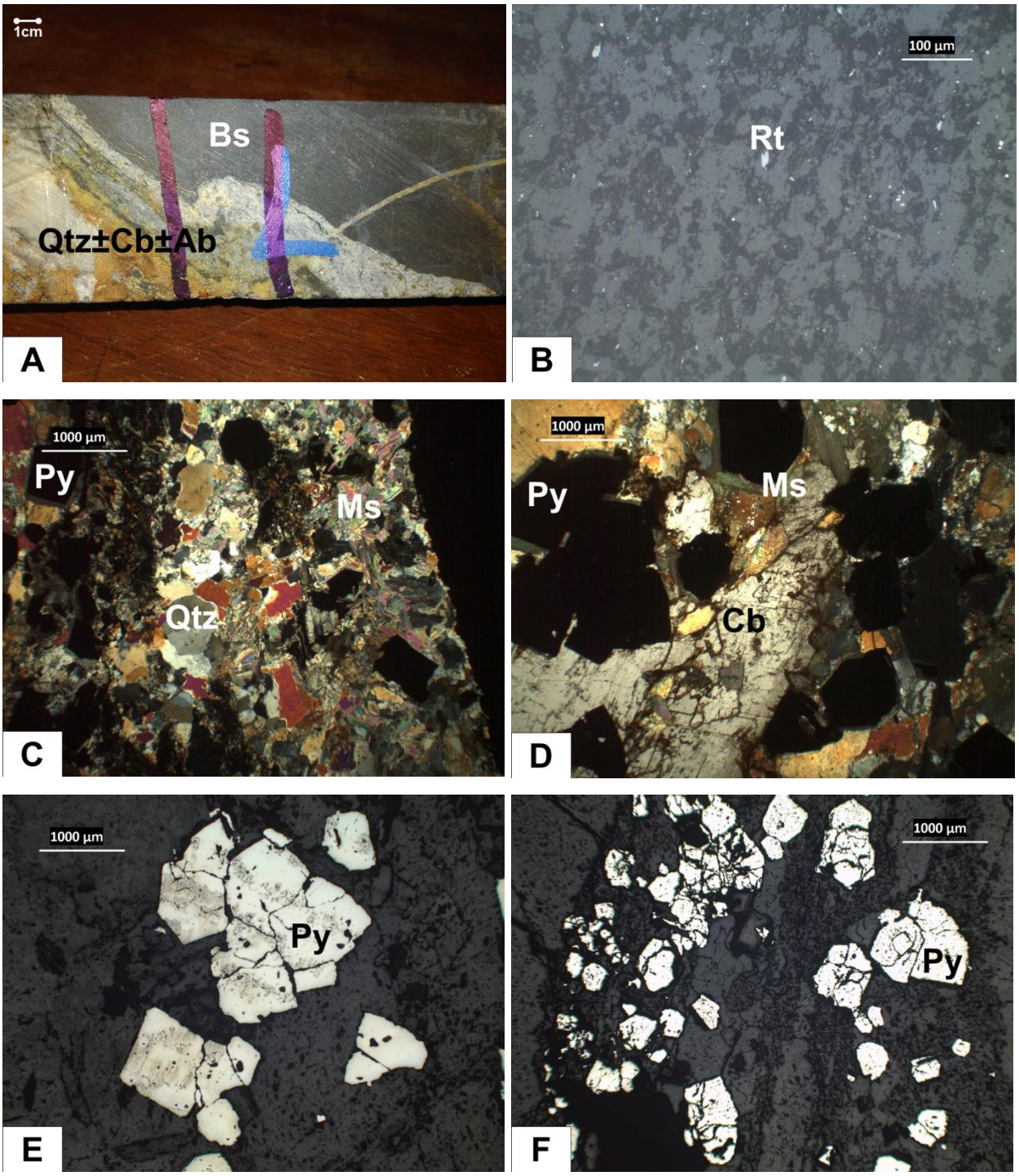

Figure 27. HVN7; hydrothermal vein sample crosscutting the black shale. A. Quartz (Qtz) vein with albite (Ab) and carbonate (Cb) crosscutting the black shale (Bs); B. Rutile (Rt) scattered in the host rock matrix under reflected light; C. Quartz (Qtz) vein with muscovite-rich (Ms) and pyrite-rich (Py) zone in transmitted light; D. Carbonate-rich zone with pyrite (Py) and muscovite (Ms) within quartz vein under transmitted light; E. Subhedral to euhedral pyrite (Py) in the vein under reflected light; F. Aggregate of subhedral to anhedral pyrite (Py) within the quartz vein.

21. HVN8

Sample HVN8 was taken at 106.5 m depth of TDD036 core from a 1 m quartz vein associated with abundant massive sulphide and crosscutting a 109.18 m thick fine-grained black shale unit (Figure 28A) interlayered with an upper 16.57 m and a lower 14.1 m thick feldspar-rich granitoid intrusive sills. The sample was collected 33.85 m below the upper granitoid sill. Quartz-rich veinlets crosscut the black shale and the main vein at a high angle.

The black shale matrix is composed of fine-grained anhedral crystals of about 160 µm quartz, 180 µm albite, and extremely fine-grained dark non-crystalline carbon (Figure 28C). Albite in the matrix shows a sericitic alteration. Albite commonly occurs near sulphide crystals. Quartz occurs as elongated crystals randomly oriented in the sulphide-rich zone and has approximately 400 by 100 µm of size (Figure 28B). Anhedral to euhedral pyrite and arsenopyrite, varying in size from 80 µm to 2000 µm, are randomly distributed within the matrix, and in the massive sulphide vein selvedge are often not disintegrated, whereas they appear disintegrated away from the vein selvedge. Albite is often found as inclusions in pyrite.

Veinlets are about 960 µm thick and consist of abundant quartz and minor albite. Veinlets commonly converge into one thicker veinlet within the black shale matrix (Figure 28C). Veinlet crystal sizes vary from the vein core to the rim with coarse-grained quartz of about 720 µm in the core and fine-grained quartz of about 80 µm at the rim.

The vein consists of massive sulphide in the quartz-rich matrix associated with minor albite. The massive sulphide consists of massive arsenopyrite associated with massive pyrite (Figure 28E). The quartz crystals of the vein are coarse-grained with grain sizes of approximately 4800 µm. Albite consists of medium-grained crystals of about 800 µm commonly found around massive arsenopyrite and pyrite (Figure 28D). Albite is also found as inclusions in pyrite with an average size of 160 µm. The massive pyrite commonly occurs on the contact of the vein with the host rock and along fractures in the massive arsenopyrite (Figure 28E). Rare fine-grained chalcopyrite occurs as inclusions in pyrite. An approximate 10 µm sized particle of native **gold** occurs at the interface zone between pyrite crystals. The gold grain is associated with pyrite and overgrows the interface materials between pyrite crystals (Figure 28F).

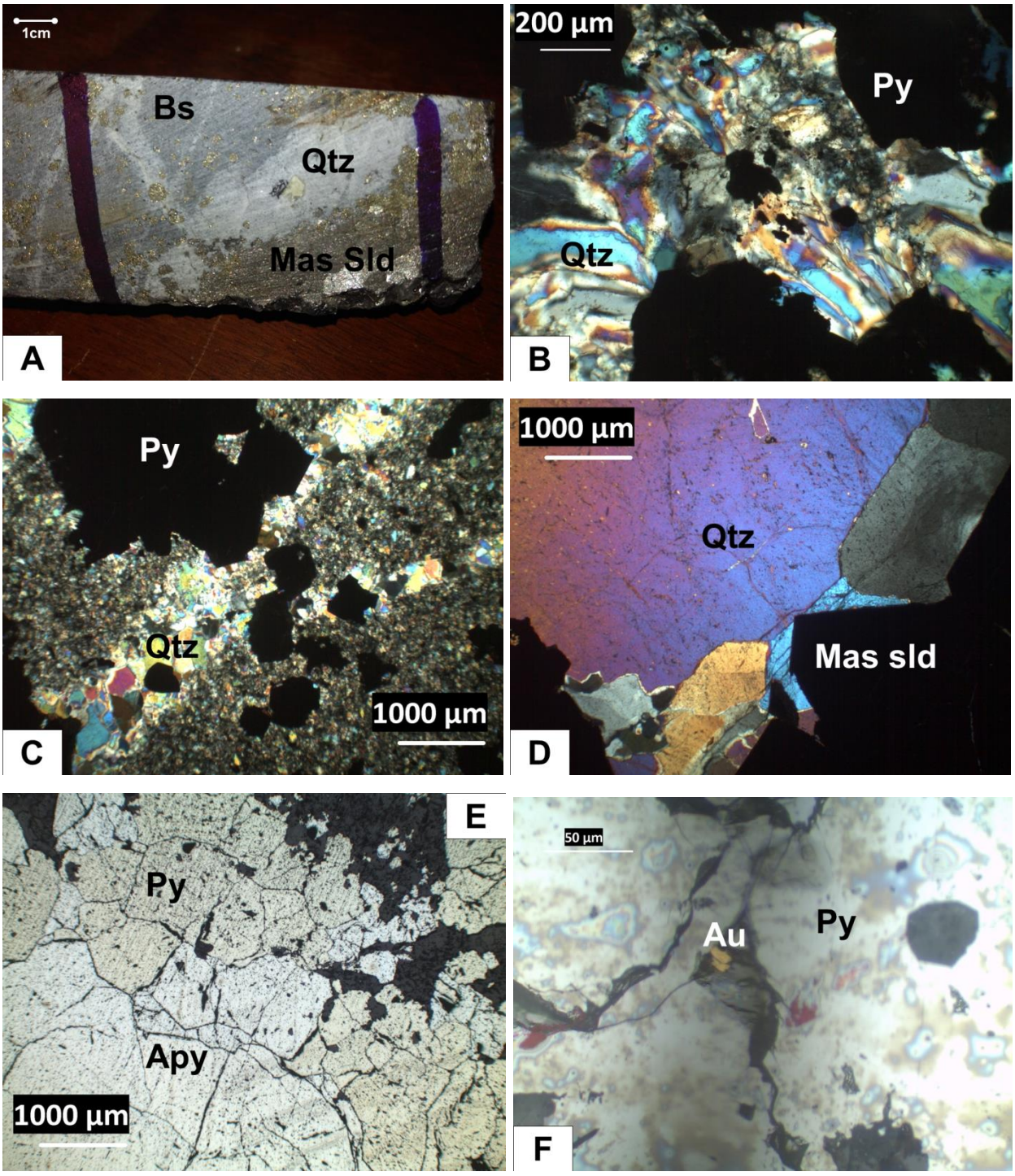

Figure 28. HVN8; hydrothermal vein. A. Quartz (Qtz) vein crosscutting the black shale (Bs) and associated massive sulphide (Sld); B. Quartz (Qtz) around pyrite (Py) under transmitted light; C. Intersecting quartz (Qtz) veinlets and pyrite (Py) in transmitted light; D. Quartz (Qtz) vein in contact with the massive sulphide (Sld) body under transmitted light; E. Pyrite (Py) and arsenopyrite (Apy) of the massive sulphide body in contact with the host rock under reflected light; F. Gold (Au) grain occuring in pyrite (Py) crystals interface.

22. HVN16

Hydrothermal vein HVN16 was taken at 103.2 m depth of TDD054 core from a 1.10 m thick quartz-rich vein crosscutting a 147.89 m fine-grained black shale unit (Figure 29A) underlain by a 9 m thick feldspar-rich granitoid intrusive sill. The sample was collected 44.69 m above the granitoid sill. The thin section consists of a quartz-rich vein containing black shale host rock fragments. Abundant disseminated and massive sulphide is randomly distributed in and around the vein, especially within the black shale matrix. Also, quartz-rich veinlets are randomly oriented in the black shale matrix.

The black shale consists of a fine-grained matrix composed of anhedral crystals of quartz and albite, and organic matter. Quartz crystals are approximately 100 µm in size while albite crystals measure about 160 µm. The organic matter consists of fine-grained non-crystalline carbon abundantly distributed in the matrix. Abundant subhedral to anhedral pyrite is randomly disseminated in the black shale matrix (Figure 29D&F). The subhedral to anhedral disseminated pyrite varies in size from 10 µm to 400 µm. Fine-grained quartz and albite are often found as inclusions within pyrite. Rare 50 µm rutile is randomly distributed in the matrix, but also occurs in contact with pyrite.

The veinlets vary in thickness from 30 µm to 880 µm with coarse-grained quartz and minor albite crystals occurring in the core and fine-grained crystals at the rim. The veinlets are commonly composed of about 140 µm quartz and 170 µm albite crystals. Thin veinlets crosscut the thicker veinlet at high angle (Figure 29B).

The quartz vein consists of coarse-grained anhedral quartz measuring approximately 800 µm to 4000 µm. The vein is fractured and along the fracture occurs fine-grained quartz and albite of about 240 µm in size, associated with abundant pyrite and organic matter (Figure 29C). The pyrite within the vein consists of euhedral shaped crystals (Figure 29E). On the contact between the vein and the black shale occur fine-grained crystals of quartz, albite and carbonate of approximately 80 µm, and pyrite of about 100 µm in size.

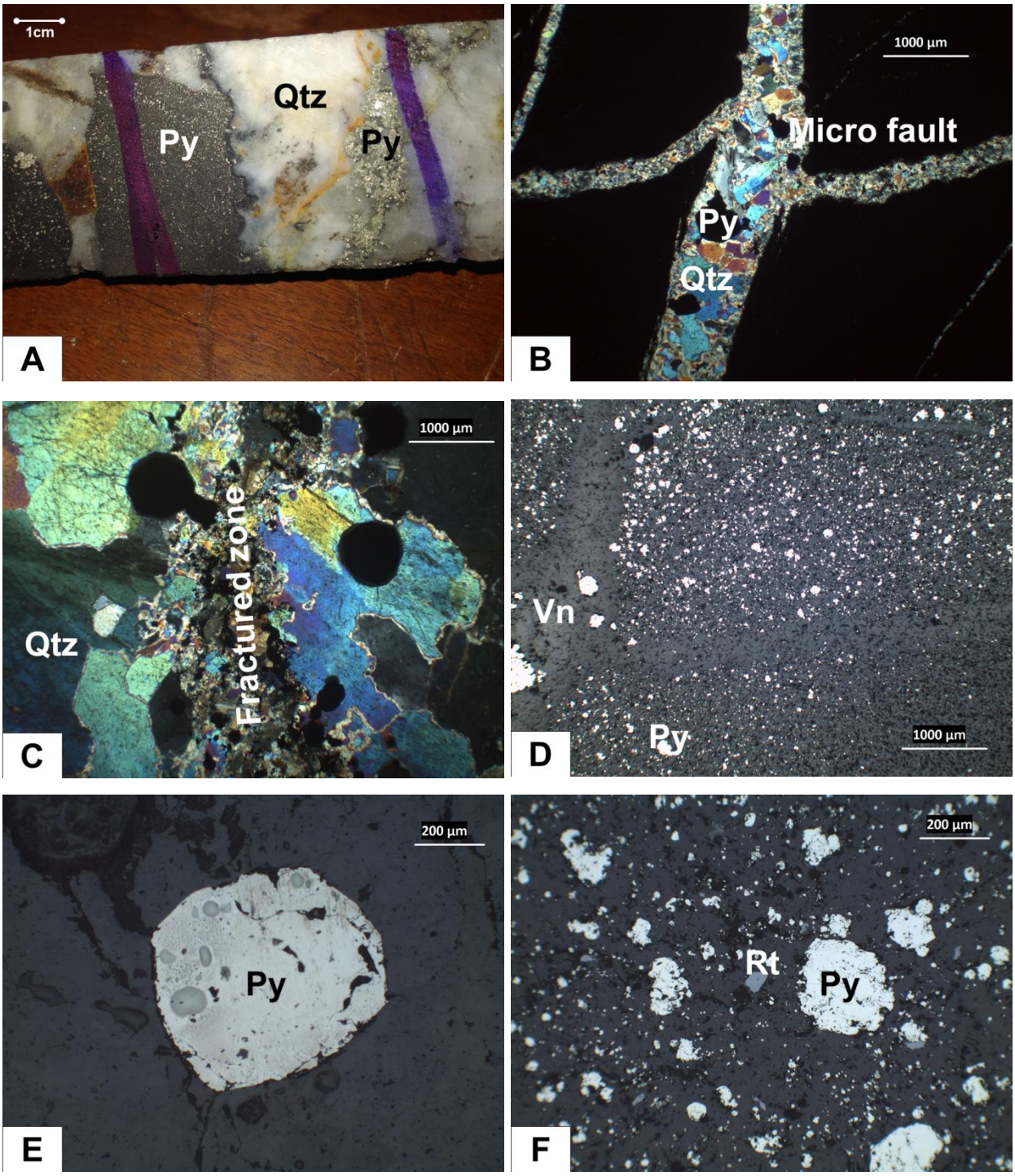

Figure 29. HVN16; hydrothermal vein sample in black shale. A. Quartz (Qtz) vein crosscutting the black shale with disseminated pyrite (Py); B. Quartz-rich veinlets and disseminated pyrite (Py) under transmitted light; C. Fractured zone within the quartz (Qtz) vein in transmitted light; D. Disseminated anhedral pyrite (Py) along the vein (Vn) selvedge in the black shale host rock under reflected light; E. Subhedral pyrite (Py) within the quartz vein under reflected light; F. Dissiminated anhedral pyrite (Py) and rutile (Rt) in the vein selvedge in black shale under reflected light.

23. HVN19

Sample HVN19 was collected at 132.8 m depth of TDD079 core from a 25 cm quartz-rich vein associated with massive sulphide, crosscutting an 84.77 m medium-grained light grey feldspar-rich granitoid unit (Figure 30A) interlayered with an upper 48.23 m and a lower 41.92 m thick black shale host rock. The sample was taken 0.20 m above the lower black shale unit. The thin section consists of a quartz vein associated with massive sulphide crosscutting a porphyritic medium-grained granitoid host rock matrix.

The host rock granitoid matrix consists of abundant euhedral albite, overgrowing anhedral carbonate and minor quartz. Albite in the host rock ranges in size from 320 to 1040 µm. Quartz consists commonly of fine-grained crystals measuring about 350 µm and rarely interstitial between the albite crystals. Carbonate overgrows the albite-rich matrix and measures about 80 µm to 960 µm in size (Figure 30C). Euhedral pyrite occurs in the granitoid matrix near the contact with the massive sulphide vein (Figure 30E), and euhedral fractured pyrite is occasionally disseminated in the host rock matrix measuring approximately 180 µm to 720 µm.

The vein consists of coarse-grained massive pyrite and arsenopyrite in a coarse-grained quartz matrix. The coarse-grained quartz matrix measures up to 1 cm of crystal size (Figure 30B). On the contact between the coarse-grained quartz with the massive pyrite and arsenopyrite occurs albite of about 640 x 1200 µm. Fine-grained albite and quartz are found as inclusions within the massive pyrite and arsenopyrite. The massive pyrite and arsenopyrite consist of coarse-grained crystals intergrown in the quartz-rich matrix (Figure 30D&F).

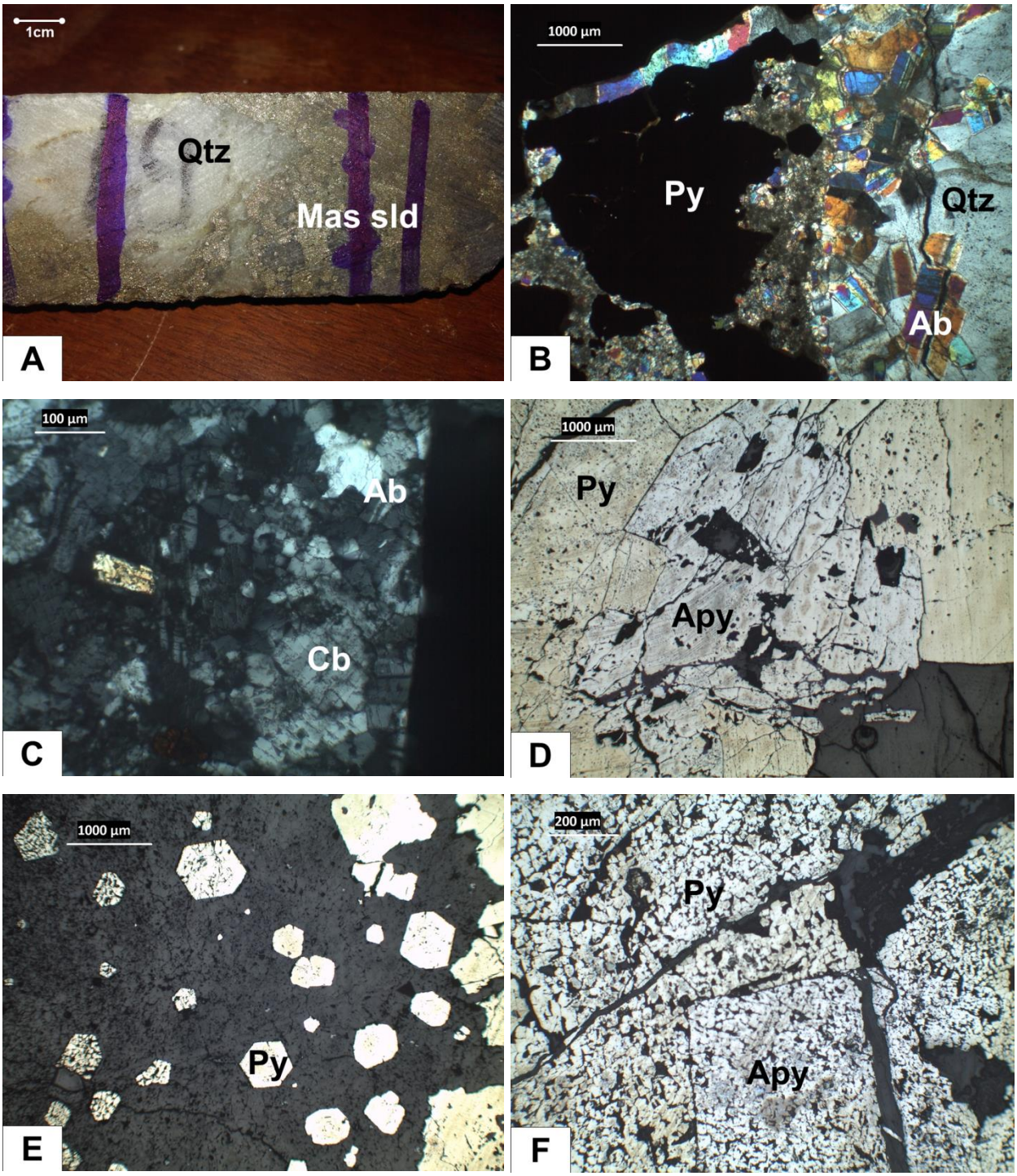

Figure 30. HVN19; hydrothermal vein sample in granitoid intrusive sill. A. Quartz (Qtz) vein crosscutting the granitoid sill and associated disseminated and massive sulphide (Sld); B. Pyrite (Py) and quartz (Qtz) vein with albite (Ab) developed around the contact of the vein with the pyrite under transmitted light; C. Carbonate (Cb) and albite (Ab) in the granitoid host rock under transmitted light; D. Massive pyrite (Py) and arsenopyrite (Apy) of the vein under reflected light; E. Euhedral pyrite (Py) in the granitoid matrix under reflected light; F. Fractured massive pyrite (Py) and arsenopyrite (Apy) under reflected light.

III.2. MICRO-CHEMICAL ANALYSIS OF THE TWANGIZA DEPOSIT SULPHIDES

III.2.1. Mineralized black shale samples

The different types of sulphide identified in the mineralized black shale consist of pyrite, arsenopyrite and chalcopyrite (Figure 31). The different pyrite textures investigated in the present sample type consist commonly of: (i) disseminated fine-grained crystals in the quartz and albite-rich matrix associated with fine-grained monazite, zircon, fluor-apatite, muscovite, and rutile; (ii) euhedral disintegrated crystals disseminated in the matrix (Figure 36D); (iii) anhedral crystals locally disseminated in the matrix; (iv) aggregates of anhedral annealed crystals within a phlogopite-rich matrix associated with quartz and albite in the sulphide-rich segregated lenses in the pelitic matrix; and (v) euhedral and anhedral crystals of pyrite within the quartz veins associated with minor magnesite and siderite.

Pyrites with different textures in the mineralised black shales have uniform major elemental compositions (Table 3). The percentage of Fe ranges from 44.57 to 45.52 wt. % while S ranges from 54.11 to 55.15 wt. %. However, minor concentrations of As are found within the fine-grained pyrite scattered in the matrix, as shown by the weak As peak of the pyrite spectrum (Figure 31B). Here As is estimated at about 0.92 wt. % (Table 3).

The arsenopyrite, commonly found as inclusions in the pyrite or occasionally intergrown with the pyrite, contains low concentrations of Ni element (Figure 31D; Table 3). The Ni content of the arsenopyrite is estimated at 0.39 wt. % and shows small peaks on the arsenopyrite spectrum. Chalcopyrite is almost exclusively found as inclusions within the pyrite (Figure 31C; Table 3).

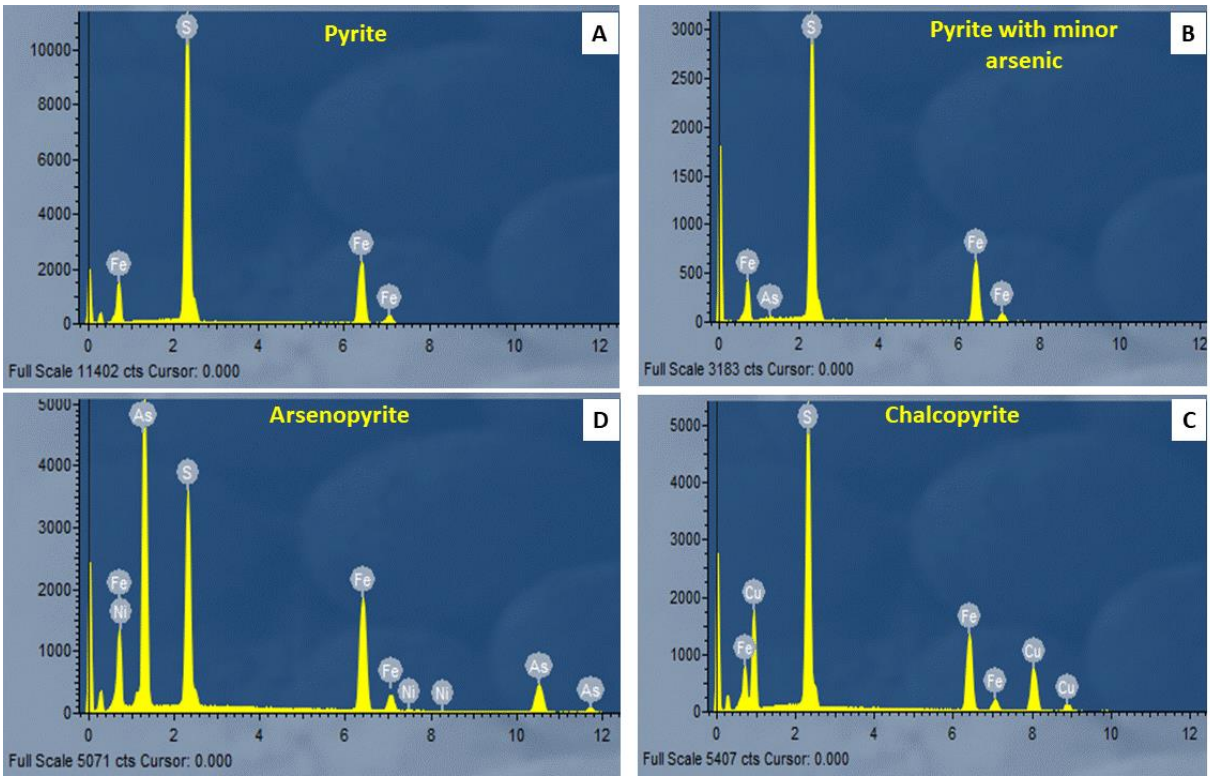

Figure 31. EDS spectra of mineralized black shale sulphides. A. Spectrum of pyrite, B. Spectrum of pyrite with minor amounts of As, C. Spectrum of chalcopyrite, D. Spectrum of arsenopyrite

The gold grains have been identified in the sulphide-rich lenses associated with the pyrite. The analysis of gold shows some small peaks of iron associated with it (Figure 32, Figure 36C).

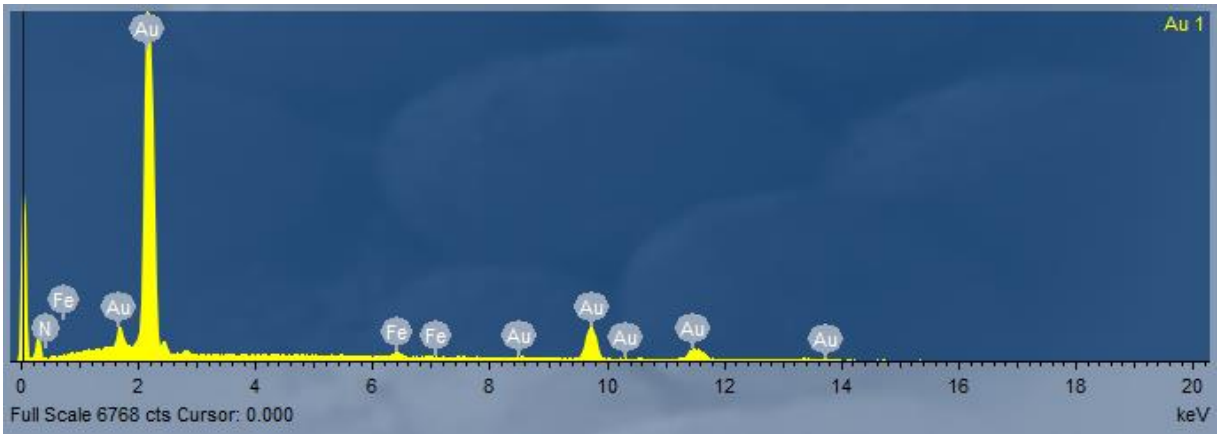

Figure 32. EDS spectrum of gold (Au) associated with pyrite in the mineralized black shale (Au=96.89%; Fe=1.46%).

Table 3. Chemical composition of sulphides associated with the mineralized black shales

	Matrix		Euhedral pyrite		Anhedral pyrite		Sulphide lens			Vein		
	MBS1	MBS3A	MBS1	MBS1	MBS1	MBS1	MBS3B	MBS3B	MBS3A	MBS3B	MBS3B	MBS3B
Wt. % (atom)	Pyrite	Pyrite	Pyrite	Arseno pyrite	Pyrite	Arseno pyrite	Pyrite	Chalcop yrite	Arseno pyrite	Anhedral Pyrite	Arseno pyrite	Euhedral Pyrite
Fe	44.81	44.65	44.99	34.51	45.1	34.44	45.52	30.18	34.45	45.21	34.64	44.57
S	55.00	54.43	54.66	21.13	54.69	21.68	54.11	35.63	22.1	54.69	22.17	55.15
As	0.19	0.92	0.35	43.97	0.21	43.49	0.37	0.00	43.45	0.09	43.18	0.28
Ni	0.00	0.00	0.00	0.39	0.00	0.39	0.00	0.00	0.00	0.00	0.00	0.00
Cu	0.00	0.00	0.00	0.00	0.00	0.00	0.00	34.20	0.00	0.00	0.00	0.00
Total	100.00	100.00	100.00	100.00	100.00	100.00	100.00	100.00	100.00	100.00	100.00	100.00
Ions (norm. 3)												
Fe	0.96	0.96	0.96	0.99	0.96	0.98	0.98	0.99	0.98	0.96	0.99	0.95
S	2.04	2.03	2.03	0.94	2.03	1.08	2.02	2.03	1.10	2.03	1.10	2.05
As	0.00	0.01	0.01	1.06	0.00	0.93	0.01	0.00	0.92	0.00	0.92	0.00
Ni	0.00	0.00	0.00	0.01	0.00	0.01	0.00	0.00	0.00	0.00	0.00	0.00
Cu	0.00	0.00	0.00	0.00	0.00	0.00	0.00	0.98	0.00	0.00	0.00	0.00
Total	3	3	3	3	3	3	3	4	3	3	3	3

The major matrix minerals are quartz associated with plagioclase (Figure 33). The plagioclase is referred to as albite. Quartz and albite are also commonly found as inclusions within the pyrite. The albite is composed of Na, Al and Si, and the composition is uniform everywhere in the sample (Figure 33A; Table 4). No Ca content has been reported. Albite is often found in the vicinity of pyrite phases. The phlogopite is the major phase of the sulphide-rich lens matrix (Figure 33C; Figure 36A; Table 4).

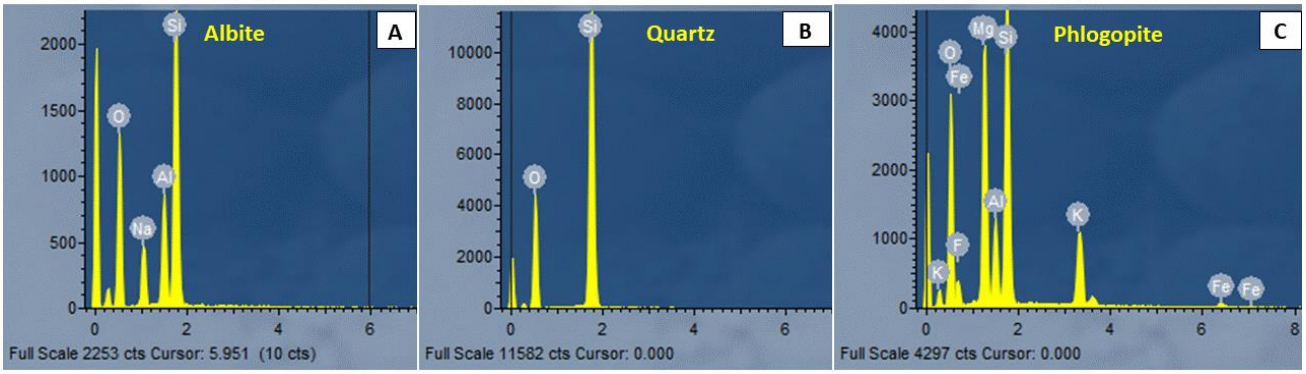

Figure 33. EDS spectra of major matrix minerals of the mineralized black shale. A. Spectrum of Albite; B. Spectrum of quartz; C. Spectrum of phlogopite.

The minor phases of the matrix, consisting of scattered fine-grained crystals, are rutile, apatite with minor fluorine, monazite, zircon, and muscovite (Figure 34; Table 4). Siderite, muscovite, rutile and tourmaline are also found as inclusions within pyrite. The monazite spectrum does not show Th and U peaks, but does, however, contains Nd (Figure 34). Rutile contains low concentrations of vanadium, chromium and tantalum (Figure 34; Table 4). The siderite which occurs as inclusions within pyrite is in solid solution with magnesite and has higher Mg and low Fe content compared to the siderite occurring in the vein (Table 4).

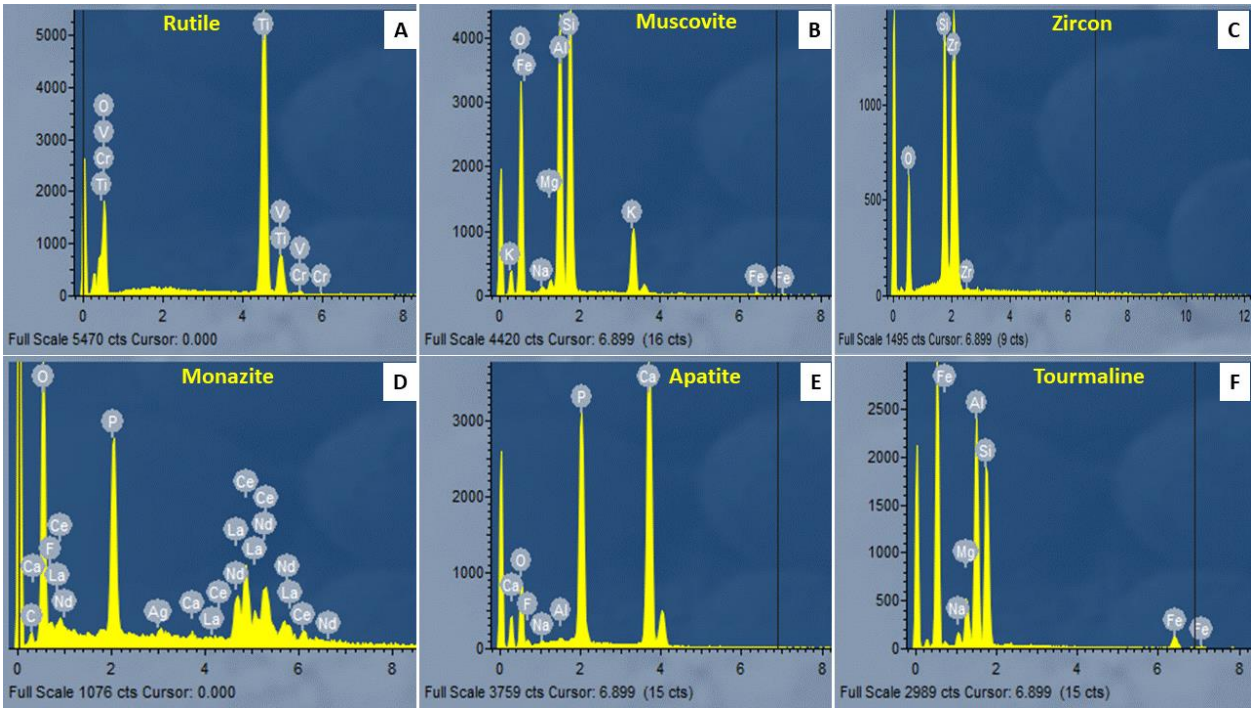

Figure 34. EDS spectra of fine-grained crystals scattered in the mineralized black shale's matrix and as inclusions in pyrite. A. Spectrum of rutile; B. Spectrum of muscovite; C. Spectrum of zircon; D. Spectrum of monazite; E. Spectrum of apatite with minor fluorine; F. Spectrum of tourmaline (B not detected by this method).

The magnesite and siderite are found associated with the quartz vein which crosscut the mineralized black shale (Figure 35; Figure 36B).

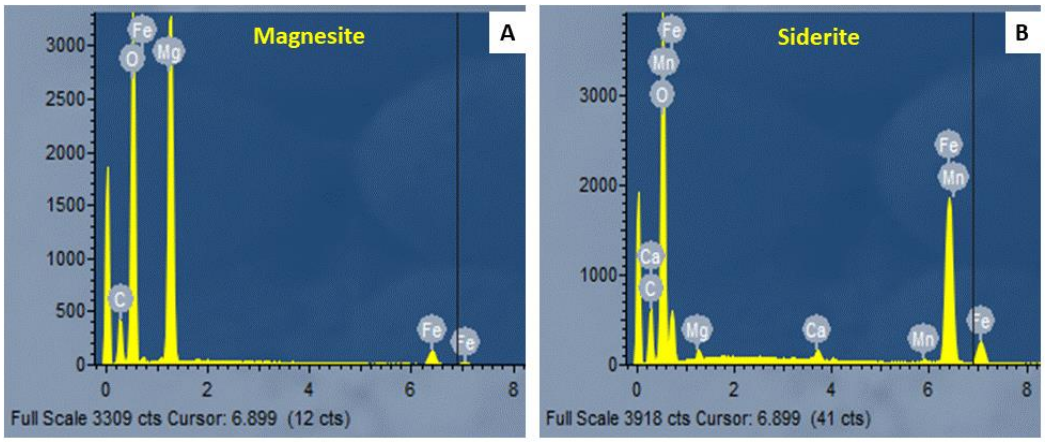

Figure 35. EDS spectra of minerals associated with the quartz veins that crosscut the mineralized black shale. A. Spectrum of magnesite; B. Spectrum of siderite.

Table 4. Chemical composition of oxides, silicates, phosphates and carbonate phases associated with mineralized black shales.

	MBS1	MBS1	MBS3A	MBS1	MBS3B	MBS3A	MBS3A	MBS1	MBS3A	MBS1	MBS3B	MBS3B
	Quartz	Muscovite	Albite	Rutile	apatite	Zircon (lens)	Zircon (matrix)	Phlogopite	Tourmaline (inclusion)	Siderite (inclusion)	Siderite	Magnesite
(Wt. %)												
SiO2	103.44	48.96	68.20	0.00	0.00	31.49	33.24	45.34	38.64	0.00	0.00	0.00
Al2O3	0.00	32.18	18.66	0.11	0.00	0.12	0.63	11.44	33.37	0.00	0.00	0.00
Fe2O3	0.00	0.00	0.00	0.00	0.00	0.00	0.83	0.00	0.00	0.00	0.00	0.00
Cr2O3	0.00	0.00	0.00	0.89	0.00	0.00	0.00	0.00	0.00	0.00	0.00	0.00
TiO2	0.00	0.25	0.07	95.40	0.00	0.18	0.34	0.05	0.08	0.00	0.00	0.00
FeO	0.00	0.97	0.25	0.29	0.00	0.00	0.00	1.46	5.53	29.43	54.62	5.12
MgO	0.00	3.58	0.05	0.24	0.12	0.03	0.21	28.42	6.21	26.24	1.76	42.37
MnO	0.00	0.02	0.12	0.18	0.00	0.00	0.00	0.05	0.06	1.22	0.67	0.22
CaO	0.00	0.01	0.15	0.05	51.63	0.12	0.94	0.16	0.11	0.27	1.14	0.08
Na2O	0.00	0.63	11.60	0.00	0.46	0.00	0.00	0.23	1.93	0.00	0.00	0.00
K2O	0.00	10.04	0.14	0.00	0.01	0.00	0.00	9.63	0.08	0.09	0.00	0.00
BaO	0.00	0.00	0.00	0.00	0.00	0.00	0.00	0.00	0.00	0.05	0.00	0.00
F	0.00	0.00	0.00	0.00	3.31	0.00	0.00	0.00	0.00	0.00	0.00	0.00
Nb2O3	0.00	0.00	0.00	0.52	0.00	0.00	0.00	0.00	0.00	0.00	0.00	0.00
Ta2O5	0.00	0.00	0.00	0.41	0.00	0.00	0.00	0.00	0.00	0.00	0.00	0.00
ZrO2	0.00	0.00	0.00	0.00	0.00	67.45	63.43	0.00	0.00	0.00	0.00	0.00
HfO2	0.00	0.00	0.00	0.00	0.00	2.29	0.00	0.00	0.00	0.00	0.00	0.00
IrO2	0.00	0.00	0.00	0.00	0.00	0.00	0.00	0.00	0.00	0.00	0.00	0.00
ThO2	0.00	0.00	0.00	0.00	0.00	0.00	0.50	0.00	0.00	0.00	0.00	0.00
P2O5	0.00	0.00	0.00	0.00	44.17	0.00	0.00	0.00	0.00	0.00	0.00	0.00
V2O5	0.00	0.00	0.00	1.93	0.00	0.00	0.00	0.00	0.00	0.00	0.00	0.00
Total	103.44	96.64	99.24	100.00	99.7	101.68	100.11	96.78	86.01	57.30	58.19	47.79

.

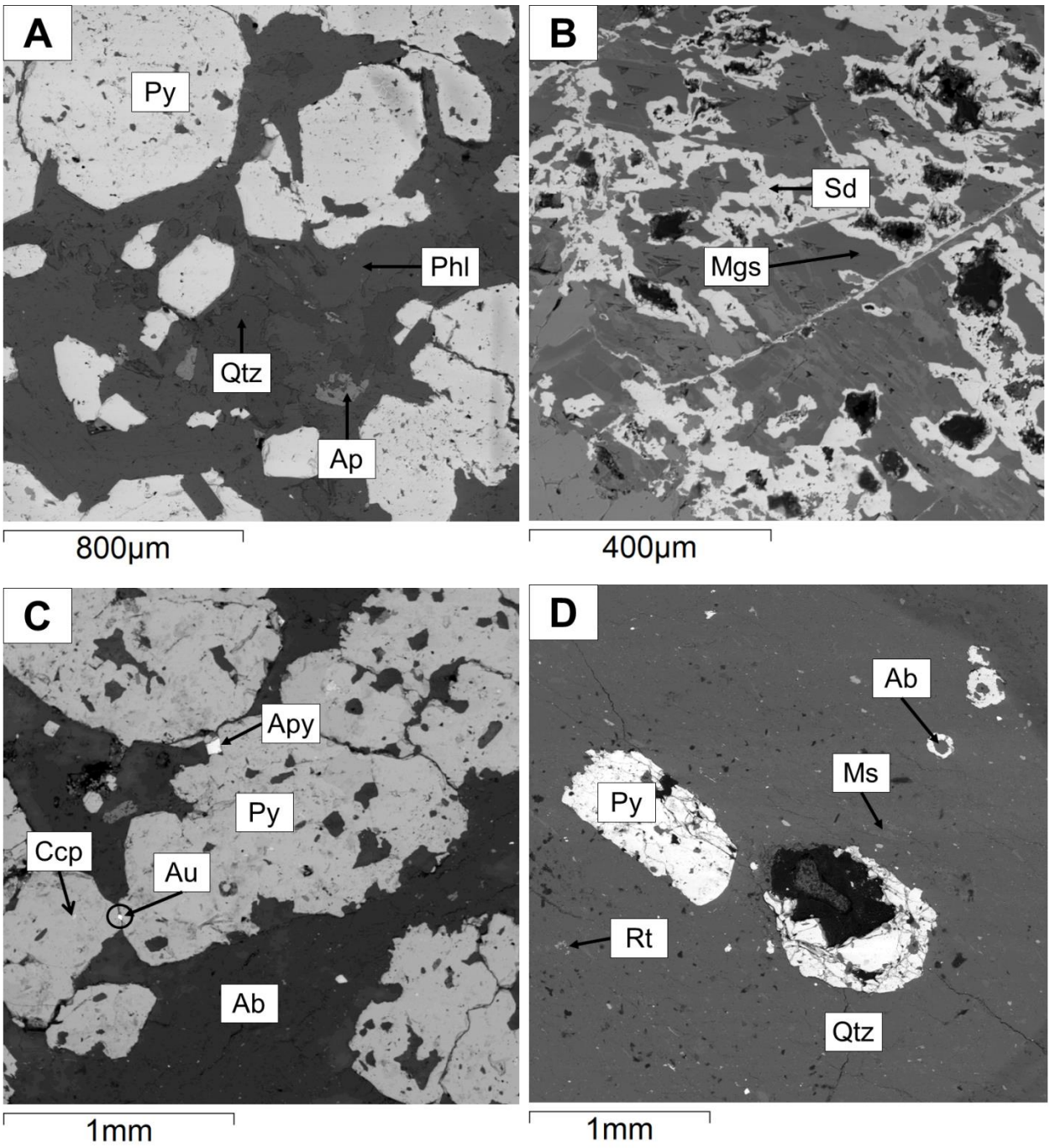

Figure 36. Backscattered electron photomicrographs of the mineralized black shale. A. Pyrite (Py) aggregation in phlogopite-rich (Phl) matrix within the sulphide-rich lens (MBS1); B. Magnesite (Mgs) and siderite (Sd) overgrowing the quartz vein (MBS3B); C. Gold occurring between pyrites (Py) with intergrowing arsenopyrite (Apy) and chalcopyrite (Ccp) (MBS3A); D. Subhedral fractured pyrite (Py) in quartz-rich (Qtz) matrix associated with albite (Ab), muscovite (Ms) and rutile (Rt) (MBS1).

III.2.2. Unmineralized black shale samples

The sulphide phases identified in the unmineralized black shale consist of pyrrhotite, pyrite, arsenopyrite and rare chalcopyrite (Figure 37). The different pyrite textures investigated are: (i) fine-grained crystals randomly scattered in the quartz-rich matrix associated with albite, muscovite and occasionally dolomite; (ii) anhedral pyrite having quartz and albite minerals as inclusions, and apatite which contain minor fluorine and zircon occurring in its vicinity; (iii) aggregates of fine-grained anhedral pyrite crystals in a quartz-rich matrix associated with muscovite and albite within spherical nodules, containing quartz inclusions (Figure 41A); (iv) subhedral pyrite with albite inclusions, and fine-grained rutile and monazite occurring in its vicinity within the rock matrix; (v) anhedral annealed pyrite clustered in sulphide lenses with an albite-rich matrix and with tourmaline, albite and pyrophyllite inclusions (Figure 41C); (vi) euhedral zoned pyrite within the quartz vein with monazite occurring in its vicinity, and fine-grained anhedral pyrite occurring towards the rims of the vein (Figure 41D); and (vii) anhedral pyrite distributed in the form of short stringers occurring in the quartz and albite-rich matrix associated with dolomite, monazite and rutile, and having vermiculite as inclusion.

The pyrite with different textures in the unmineralized black shale has uniform composition with S values ranging from 53.50 to 54.80 wt. % and 44.80 to 46.40 wt. % of Fe (Table 5). The As concentration is generally low, not visible on the spectrum, and is estimated to be up to 0.49 wt. % (Figure 37A; Table 5).

The arsenopyrite finely scattered in the matrix contains minor Ni of up to ~0.70 wt. % (Figure 37E), whereas the arsenopyrite locally intergrown with pyrrhotite does not contain Ni (Figure 37D; Table 5).

The pyrrhotite occurs in a quartz-rich matrix associated with chlorite (Figure 37B; Figure 41B). The chalcopyrite is found as inclusions in pyrite within the sulphide lens and has lower amounts of Cu compare to the mineralized black shale, probably substituted by Fe, which is in excess, as attested by the normalization to 4 atoms that estimate the value of Cu cations to 0.67 and 1.28 for Fe anions (Table 5; Figure 37C).

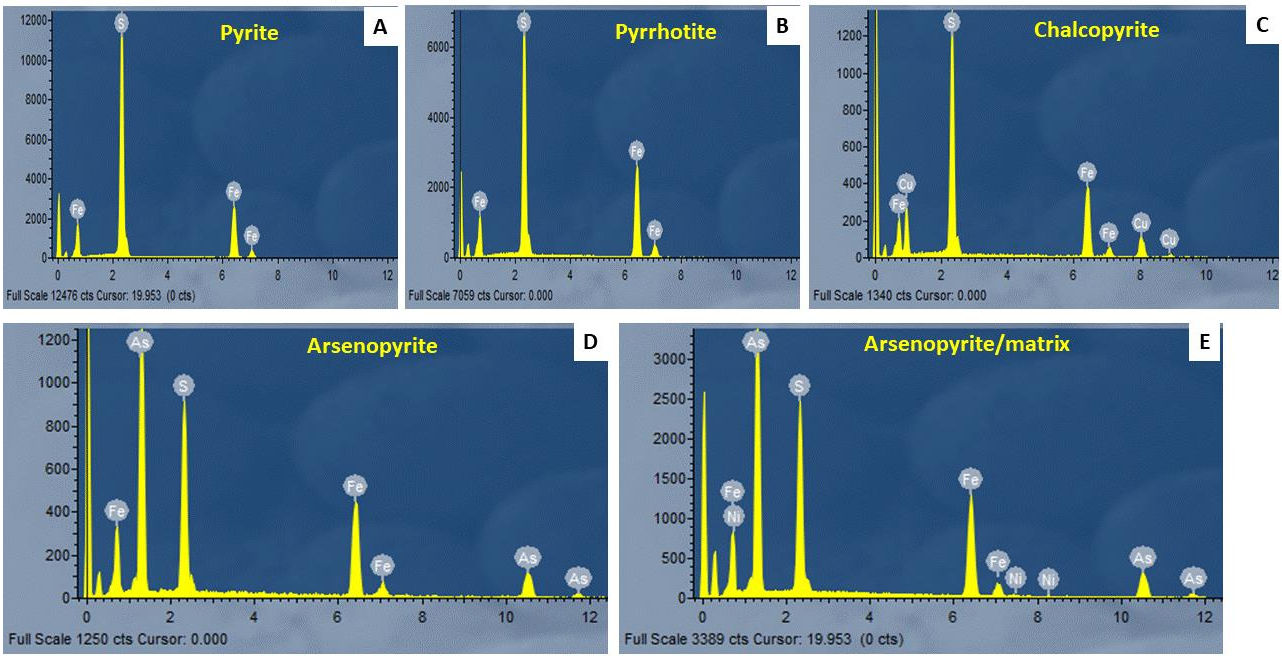

Figure 37. EDS spectra of the unmineralized black shale sulphides. A. Spectrum of pyrite; B. Spectrum of pyrrhotite; C. Spectrum of chalcopyrite; D. Spectrum of arsenopyrite; E. Spectrum of arsenopyrite from the scattered fine-grained crystals within the matrix.

Table 5. Chemical compositions of sulphides associated with unmineralized black shales.

	Matrix		**Anhedral pyrite**			**Subhedral pyrite**	**Sulphide lens**		**Vein**			
	UMBS11	UMBS12B	UMBS11	UMBS9	UMBS9	UMBS4	UMBS4	UMBS4	UMBS4	UMBS12B	UMBS4	
	Pyrite	Arsenopyrite	Pyrite	Pyrrhotite	Arsenopyrite	Pyrite	Pyrite	Chalcopyrite	Pyrite	Pyrite stringer	Zoned pyrite	
Wt. % (atom)											*Inner*	*Outer*
Fe	45.53	33.44	45.80	58.37	33.88	46.39	45.92	39.88	44.87	45.46	45.16	44.93
S	54.01	21.91	54.16	41.49	22.35	53.64	53.59	37.06	54.71	54.29	54.80	54.75
As	0.46	43.95	0.04	0.15	43.77	0.00	0.49	0.18	0.41	0.25	0.04	0.33
Ni	0.00	0.70	0.00	0.00	0.00	0.00	0.00	0.00	0.00	0.00	0.00	0.00
Cu	0.00	0.00	0.00	0.00	0.00	0.00	0.00	22.88	0.00	0.00	0.00	0.00
Total	100.00	100.00	100.00	100.01	100.00	100.03	100.00	100.00	99.99	100.00	100.00	100.01
Ions (normalis.)												
Fe	0.98	0.96	0.98	6.70	0.96	1.00	0.99	1.28	0.96	0.97	0.96	0.96
S	2.02	1.09	2.02	8.29	1.11	2.00	2.01	2.07	2.04	2.02	2.04	2.04
As	0.01	0.94	0.00	0.01	0.93	0.00	0.01	0.00	0.01	0.00	0.00	0.01
Ni	0.00	0.02	0.00	0.00	0.00	0.00	0.00	0.00	0.00	0.00	0.00	0.00
Cu	0.00	0.00	0.00	0.00	0.00	0.00	0.00	0.65	0.00	0.00	0.00	0.00
Total	3	3	3	15	3	3	3	4	3	3	3	3

The quartz is often associated with albite and muscovite in the unmineralized black shale matrix. Quartz is also associated with chlorite (Figure 38A; Table 6) and rare fine-grained scattered ferrierite $(Na,K)_2Mg(Si,Al)_{18}O_{36}.9H_2O$) (Figure 38C; Table 6) in the matrix of pyrrhotite-rich samples. The organic matter, consisting of extremely fine non-crystalline carbon (Figure 38B), is ranndomly distributed within the sample matrix and is responsible for the blackish colour of the rock. The carbon is attested by the carbon peak as investigated in the rock matrix and accounts for approximately 98 wt%.

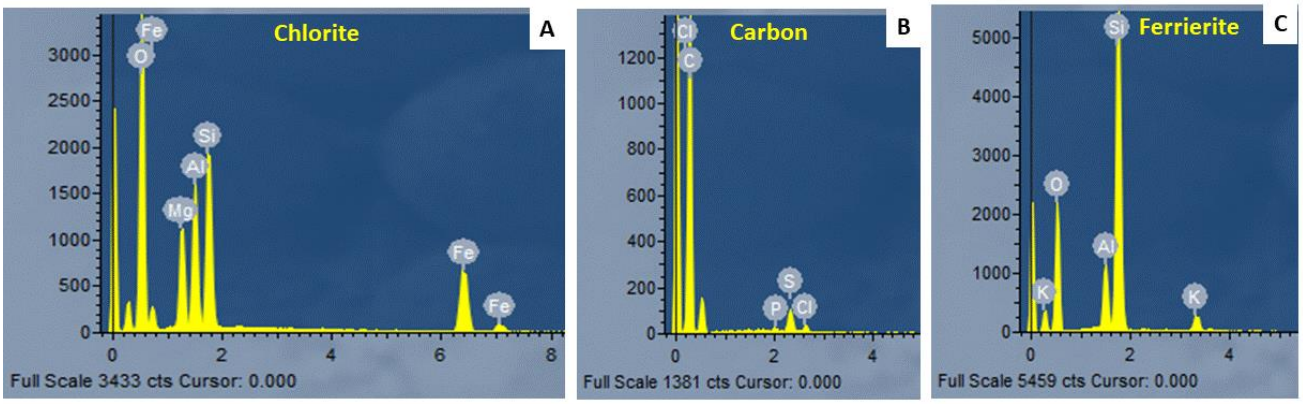

Figure 38. EDS spectra of minor phases associated with quartz within the unmineralized black shale matrix. A. Spectrum of chlorite; B. Spectrum of carbon; C. Spectrum of ferrierite.

The crosscutting quartz vein is associated with minor fine-grained crystals of magnesite (Figure 39B) and / or apatite with minor fluorine, rutile (Figure 39E), dolomite (Figure 39D), and rare thortveitite ($(Sc,Y)_2Si_2O_7$) (Figure 39A) and gaspeite ($(Ni,Mg)CO_3$) (Figure 39F) (Table 6). The pyrite occurring in the vein has albite, muscovite, and vermiculite (Figure 39C) as inclusions (Table 6).

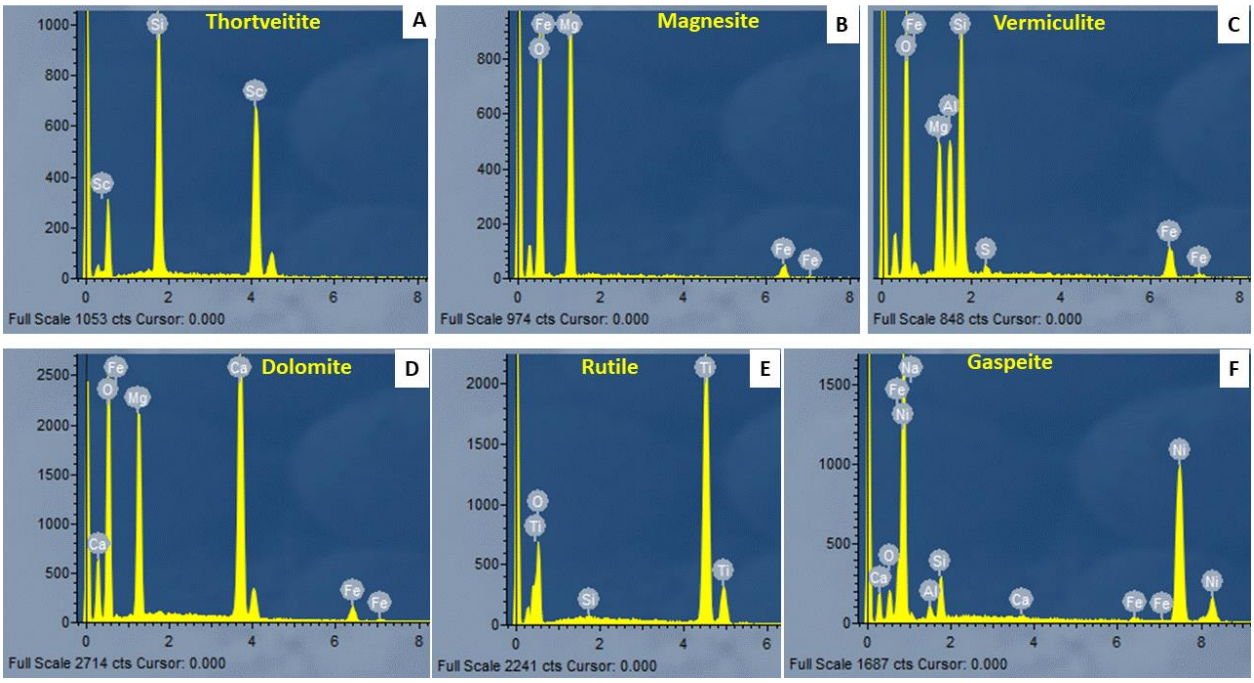

Figure 39. EDS spectra of fine-grained scattered crystals associated with the quartz-vein crosscutting the unmineralized black shale. A. Spectrum of thortveitite; B. Spectrum of magnesite; C. Spectrum of vermiculite; D. Spectrum of dolomite; E. Spectrum of rutile; F. Spectrum of gaspeite.

In the sulphide-rich lens, rare pyrophyllite ($Al_2Si_4O_{10}(OH)_2$) (Figure 40A) and tourmaline (Figure 40B) are found as inclusions within the pyrite (Table 6).

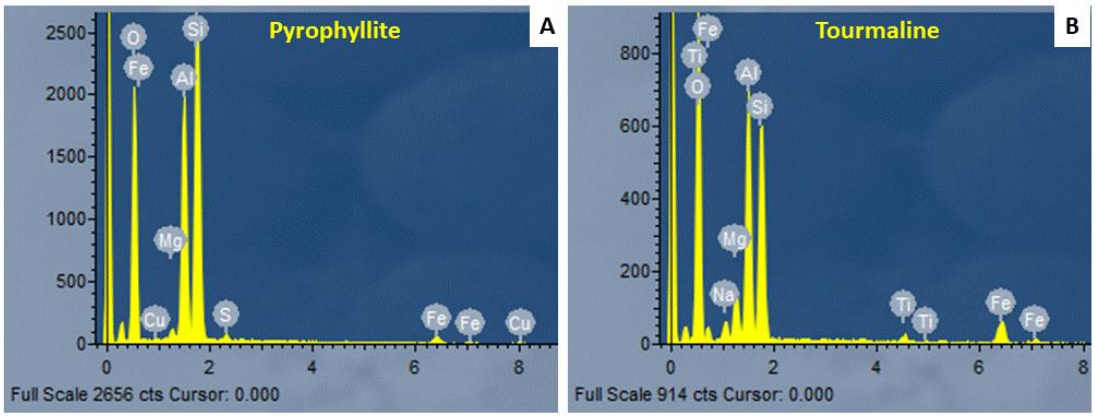

Figure 40. EDS spectra of inclusion minerals within pyrite in the sulphide-rich lens. A. Spectrum of pyrophyllite; B. Spectrum of tourmaline.

Table 6. Chemical compositions of silicates, carbonates, oxides and phosphates phases associated with unmineralized black shales

	UMBS12B	UMBS11	UMBS12B	UMBS12B	UMBS12B	UMBS11	UMBS12B	UMBS9	UMBS9	UMBS4A	UMBS4A	UMBS4A	UMBS4A	UMBS12B	UMBS12B
	Albite	Muscovite	Quartz	Dolomite	Zircon	Rutile	apatite	Chlorite	Ferrierite	Pyrophyllite	Tourmaline	Magnesite	Thorveiitite	Gaspeite	Vermiculite
(Wt%)															
SiO2	70.23	49.92	99.20	0.00	31.25	0.64	0.00	31.26	73.19	59.86	38.49	0.00	46.84	4.79	35.51
Al2O3	18.44	34.66	0.00	0.00	0.08	0.24	0.68	20.35	11.07	30.28	30.25	0.00	0.17	1.33	15.52
Fe2O3	0.00	0.00	0.00	0.00	0.00	0.00	0.00	0.00	0.00	0.00	0.00	0.00	0.00	0.00	0.00
Cr2O3	0.00	0.00	0.00	0.00	0.00	0.21	0.00	0.00	0.00	0.00	0.00	0.00	0.00	0.00	0.00
TiO2	0.12	0.24	0.00	0.00	0.07	97.84	0.00	0.12	0.00	0.00	1.22	0.00	0.00	0.00	0.00
FeO	0.16	0.98	0.00	4.00	0.15	0.38	0.75	23.74	0.00	3.03	8.66	6.74	0.26	0.39	10.37
MgO	0.00	0.62	0.00	19.48	0.07	0.20	0.03	13.68	0.25	0.90	5.90	42.31	0.24	0.07	14.41
MnO	0.00	0.08	0.00	0.15	0.00	0.04	0.22	0.14	0.00	0.00	0.00	0.00	0.01	0.00	0.17
CaO	0.00	0.00	0.00	29.57	0.06	0.10	49.88	0.17	0.09	0.00	0.00	0.05	0.24	0.24	0.20
Na2O	11.14	0.33	0.00	0.00	0.00	0.00	0.01	0.17	0.18	0.00	2.59	0.00	0.00	1.12	0.01
K2O	0.00	8.68	0.00	0.00	0.00	0.00	0.00	0.38	3.23	0.00	0.00	0.00	0.00	0.00	0.00
F	0.00	0.00	0.00	0.00	0.00	0.00	5.54	0.00	0.00	0.00	0.00	0.00	0.00	0.00	0.00
NiO	0.00	0.00	0.00	0.00	0.00	0.00	0.00	0.00	0.00	0.00	0.00	0.00	0.00	52.06	0.00
Sc2O3	0.00	0.00	0.00	0.00	0.00	0.00	0.00	0.00	0.00	0.00	0.00	0.00	51.13	0.00	0.00
Y2O3	0.00	0.00	0.00	0.00	0.00	0.00	0.00	0.00	0.00	0.00	0.00	0.00	0.75	0.00	0.00
SO3	0.00	0.00	0.00	0.00	0.00	0.00	0.00	0.00	0.00	0.00	0.00	0.00	0.00	0.00	1.93
Ta2O5	0.00	0.00	0.00	0.00	0.00	0.09	0.00	0.00	0.00	0.00	0.00	0.00	0.00	0.00	0.00
ZrO2	0.00	0.00	0.00	0.00	66.47	0.00	0.00	0.00	0.00	0.00	0.00	0.00	0.00	0.00	0.00
HfO2	0.00	0.00	0.00	0.00	1.48	0.00	0.00	0.00	0.00	0.00	0.00	0.00	0.00	0.00	0.00
Nb2O5	0.00	0.00	0.00	0.00	0.00	0.27	0.00	0.00	0.00	0.00	0.00	0.00	0.00	0.00	0.00
P2O5	0.00	0.00	0.00	0.00	0.39	0.00	43.02	0.00	0.00	0.00	0.00	0.00	0.00	0.00	0.00
Total	100.09	95.51	99.20	53.20	100.02	99.65	100.13	90.01	88.01	94.06	87.11	49.09	99.64	60.00	78.11

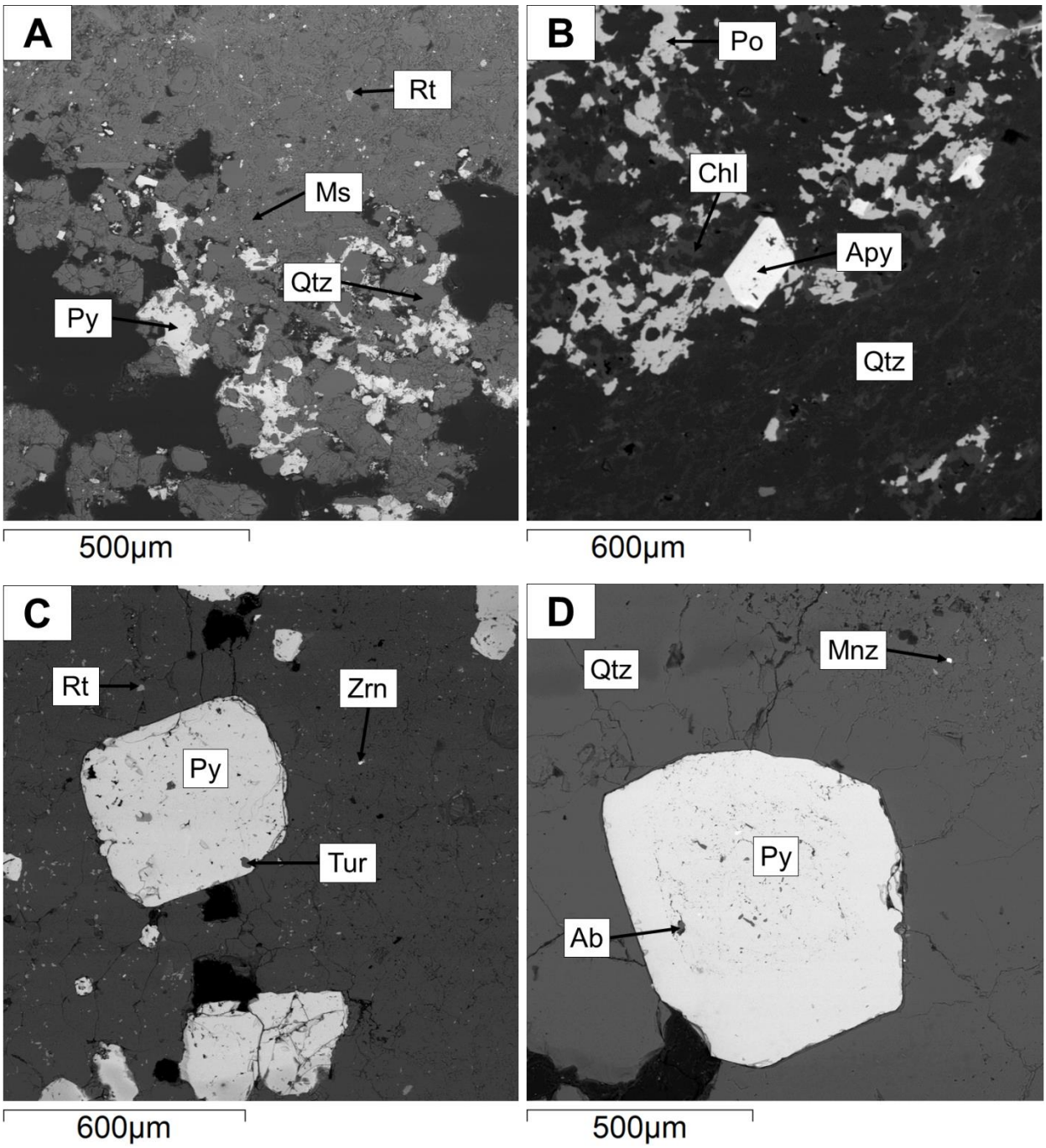

Figure 41. Backscattered electron photomicrographs of unmineralized black shale. A. Aggregate of fine-grained pyrite (Py) in spherical body rich in quartz (Qtz) associated with muscovite (Ms) and rutile (Rt) matrix (UMBS11); B. Fine-grained anhedral pyrrhotite (Po) and arsenopyrite (Apy) in quartz-rich (Qtz) matrix associated with chlorite (Chl) (UMBS9); C. Euhedral pyrite (Py) occurring with tourmaline (Tur), zircon (Zrn) and rutile (Rt) (UMBS4A) in the sulphide-rich lens; D. Zoned pyrite (Py) and monazite (Mnz) within the quartz (Qtz) vein (UMBS4A).

III.2.3. Mineralized granitoid samples

The different sulphide phases investigated in the mineralized granitoid samples are pyrite, arsenopyrite, chalcopyrite, and locally pyrrhotite. The different pyrite textures investigated consist of: (i) fine-grained pyrite randomly distributed in the albite-rich matrix associated with overgrowing dolomite and minor siderite, muscovite as well as fine-grained scattered apatite with minor fluorine, rutile, chlorite, and barite; (ii) anhedral pyrite in the albite-rich matrix associated with dolomite, siderite, muscovite, vermiculite, apatite, and rutile occurring in its vicinity and showing albite, arsenopyrite and chalcopyrite as inclusions (Figure 44A&B); (iii) euhedral pyrite (Figure 44C) in the albite-rich matrix associated with overgrowing ankerite and siderite, and scattered fine-grained apatite, monazite, and rutile, with albite, chalcopyrite, and pyrrhotite as inclusions; and (iv) fine-grained pyrite (Figure 42A, Table 7) occurring together with rutile, phlogopite and vermiculite toward the rims of the dolomite vein which crosscuts the mineralised granitoid sample.

The arsenopyrite (Figure 42B), chalcopyrite (Figure 42D) and pyrrhotite (Figure 42C) form inclusions within pyrite (Table 7).

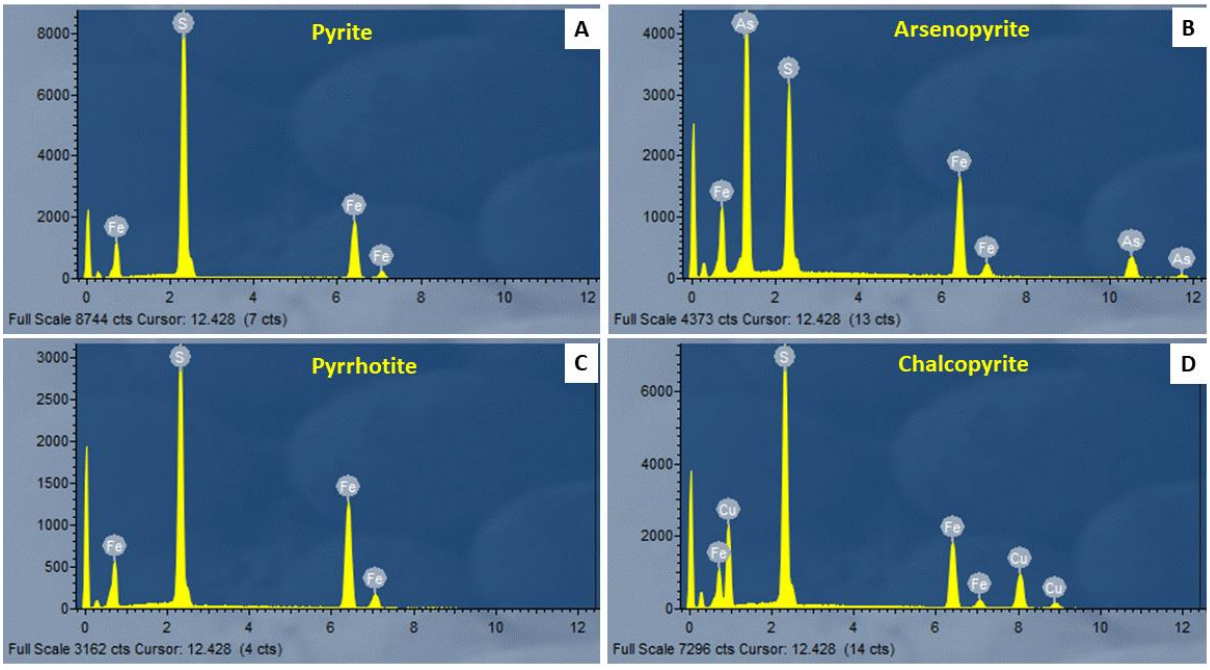

Figure 42. EDS spectra of mineralized granitoid sulphides. A. Spectrum of pyrite; B. Spectrum of arsenopyrite; C. Spectrum of pyrrhotite; D. Spectrum of chalcopyrite.

The pyrite composition is uniform in all the different textural varieties. The Fe value ranges from 47.73 to 45.85 wt. % while the S value ranges from 53.93 to 55.25 wt. % (Table 7). The As content is below the detection limit.

The chalcopyrite which occur as inclusions within the different textural pyrite crystals has almost the same composition.

Table 7. Chemical composition of sulphides associated with the mineralized granitoid

	Matrix	Anhedral pyrite			Euhedral pyrite			Vein
	MGR17	MGR17	MGR17	MGR20	MGR20	MGR17	MGR17	MGR17
wt% (atom)	Pyrite	Pyrite	Arsenopyrite	Chalcopyrite	Pyrite	Pyrrhotite	Chalcopyrite	Pyrite
Fe	45.21	45.44	34.60	31.24	45.85	60.68	30.47	44.73
S	54.66	54.50	21.90	36.63	53.93	39.32	35.83	55.25
As	0.13	0.06	43.50	0.02	0.22	0.00	0.11	0.03
Ni	0.00	0.00	0.00	0.00	0.00	0.00	0.00	0.00
Cu	0.00	0.00	0.00	32.11	0.00	0.00	33.59	0.00
Total	100	100	100	100	100	100	100	100
Ions (normalis.)								
Fe	0.97	0.97	0.99	1.01	0.98	7.05	1.00	0.95
S	2.03	2.03	1.09	2.07	2.01	7.95	2.04	2.05
As	0.00	0.00	0.92	0.00	0.00	0.00	0.00	0.00
Ni	0.00	0.00	0.00	0.00	0.00	0.00	0.00	0.00
Cu	0.00	0.00	0.00	0.92	0.00	0.00	0.96	0.00
Total	3	3	3	4	3	15	4	3

Albite is the main phase of the matrix and is composed of Na, Si and Al showing the endmember composition in all analysed points (Table 8). It is associated with overgrowing dolomite, minor ankerite and siderite, and fine-grained scattered muscovite, apatite, rutile, zircon, chlorite and occasional barite ($BaSO_4$) (Figure 43). Zircon contains small concentrations of Sc and Fe of ~ 0.82 wt. % while the apatite contains small concentrations of W of ~ 0.69 wt%. The barite shows small peaks of Co content. The carbonate vein that crosscuts the mineralized granitoid consists of dolomite associated with minor magnesite, siderite and phlogopite in the contact with the host rock (Figure 44D).

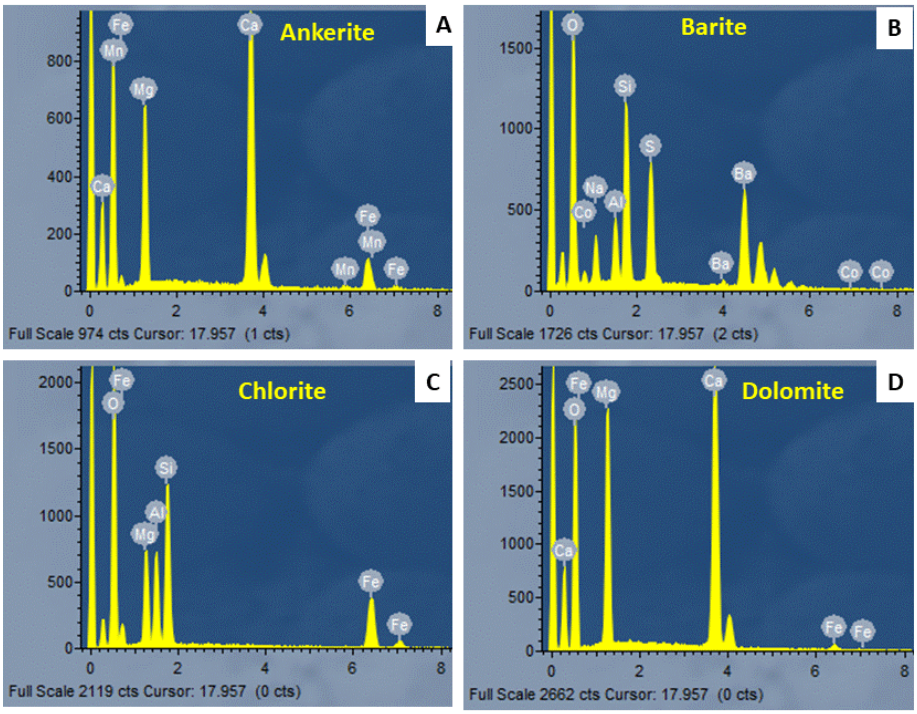

Figure 43. EDS spectra of some oxide phases associated with albite in the granitoid matrix. A. Spectrum of ankerite; B. Spectrum of barite; C. Spectrum of chlorite; D. Spectrum of dolomite.

Table 8. Chemical composition of oxides, silicates, carbonates, sulfates and phosphates phases associated with the mineralized granitoid

	MGR17	MGR17	MGR20	MGR17	MGR20	MGR20	MGR20	MGR17	MGR17	MGR17	MGR17	MGR17	MGR17
	Muscovite	Albite	apatite	Rutile	Dolomite	Barite	Chlorite	Siderite	Vermiculite	Ankerite	Zircon	Magnesite	Phlogopite
(Wt%)													
SiO2	48.64	69.77	0.75	0.00	0.00	0.00	32.94	0.00	38.42	0.00	32.32	0.00	41.32
Al2O3	33.97	18.66	0.00	0.12	0.00	0.00	15.43	0.00	10.67	0.00	1.23	0.00	13.06
Fe2O3	0.00	0.00	0.00	0.00	0.00	0.00	0.00	0.00	0.00	0.00	0.00	0.00	0.00
Cr2O3	0.00	0.00	0.00	0.21	0.00	0.00	0.00	0.00	0.00	0.00	0.00	0.00	0.00
TiO2	0.29	0.05	0.00	96.47	0.00	0.00	0.00	0.00	0.00	0.00	0.30	0.00	0.11
FeO	0.30	0.13	0.56	0.04	1.34	0.00	23.97	53.54	7.06	8.09	0.84	23.72	3.86
MgO	1.20	0.00	0.12	0.06	20.56	0.00	15.40	1.44	23.68	16.82	0.00	24.03	23.49
MnO	0.09	0.00	0.00	0.22	0.00	0.00	0.00	5.05	0.00	0.75	0.00	0.13	0.00
CaO	0.00	0.15	47.60	0.75	28.88	0.21	0.15	1.97	0.11	29.12	0.65	0.04	0.10
Na2O	0.62	11.17	0.00	0.00	0.00	0.00	0.11	0.00	0.06	0.00	0.00	0.08	0.15
K2O	9.98	0.10	0.04	0.00	0.00	0.00	0.11	0.00	0.00	0.00	0.00	0.00	8.82
BaO	0.00	0.00	0.00	0.00	0.15	62.88	0.00	0.00	0.00	0.24	0.00	0.00	0.00
F	0.00	0.00	5.56	0.00	0.00	0.00	0.00	0.00	0.00	0.00	0.00	0.00	5.38
SO3	0.00	0.00	0.00	0.00	0.00	36.91	0.00	0.00	0.00	0.00	0.00	0.00	0.00
SrO	0.00	0.00	0.28	0.00	0.00	0.00	0.00	0.00	0.00	0.00	0.00	0.00	0.00
ZrO2	0.00	0.00	0.00	0.00	0.00	0.00	0.00	0.00	0.00	0.00	62.77	0.00	0.00
HfO2	0.00	0.00	0.00	0.00	0.00	0.00	0.00	0.00	0.00	0.00	0.00	0.00	0.00
Nb2O5	0.00	0.00	0.00	0.46	0.00	0.00	0.00	0.00	0.00	0.00	0.00	0.00	0.00
Ta2O5	0.00	0.00	0.00	0.51	0.00	0.00	0.00	0.00	0.00	0.00	0.00	0.00	0.00
P2O5	0.00	0.00	40.08	0.00	0.00	0.00	0.00	0.00	0.00	0.00	0.00	0.00	0.00
V2O5	0.00	0.00	0.00	0.65	0.00	0.00	0.00	0.00	0.00	0.00	0.00	0.00	0.00
WO3	0.00	0.00	0.69	0.00	0.00	0.00	0.00	0.00	0.00	0.00	0.00	0.00	0.00
Sc2O3	0.00	0.00	0.00	0.00	0.00	0.00	0.00	0.00	0.00	0.00	1.29	0.00	0.00
Total	95.08	100.03	94.99	98.84	50.94	100.00	88.09	62.00	80.00	55.03	99.40	48.00	96.28

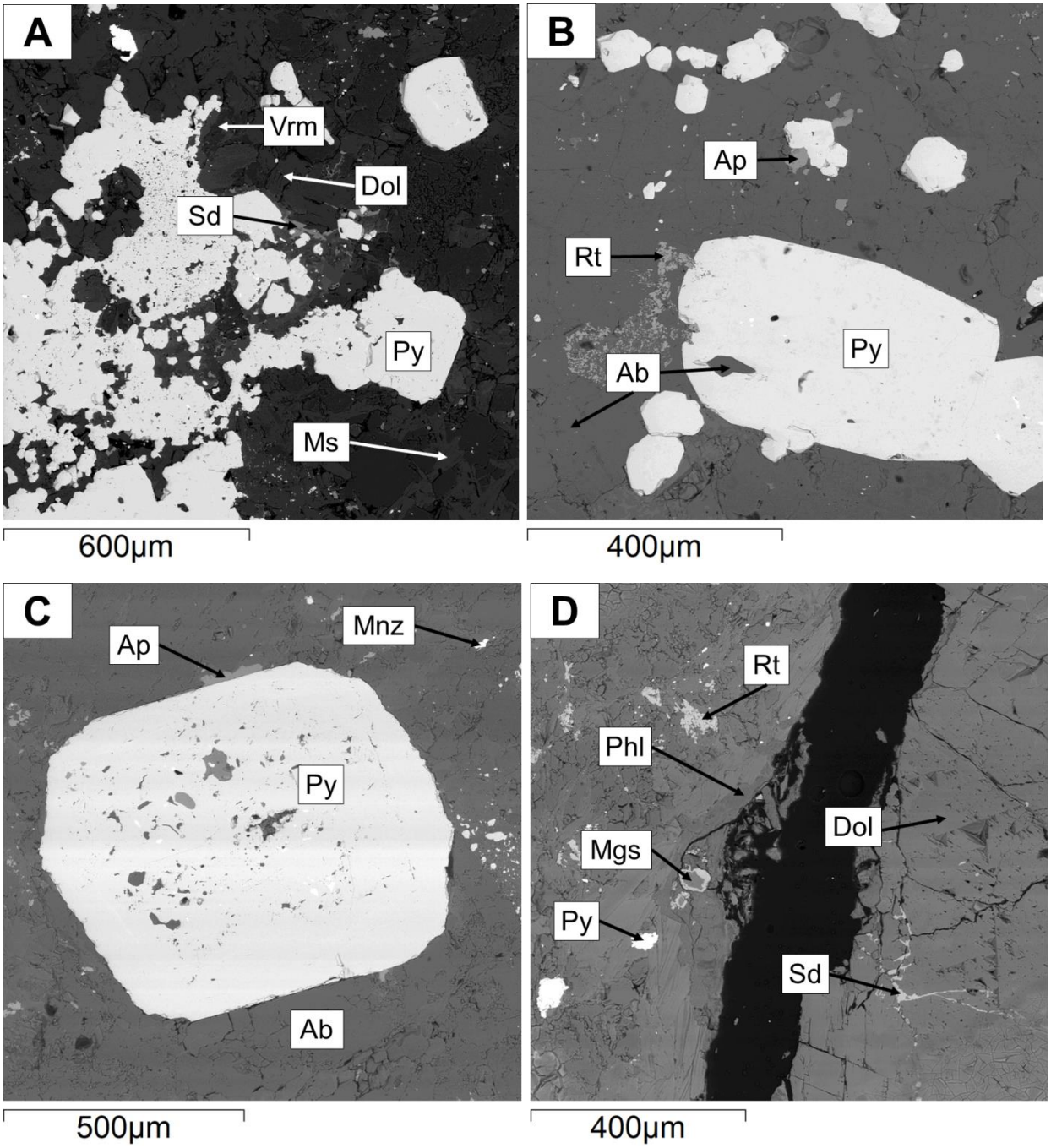

Figure 44. Backscattered electron photomicrographs of mineralized granitoid. A. Anhedral pyrite (Py) occurring in dolomite –rich (Dol) matrix associated with siderite (Sd), vermiculite (Vrm), and muscovite (Ms) (MGR17); B. Anhedral pyrite (Py) within albite-rich matrix with associated rutile (Rt) and apatite (Ap) (MGR 20); C. Euhedral pyrite (Py) in albite-rich (Ab) matrix with associated monazite (Mnz) and apatite (Ap) (MGR 17); D. Dolomite (Dol) vein associated with interstitial siderite (Sd) and phlogopite (Phl), rutile (Rt), magnesite (Mgs) and pyrite (Py) in contact with the host rock (MGR17)

III.2.4. Unmineralized granitoid samples

The different sulphide phases identified in the unmineralized granitoid are pyrite, pyrrhotite, and occasionally cobaltite (CoAsS). The pyrite texture investigated consists essentially of anhedral pyrite (Figure 45A) in an albite-rich matrix associated with overgrowing ankerite, minor magnesite and siderite, and fine-grained scattered rutile, fluor-apatite, monazite, and zircon (Figure 47A&C). Muscovite and rutile are found as inclusions within the anhedral pyrite.

The anhedral pyrrhotite (Figure 45B) occurs in the albite-rich matrix associated with overgrowing ankerite and chlorite, as well as fine-grained scattered rutile and apatite with minor fluorine (Figure 47B&D). Chlorite in the unmineralized black shale has Mg>Fe compare to that of the mineralized granitoid.

The cobaltite (Figure 45C) is occasionally scattered in the albite-rich matrix and is associated with overgrowing ankerite (Figure 47D).

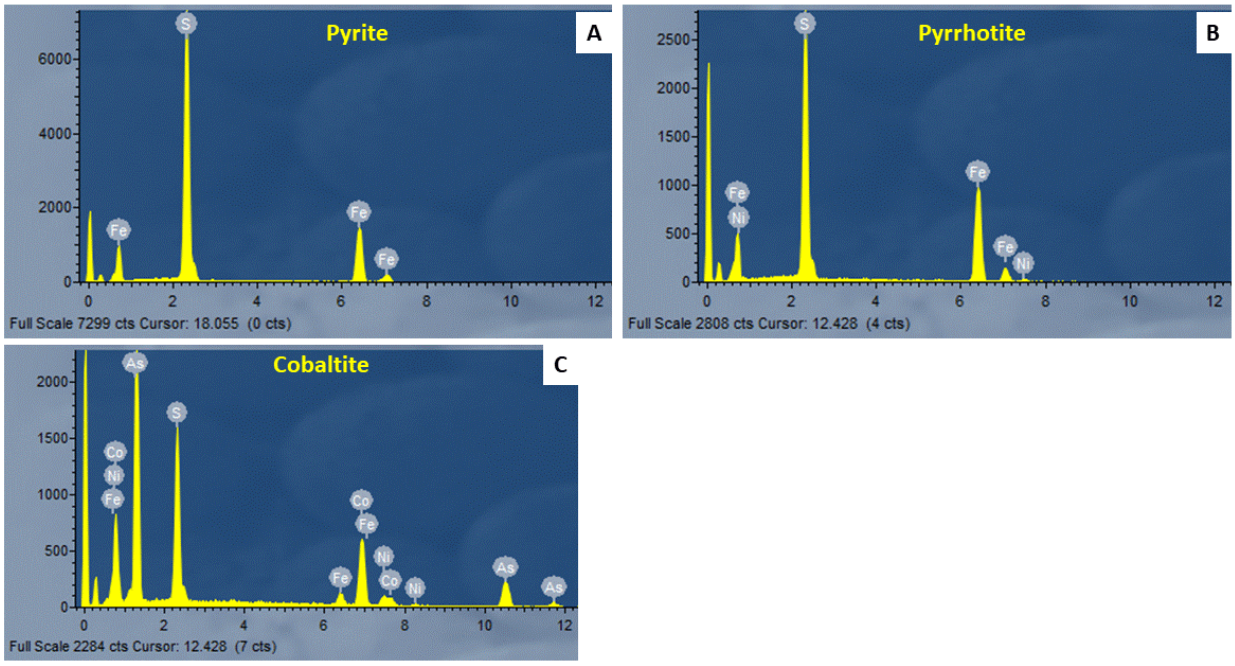

Figure 45. EDS spectra of sulphides associated with the unmineralized granitoids. A. Spectrum of pyrite; B. Spectrum of pyrrhotite; C. Spectrum of cobaltite.

Fe in pyrite is about 44.67 wt. % and S is 55.33 wt. %; As is absent. The pyrrhotite shows minor Ni which accounts for approximately 2.06 wt. %. The cobaltite is also enriched in Ni and Fe with

4.55 wt. % and 3.45 wt. %, respectively. Ni and Fe may have substituted for cobalt, which accounts for 0.76 cations per formula unit (Table 9).

Table 9. Chemical results of sulphides associated with the unmineralized granitoid.

	UGR13	UGR13	UGR10
wt% (atom)	Pyrrhotite	Cobaltite	Pyrite
Fe	56.58	3.45	44.67
S	41.29	20.10	55.33
As	0.07	44.52	0.00
Ni	2.06	4.55	0.00
Cu	0.00	0.00	0.00
Co	0.00	27.37	0.00
Total	100	100	100
Ions (normalis.)			
Fe	6.50	0.10	0.95
S	8.27	1.03	2.05
As	0.01	0.98	0.00
Ni	0.23	0.13	0.00
Cu	0.00	0.00	0.00
Co	0.00	0.76	0.00
Total	15	3	3

Rare fine-grained xenotime (YPO_4) is occasionally found in the albite- and ankerite-rich matrix (Figure 46A). The rutile is enriched in V, Cr and Nb (Figure 46B). The Cr value accounts for 1.15 wt. % and the Nb is 1.06 wt. % (Table 10).

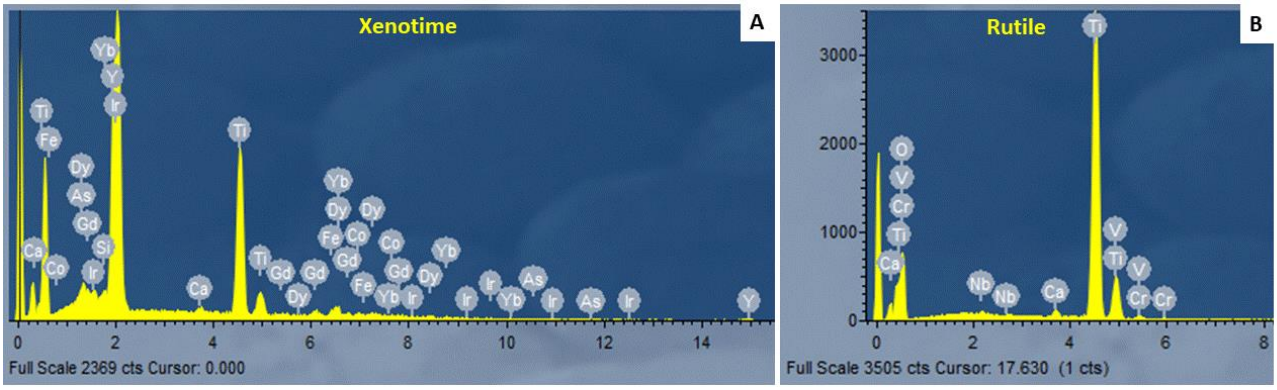

Figure 46. EDS spectra of some of the fine-grained scattered minerals associated with the albite- and ankerite-rich matrix of the unmineralized granitoid. A spectrum of xenotime; B. Spectrum of rutile

Table 10. Chemical compositions of silicates, carbonates, phosphates and oxide phases associated with the unmineralized granitoid

	UGR10	UGR10	UGR10	UGR10	UGR10	UGR10	UGR10	UGR10	UGR13
	Albite	Dolomite	Ankerite	Magnesite	Siderite	Rutile	Fluor-apatite	Muscovite	Chlorite
(Wt%)									
SiO2	70.26	0.00	0.00	0.00	0.00	0.00	0.00	48.90	28.76
Al2O3	18.53	0.00	0.00	0.00	0.00	0.08	0.00	32.89	20.50
Fe2O3	0.00	0.00	0.00	0.00	0.00	0.00	0.00	0.00	0.00
Cr2O3	0.00	0.00	0.00	0.00	0.00	1.15	0.00	0.00	0.05
TiO2	0.01	0.00	0.00	0.00	0.00	94.38	0.00	0.29	0.48
FeO	0.14	6.37	10.96	11.14	37.91	0.26	0.00	1.05	16.70
MgO	0.00	17.05	15.16	36.17	20.85	0.14	0.06	1.01	21.38
MnO	0.00	0.30	0.07	0.30	2.61	0.21	0.09	0.24	0.04
CaO	0.12	28.28	28.72	0.38	0.64	1.00	50.26	0.16	0.07
Na2O	11.10	0.00	0.00	0.00	0.00	0.00	0.00	0.14	0.03
K2O	0.03	0.00	0.00	0.00	0.00	0.00	0.00	9.60	0.03
BaO	0.00	0.00	0.09	0.00	0.00	0.00	0.00	0.00	0.00
Nb2O5	0.00	0.00	0.00	0.00	0.00	1.06	0.00	0.00	0.00
Ta2O5	0.00	0.00	0.00	0.00	0.00	0.11	0.00	0.00	0.00
SrO	0.00	0.00	0.00	0.00	0.00	0.00	0.55	0.00	0.00
F	0.00	0.00	0.00	0.00	0.00	0.00	6.17	0.00	0.00
Li2O	0.00	0.00	0.00	0.00	0.00	0.00	0.00	0.00	0.00
B2O3	0.00	0.00	0.00	0.00	0.00	0.00	0.00	0.00	0.00
P2O5	0.00	0.00	0.00	0.00	0.00	0.00	42.85	0.00	0.00
V2O5	0.00	0.00	0.00	0.00	0.00	0.91	0.00	0.00	0.00
Total	100.19	52.00	55.00	48.00	62.00	98.39	99.98	94.28	88.10

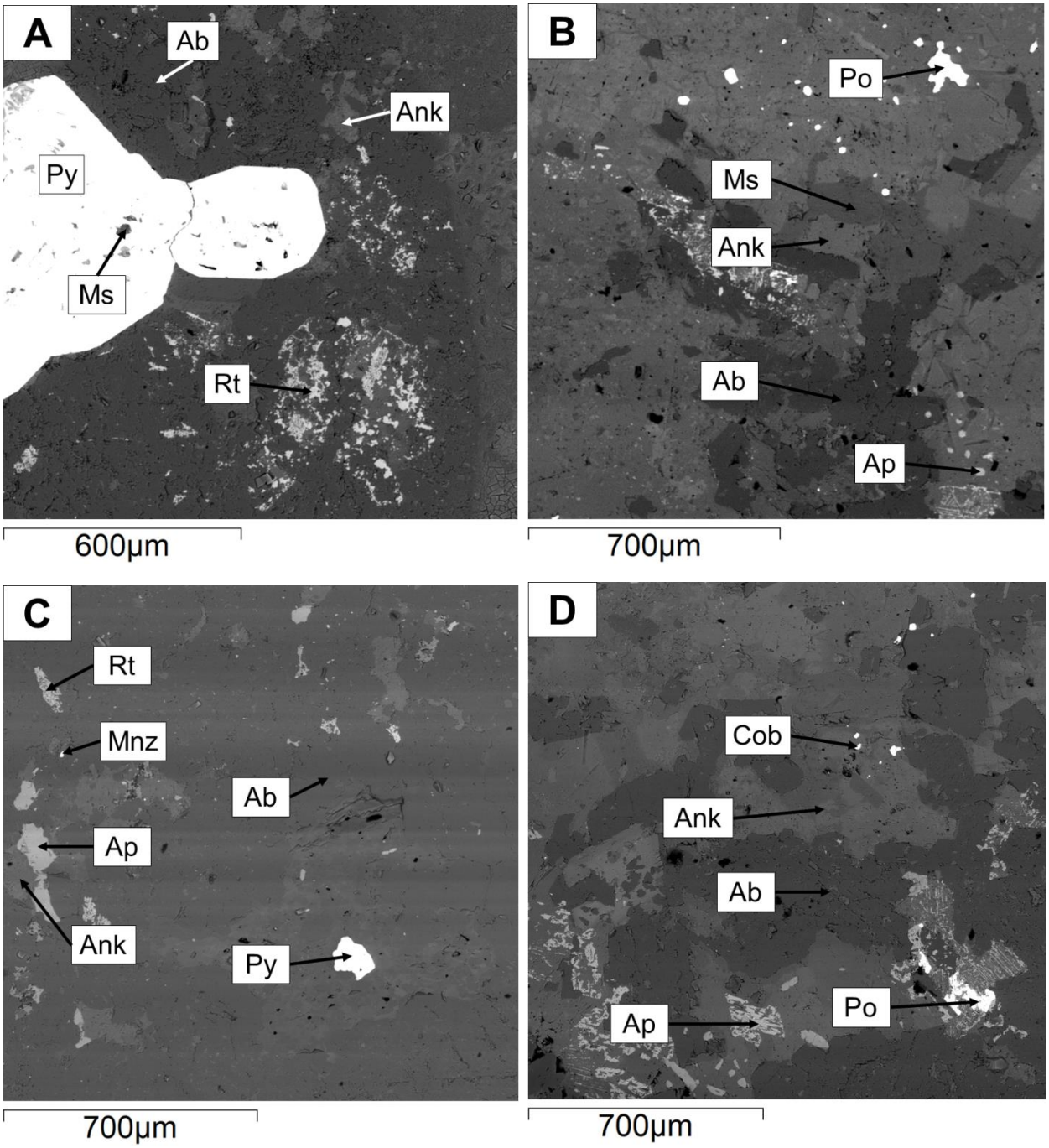

Figure 47. Backscattered electron photomicrographs of unmineralized granitoid. A. Subhedral to anhedral pyrite (Py) within albite-rich (Ab) matrix with overgrowing ankerite (Ank) and rutile (Rt) (UGR10); B. Pyrrhotite (Po) occurring in ankerite-rich (Ank) matrix associated with muscovite (Ms), albite (Ab) and fine-grained apatite (Ap) (UGR13); C. Fine-grained pyrite (Py) in albite-rich (Ab) matrix associated with ankerite (Ank), apatite (Ap), monazite (Mnz), and rutile (Rt) (UGR10); D. Pyrrhotite (Po) and cobaltite (Cob) occurring in ankerite (Ank) and albite (Ab) matrix associated with apatite (Ap) (UGR13).

III.2.5. Hydrothermal vein samples

The different sulphide phases analysed in the hydrothermal vein samples are pyrite and arsenopyrite. The different pyrite textures investigated are: (i) anhedral pyrite occurring in the quartz vein with albite and tourmaline as inclusions; (ii) fine-grained pyrite as inclusions within massive arsenopyrite; (iii) massive pyrite with fine-grained arsenopyrite as inclusions (Figure 51D); (iv) anhedral pyrite abundantly disseminated along the vein selvedge within the host rock, in an albite-rich matrix associated with muscovite, and with fine-grained monazite and arsenopyrite as inclusions (Figure 51B); and (v) euhedral zoned pyrite within the albite-rich matrix associated with minor rutile and monazite, and with albite as inclusions (Figure 51C).

The arsenopyrite (Figure 48C) investigated is found as: (i) anhedral crystals intergrowing with pyrite in the quartz vein; (ii) coarse massive crystals; and (iii) as fine-grained anhedral crystals occurring as inclusions within pyrite.

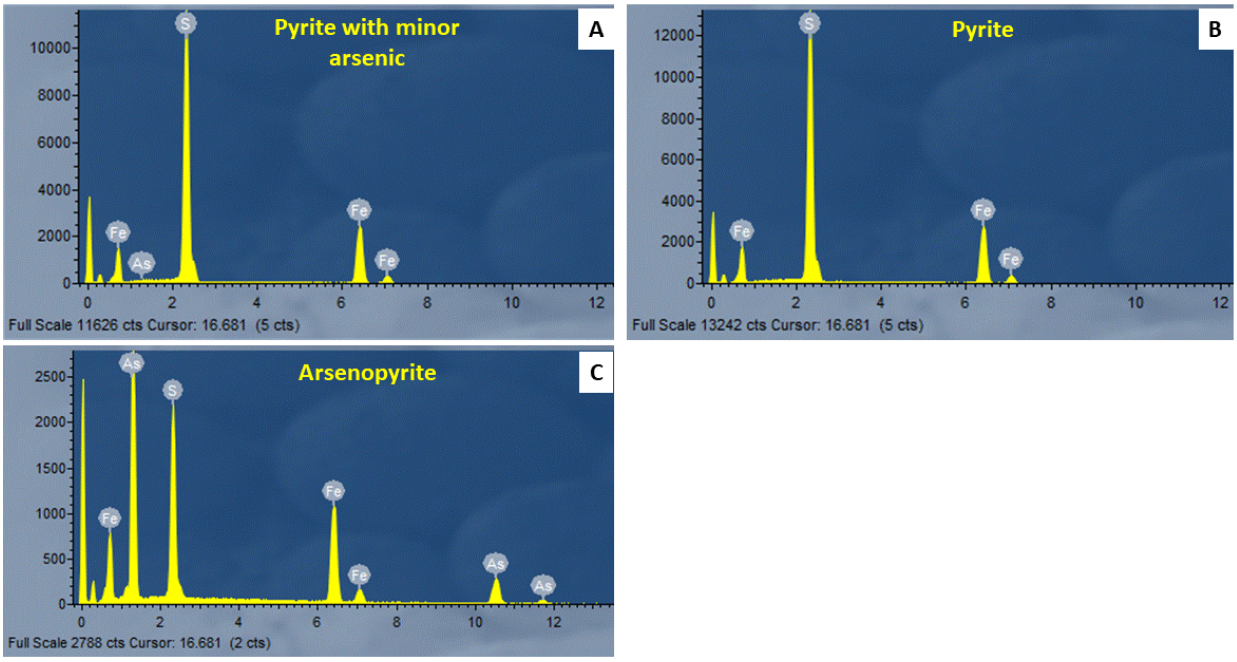

Figure 48. EDS spectra of sulphides associated with hydrothermal veins. A. Spectrum of arsenian pyrite; B. Spectrum of pyrite; C. Spectrum of arsenopyrite.

The different pyrite textural types of hydrothermal veins differs in composition with regards to arsenic content (Figure 48A&B). The Fe content ranges from 44.87 to 45.67 wt. % while the S

content ranges from 53.75 to 54.37 wt. %. The Fe and S values vary with the concentration of As content which ranges from approximately 0.20 up to about 1.07 wt. % (Table 11).

The arsenopyrite shows uniform composition in all the textural types with approximately 35.20 wt. % of Fe, 22.55 wt. % of As, and 42.20 wt. % of S (Table 11).

Table 11. Sulphide compositions in hydrothermal veins.

	Disseminated pyrite	**Anhedral Pyrite**		**Massive sulphide**		**Euhedral zoned pyrite**	
	HVN2	HVN8	HVN8	HVN19	HVN19	HVN19	HVN19
wt% (atom)	Pyrite	Pyrite	Arsenopyrite	Pyrite	Arsenopyrite	Inner part	Outer part
Fe	45.54	44.87	35.14	45.41	35.25	45.18	45.67
S	53.94	54.30	22.46	54.37	22.68	53.75	54.14
As	0.52	0.83	42.41	0.22	42.07	1.07	0.20
Ni	0.00	0.00	0.00	0.00	0.00	0.00	0.00
Cu	0.00	0.00	0.00	0.00	0.00	0.00	0.00
Total	100	100	100	100	100	100	100
Ions (normalis.)							
Fe	0.98	0.96	1.00	0.97	1.00	0.97	0.98
S	2.02	2.03	1.11	2.03	1.12	2.01	2.02
As	0.01	0.01	0.90	0.00	0.89	0.02	0.00
Ni	0.00	0.00	0.00	0.00	0.00	0.00	0.00
Cu	0.00	0.00	0.00	0.00	0.00	0.00	0.00
Total	3	3	3	3	3	3	3

The gold associated with pyrite along the interface area between anhedral pyrite crystals has some traces of Fe which accounts for 1.17 wt% (Figure 49; Figure 51A), which, however, could be a contamination from the pyrite next to the grain.

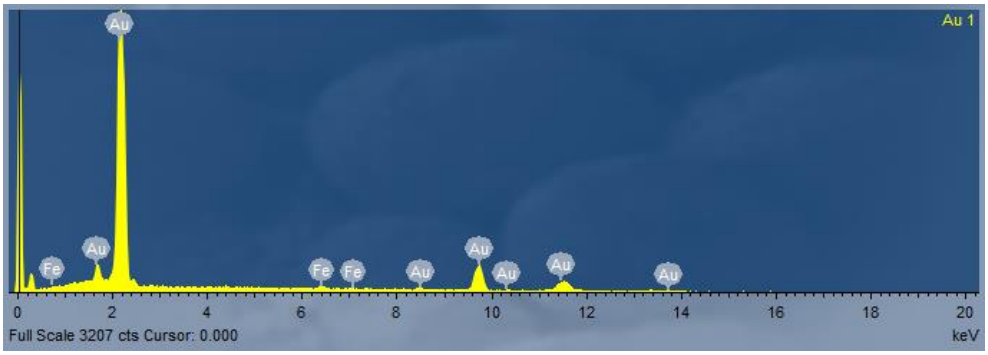

Figure 49. EDS spectrum of gold (Au~98.83 wt%).

The hydrothermal vein matrix consists commonly of quartz, occasionally associated with albite, and fine-grained monazite (Figure 50), muscovite and rutile (Table 12).

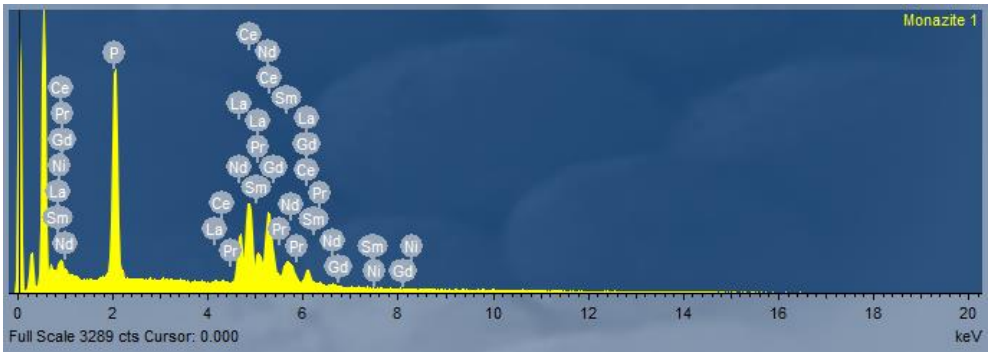

Figure 50. EDS spectrum of monazite.

Table 12. Chemical composition of oxides and silicates in the hydrothermal veins.

	HVN8	HVN8	HVN8	HVN2	HVN2
	Albite	Quartz	Tourmaline	Muscovite	Rutile
(Wt%)					
SiO2	69.84	99.86	38.92	50.88	0.00
Al2O3	18.78	0.00	30.93	30.81	1.59
Fe2O3	0.00	0.00	0.00	0.00	0.00
Cr2O3	0.00	0.00	0.49	0.00	0.69
TiO2	0.00	0.00	0.00	0.03	86.44
FeO	0.30	0.07	2.09	0.80	0.18
MgO	0.00	0.10	9.58	1.34	0.17
MnO	0.00	0.00	0.08	0.00	0.00
CaO	0.04	0.10	0.01	0.02	0.05
Na2O	11.12	0.00	2.14	1.24	1.28
K2O	0.03	0.00	0.02	8.73	0.00
BaO	0.00	0.00	0.00	0.00	0.00
F	0.00	0.00	0.00	0.96	0.00
Nb2O5	0.00	0.00	0.00	0.00	0.26
Ta2O5	0.00	0.00	0.00	0.00	7.95
P2O5	0.00	0.00	0.00	0.00	0.00
V2O5	0.00	0.00	0.00	0.00	0.84
Total	100.11	100.13	84.26	94.81	99.45

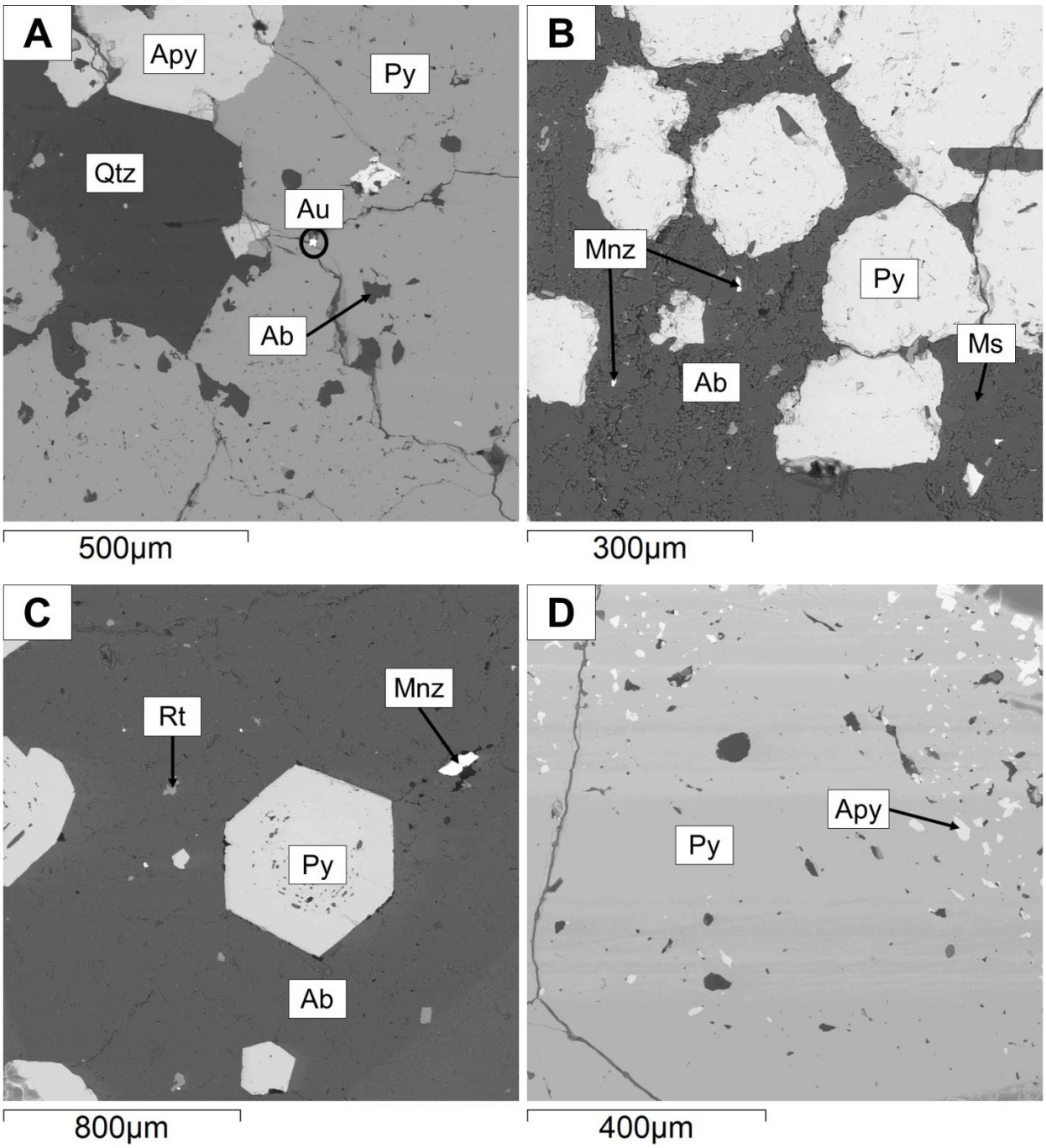

Figure 51. Backscattered electron photomicrographs of hydrothermal vein samples. A. Native gold (Au) along pyrite (Py) crystals interface area (HVN8); B. Disseminated pyrite (Py) along the vein selvedge in albite-rich (Ab) matrix associated with muscovite (Ms) and monazite (Mnz) of the host rock (HVN2); C. Zoned pyrite (Py) in albite-rich (Ab) matrix associated with rutile (Rt) and monazite (Mnz) within the massive sulphide vein (HVN19); D. Arsenopyrite (Apy) as inclusions within pyrite (Py) in massive sulphide vein (HVN19).

IV. DISCUSSION AND INTERPRETATION

The sulphides within Twangiza mine are pyrite, arsenopyrite, pyrrhotite, and chalcopyrite. The EDS analysis has revealed the presence of rare fine-grained cobaltite occurring with pyrrhotite in the unmineralized granitoid sample. By far the most common sulphide phase in the black shale and granitoid, whether mineralized or unmineralized, is pyrite. Arsenopyrite is often found either as inclusions in pyrite or intergrown with pyrite in all sample types. However, in massive sulphides veins, arsenopyrite is the most abundant sulphide. Pyrrhotite occurs as an aggregation of fine-grained anhedral crystals randomly distributed in the unmineralized black shale and unmineralized granitoid. It is also found as fine-grained crystals as inclusion within pyrite in mineralized granitoid. Chalcopyrite is almost exclusively occurring as inclusions within pyrite in mineralized and unmineralized black shales and mineralized granitoid samples.

Different types of sulphide textures are recognized within different sample and rock types.

Table 13. Sulphide textures and associated lithologies, samples and figures

	Textural type	Lithologies	Samples	Figures
Pyrite	Aggregates of fine-grained anhedral crystals in spherical nodules	Unmineraliized black shale	UMBS11	Figures 16C&D
	Aggregates of annealed anhedral pyrite in sulphide-rich lenses	Unmineralized black shale, mineralized black shale	UMBS4A MBS1, MBS3A, MBS3B, MBS6	Figure 13D Figures 8F, 9D, 10C, 11E
	Subhedral to euhedral fine-grained pyrite	Unmineralized black shale, mineralized black shale, mineralized granitoid, and unmineralized granitoid	UMBS4A, UMBS4B, UMBS12A, UMBS12B, MBS1, MBS3B, MBS6, MBS15, MGR17, MGR18, MGR20 UGR14	Figure 13E, 14C&D, 17F, 18F Figure 8E, 10D, 11F, 12E Figure 19E, 20E, 21E Figure 24E
	Elongated anhedral pyrite in the form of stringers	Unmineralized black shale, unmineralized granitoid, and mineralized granitoid	UMBS12B UGR 10 MGR17, MGR18	Figure 18D Figure 22E Figure 19F, 20D
	Aggregates of fine-grained anhedral pyrite	Mineralized granitoid, and Unmineralized granitoid	MGR20 UGR10	Figure 21F Figure 22D

	Euhedral zoned pyrite in vein	Mineralized black shale, Unmineralized black shale, and hydrothermal vein	MBS6 UMBS4A HVN2, HVN16	Figure 11D Figure 13F Figure 25E, 28E
	Dissemination of fine-grained subhedral to anhedral pyrite along the vein selvedge in host rock	Hydrothermal vein	HVN2, HVN16, HVN19	Figures 25D, 29D&F, 30E
	Massive sulphide bodies of pyrite	Hydrothermal vein	HVN5, HVN8, HVN19	Figures 26E&F, 28E, 30D
Arsenopyrite	Fine-grained crystals as inclusions in pyrite	Mineralized black shale Mineralized granitoid Hydrothermal vein	MBS1, MBS3A, MGR17, MGR20 HVN8, HVN19	Figures 36C,
	Medium-grained crystal intergrowing with pyrite	Mineralized black shale Hydrothermal vein	MBS3B HVN8, HVN19	Figure 10C
	Fine-grained anhedral crystal	Unmineralized black shale	UMBS12B	Figure 17E
	Euhedral crystal intergrowing with pyrrhotite	Unmineralized black shale	UMBS9	Figure 15E
	Coarse-grained massive sulphide bodies of arsenopyrite	Hydrothermal vein	HVN8, HVN19	Figure 30D
Pyrrhotite	Fine-grained anhedral patchy crystals	Unmineralized black shale	UMBS9	Figure 15C
	Aggregates of sparse anhedral fine-grained crystals	Unmineralized granitoid	UGR13	Figure 23D
	Fine-grained crystal as inclusion in pyrite	Mineralized granitoid	MGR17	
Chalcopyrite	Fine-grained crystals as inclusion in pyrite	Mineralized black shale Unmineralized black shale Mineralized granitoid	MBS3A UMBS4A MGR17	Figure 36C
Cobaltite	Anhydral fine-grained crystals	Unmineralized granitoid	UGR13	Figure 47D

The pyrite texture specific to the unmineralized black shale consists of the sparse aggregation of fine-grained anhedral crystals into spherical nodules (UMBS11, Figure 16C&D). This texture has been only found within the unmineralized black shale. The aggregation of annealed anhedral pyrite

crystals into sulphide-rich lenses has been recognized in both unmineralized black shale (UMBS4A, Figure 13D) and mineralized black shale (MBS1, Figure 8F; MBS3A, Figure 9D; MBS3B, Figure 10C; and MBS6, Figure 11E). However, the sulphide-rich lenses are mostly developed in the mineralized black shale. The subhedral to euhedral fine-grained pyrite randomly distributed in the rock matrix is found within the mineralized black shale (MBS1, Figure 8E; MBS3B, Figure 10D; MBS6, Figure 11F; and MBS15, Figure 12E), unmineralized black shale (UMBS4A, Figure 13E; UMBS4B, Figure 14C&D; UMBS12A, Figure 17F and UMBS12B, Figure 18F), the mineralized granitoid (MGR17, Figure 19E; MGR18, Figure 20E, and MGR20, Figure 21E), and unmineralized granitoid (UGR14, Figure 24E). In mineralized and unmineralized black shale, it commonly appears disintegrated. The distribution of elongated anhedral pyrite crystals in the form of short stringers has been recognized in unmineralized black shale (UMBS12B, Figure 18D), unmineralized granitoid (UGR10, Figure 22E), and mineralized granitoid (MGR17, Figure 19F; MGR18, Figure 20D). The aggregate of fine-grained anhedral crystals is found in the matrix of mineralized granitoid (MGR20, Figure 21F) and unmineralized granitoid (UGR10, Figure 22D). The euhedral zoned pyrite crystals which occur in veins are found in the veins that crosscut the mineralized black shale (MBS6, Figure 11D) and unmineralized black shale (UMBS4A, Figure 13F) as well as the hydrothermal vein samples (HVN2, Figure 25E; HVN16, Figure 28E). The dissemination of abundant fine-grained subhedral to anhedral crystals of pyrite along the vein selvedge is recognized along the contact of hydrothermal veins with the host rock (HVN2, Figure 25D; HVN16, Figure 29D&F; and HVN19, Figure 30E). The massive sulphide body of pyrite is commonly found in hydrothermal vein samples (HVN5, Figure 26E&F; HVN8, Figure 28E; and HVN19, Figure 30D).

The different pyrite major elemental compositions do not vary significantly from different textures and sample types with Fe content ranging from 44.57 to 46.40 wt. %, and the S content ranges from 53.75 to 55.25 wt. %. However, most of the pyrite crystals from the mineralized black shale and hydrothermal veins have relatively higher concentrations of As (~ 1 wt. %). The unmineralized black shale and the mineralized granitoid's pyrite have relatively lower As concentrations estimated at 0.49 wt. % and 0.22 wt. % respectively.

The aggregate of fine-grained pyrite in the spherical nodules identified in the unmineralized black shale is interpreted as early, probably diagenetic pyrite (Diehl et al., 2005; Steadman, 2015). A well-developed lamination present in the black shale is displaced around nodules (Figure 16C)

suggesting that they were probably formed within the black shale during the diagenetic process and prior to deformation. They have formed spherical aggregates of fine-grained anhedral pyrites (e.g. UMBS11) possibly replacing organic materials similarly to the process described by Taylor and Macquaker (2000). The diagenetic origin of this pyrite is also supported by the low As content which is relatively low in diagenetic pyrite compare to hydrothermal or metamorphic pyrite (Diehl et al., 2005).

During the major low-grade tectono-metamorphic event that affected the area, the aggregates of fine-grained anhedral pyrite in spherical nodules have been deformed into lenses parallel to the lamination (Steadman, 2015) and enriched in sulphide from the growth and annealing of pyrite by the hydrothermal fluids which were flown through crosscutting veinlets (Figure 9C). This should be the reason why sulphide-rich lenses are not present in the granitoid samples but more preponderant in mineralized black shale.

The subhedral to euhedral pyrite randomly distributed in the matrix have probably precipitated from the circulated hydrothermal fluid in the rock matrix (Basori et al., 2018; MacLean, 1991), or have most likely re-grown from retrograde cooling of pyrrhotite which, depending on temperature conditions, causes a drop in activity of sulphur accompanied by a decrease in sulphur content of pyrrhotite and the growth of pyrite of predominantly euhedral shape (Graham and Ohmoto, 1994; Craig and Vokes, 1993). The possible growth of pyrite from retrograde cooling of pyrrhotite is supported by the presence of pyrrhotite identified in the matrix of samples UMBS9 and UGR13, and which may have acted as the precursor of euhedral pyrite.

The distribution of elongated anhedral pyrite crystals in the form of short stringers have also precipitated from the circulated hydrothermal fluids into deformational structures (Diehl et al., 2005; Basori et al., 2018), formed during the tectonic, in the rock matrix. The aggregate of fine-grained anhedral pyrite in the granitoid matrix precipitated as well from the hydrothermal fluid (Basori et al., 2018).

The euhedral zoned pyrite within veins that crosscut the rock matrix might have resulted from the growth of early pyrite by the action of hydrothermal fluids circulating through the vein (McLean, 1991; Hammond and Tabata, 1997).

The fine-grained subhedral to anhedral crystals of pyrite disseminated along the vein selvedge have originated from the hydrothermal fluids circulating through the reactivated vein (Figure 29A)

and precipitated pyrite by fluid-wall rock interaction accompanied by host rock sulphidation (e.g. Figure 25A) and pressure fluctuation due to crack and seal responsible of fluid separation (Keith et al., 2018).

The massive sulphide bodies of pyrite have been formed by the precipitation and growth of pyrite from the circulated hydrothermal fluids in the vein through deformation structures acting as pathways (Diehl et al., 2005, Basori et al., 2018).

The arsenic incorporation into the pyrite may be related to the hydrothermal fluid, which commonly carries trace elements of As (Diehl et al., 2005), and also because As is commonly associated with the secondary pyrite of the Twangiza deposit.

The arsenopyrite is found in mineralized and unmineralized black shale, mineralized granitoid and hydrothermal vein samples. In mineralized black shale, it is found intergrown with pyrite, especially in sulphide-rich lenses and as fine-grained crystals as inclusions within pyrite (MBS1; MBS3A, Figure 36C and MBS3B, Figure 10C). It is also found as fine-grained crystals as inclusions within pyrite in mineralized granitoid (MGR17, MGR20). In unmineralized black shale, the arsenopyrite is either locally distributed in the matrix as fine-grained anhedral crystals (UMBS12B) or intergrowing with pyrrotite as euhedral medium-grained crystals (UMBS9, Figure 15E). In hydrothermal veins, it is found intergrowing with pyrite (HVN8, HVN19), as fine-grained crystals as inclusions in pyrite (HVN8, HVN19), and most importantly as coarse-grained massive sulphide bodies (HVN8, HVN19).

The arsenopyrite composition is uniform in all the sample types and textures with Fe content ranging from 33.44 to 35.20 wt. %, S content ranging from 21.13 to 22.55 wt. % and As content ranging from 42.20 to 43.97 wt. %. Nevertheless, the arsenopyrite may show minor concentrations of Ni, especially in the mineralized black shale and unmineralized black shale with 0.39 and 0.70 wt. % respectively.

The arsenopyrite might have been formed by precipitation from the hydrothermal fluid flow (Hammond and Tabata, 1997) into the deposit rocks. This is also supported by the fact that it is commonly found associated with pyrite textures and/or pyrrhotite that are referred to secondary pyrite originated from the hydrothermal fluids activity. Ni is commonly incorporated in the arsenopyrite from the hydrothermal fluid activity (Hammond and Tabata, 1997) and thus supporting the hydrothermal origin of the arsenopyrite. However, the Ni content in black shale

may also be related to the reducing conditions during the formation process, and with high pyrite and organic materials content as suggested by Zanin et al. (2017) for Ni, Mo and Co content in the black shale of Bazhenov Formation.

The pyrrhotite has been recognized in the unmineralized black shale, unmineralized granitoid and mineralized granitoid. It occurs as fine-grained anhedral patchy crystals randomly distributed in the matrix in unmineralized black shale (UMBS9, Figure 15C), whereas in unmineralized granitoid it occurs as aggregates of anhedral fine-grained crystals sparsely distributed in the matrix (UGR13, Figure 23D). In mineralized granitoid, the pyrrhotite is found as fine-grained crystal as inclusions within pyrite (MGR17). The pyrrhotite within the UGR has relatively higher concentration of Ni estimated at 2.06 wt. % than in unmineralized black shale and mineralized granitoid where the Ni is absent.

The pyrrhotite formed during prograde regional metamorphism as the pressure and temperature increased. The rock passed through a sulphur liberation window from early pyrite at moderate temperature and low pressures (450 - 500℃ and 0.3 – 1.0 GPa for pelites) which convert to pyrrhotite and release potentially considerable amounts of trace metals such as As and Au to the metamorphic fluids (Steadman, 2015). The pyrrhotite texture in the UMBS9 for instance suggests a hydrothermal fluid movement attested by the presence of patchy and slightly elongated crystals, probably in the direction of the fluid flow (Figure 15D), and the presence of a section rich in pyrrhotite with less carbon suggesting a leaching of carbon by the hydrothermal fluid and a section depleted in pyrrhotite with more carbon (Figure 15D&E). The presence of Ni in the pyrrhotite may be related to its preferential partitioning in pyrrhotite (Hammond and Tabata, 1997).

The chalcopyrite is always found as fine-grained crystals as inclusions within pyrite in mineralized (MBS3A, Figure 36C) and unmineralized black shale (UMBS4A), and mineralized granitoid (MGR17). The chalcopyrite composition does not significantly vary with the sample type and / or associated pyrite texture except in the unmineralized black shale where it shows an excess of Fe and a deficit of Cu for which the normalization to 4 ions gave respectively 1.28 and 0.67.

The chalcopyrite have also precipitated from the hydrothermal fluids flow (Hammond and Tabata, 1997, Basori et al., 2018), furthermore is associated with pyrite textures that evolved from the hydrothermal fluids activity.

The cobaltite is rare and has been only recognized in unmineralized granitoid occasionally disseminated in the matrix as anhedral fine-grained crystals (UGR13, Figure 47D). The cobaltite has minor concentrations of Ni (4.55 wt. %) and Fe (3.45 wt. %) in its structure.

This cobaltite precipitated from the hydrothermal fluid (Dolansky, 2007). The Co is a typical feature of high-temperature environment (Basori et al., 2018) and can provide information on the temperature of the hydrothermal fluid or can suggested that Co took place during the emplacement of the granitoid and subsequently formed cobaltite from the As-bearing sulphur rich hydrothermal fluid flow (Dolansky, 2007). This should be the reason why it has been only recognized in the granitoid sample. The occurrence of Co with pyrrhotite, which is assumed to be related to the hydrothermal fluid activity, emphasize also its precipitation from the hydrothermal fluids.

The gold grains are almost pure with about 97 wt. %, but often associated with lower contaminations of Fe (~1.15 wt. %). The native gold grains may have precipitated from the hydrothermal fluids in the pyrite interface area (Basori et al., 2018) which formed the trap.

The albite is found in the matrix of almost all sample types. It is associated with quartz in the black shale and hydrothermal vein samples, and with overgrowing dolomite, ankerite, siderite and magnesite in the granitoid samples. Its composition is uniform in all the sample types independently of the form of occurrence. In granitoid, it has the euhedral shape suggesting a recrystallization during the metasomatic process. The presence of albite in the overall deposit area, interpreted as a metamorphic phase (Deer et al., 1992), formed from the hydrothermal fluid which led to the albitization of the deposit and converted the intrusive rock to albitites (Saunders and Tuach, 1991). It attests to the low-grade metamorphism that affected the region.

Quartz is the major phase of the black shale's matrix samples and also constitutes the principal mineral of the hydrothermal veins. Most of the quartz veins crosscutting the black shale matrix show a comb texture suggesting a syntectonic formation from tensional type environment. The quartz vein is, however, usually fractured and overgrown by carbonates along the fractures (Figure 10B). This may suggests a late reactivation of the vein providing the pathway for the later hydrothermal fluids. The quartz in granitoid samples is rare or absent, suggesting that the original igneous rocks might have low quartz content such as monzodiorites or diorites and hence not strictly speaking granitoid, or most of quartz might have been altered by the hydrothermal fluids (e.g. MGR20) responsible for precipitation of albite and /or carbonates.

The carbonate consists mainly of dolomite, ankerite, siderite and magnesite. The black shales and albitites show abundant secondary carbonate that formed from hydrothermal influx of CO_2-rich fluids (Phillips and Brown, 1987), resulting in the alteration of the original assemblage and the precipitation of carbonates such as dolomite, ankerite, siderite and magnesite. A mantle source for the CO_2-rich fluid has been proposed in the past, but black shales are also considered as a possible source considering the high average C_{org} content of black shales, the proximity to known gold deposits and the negative $\delta^{13}C$ values measured in the carbonate alteration (Steadman, 2015). The albitites were more intensely overprinted by the alteration than the black shale, most likely due to their physical and chemical properties being more permeable and mineralogically reactive at the time of fluid influx.

Rutile is widespread in all deposit rock types. It is considered to have originated from low-grade metamorphism and / or of detrital origin (Craw et al., 2009).

Phlogopite is commonly found in dolostone, magnesium-rich limestone and ultramafic rocks (Anthony et al., 1990) which are not present in our study area. However, phlogopite might have precipitated in sulphide-rich lenses (where it has been widely recognized) from the CO_2-rich fluid influx by the reaction that mobilized Fe and stored it in the sulphides. After all Fe being consumed by sulphide precipitation, the remaining fluid precipitated phlogopite (Cui et al, 2003).

As far as native gold, visible at SEM scale, is concerned, sulphide-rich lenses may be considered as the most enriched texture in term of gold content in the mineralized black shale rocks. Here, gold has been found in spatial association with pyrite, typically along the interface of pyrite crystals (Figures 9E, 10E, 36C). Native gold grains has been also found associated with pyrite in the hydrothermal veins (Figure 28F). This suggests that gold was carried by the hydrothermal fluid and deposited in suitable traps formed by the sulphide-rich lenses and / or the massive sulphide bodies in the hydrothermal veins. The sulphide-rich lenses, which have formed from primary diagenetic pyrite, are randomly distributed in the black shales, and are likely to have formed from local sources. Hence gold found in these lenses may also not have moved far. The association of the gold with the hydrothermal fluid may also be supported by the high gold grade observed in the albitite rocks, from assay results (Table 1), where pyrite probably precipitated from the hydrothermal fluid along fractured zones.

Also some of the unmineralized black shale samples show evidence of hydrothermal fluid influx (e.g. UMBS4 and UMBS12). Their low gold grade can be explained either by few, or absence of, sulphide-rich lenses implying the absence of the mineralization's trap, or absence of reactivated veins which played the role of hydrothermal fluid pathways, and / or their gold content may have been leached (e.g. UMBS9) and deposited in ore zone by the hydrothermal fluid.

No primary pyrite has been identified in the studied albitite samples, and all pyrite in the albitite seems to be related to the hydrothermal fluid origin. Accordingly, since Au seems to be related to sulphide precipitation, also the gold in mineralized albitite may be of secondary origin, related to the mineralizing hydrothermal fluid. Some of the pyrite in the albitite might have been formed by retrograde cooling of pyrrhotite, especially within dilation zones providing the pathways for the hydrothermal fluid flow. Unmineralized granitoids show very little pyrite and are less fractured. This suggests that these granitoids, although heavily altered and albitised, were less accessible to the Au-mineralised S-rich fluids.

Moloto (2017) suggested from isotopic studies conducted on Twangiza deposit sulphides samples that gold might have been leached from sediments and concentrated into suitable traps to form the actual deposit, as some of the pyrite has a similar isotopic signature in veins and in authigenic/primary pyrite. Similarly, Büttner et al. (2016) proposed a sedimentary source the hydrothermal fluids system in the Kamituga and Lugushwa area. However, Walemba (2001) attributed the sulphur isotopic composition ($\delta^{34}S$ values in the interval of +1 to 3.4 ‰) to hydrothermal fluids resulted from magmatic source. The results of our study support that gold is associated with sulphide, especially pyrite. Furthermore, the sulphide-rich lenses' pyrite have derived from growth of primary diagenetic pyrite. There is no evidence whether the primary diagenitic pyrite is barren or contains some amount of gold. However, at the proposed pyrrhotite formation temperature and pressure (450 - 500℃ and 0.3 – 1.0 GPa for pelites), chlorite reach its terminal stability of hydrous mineral (Steadman, 2015). Simultaneous pyrite desulphurization and chlorite breakdown lead the fluids to become more sufficiently mobile to scavenge large amounts of H_2S, As, and Au from pyrite breakdown and may lead to the formation of gold deposit if deposited in a suitable structural trap (Steadman, 2015). This is supported by the fact that pyrrhotite has been commonly recognized in the unmineralized samples (e.g. UGR13 and UMBS9) where it is associated with the presence of a hydrothermal fluid movement features (Figure 15D). The sulphide-rich lenses have been thus enriched by the mineralizing hydrothermal fluid flow as

attested by the presence of the native gold (Figure 9E, Figure 10E) and the presence of crosscutting veinlets (Figure 9C) which acted as pathways. Hence, there is a probability that gold might has been leached from the sedimentary host rock by the carbonate fluid influx as attested by the presence of overgrowing carbonate in the reactivated quartz vein (e.g. Figure 10B) and the sulphide-rich lenses (Figure 9C), and redeposited it into trap areas, justifying the similarity of isotopic signature of veins and authigenic/primary pyrite investigated by Moloto (2017).

Regarding different sulphide textures and compositions, and considering the silicates, carbonates, and oxide phases associated with the sulphides in different samples and rock types of Twangiza Mine deposit, the following model is proposed for the understanding of the mineralizing phases of the deposit.

- The black shale sediments have been deposited in the area during the early Neoproterozoic period. Spherical nodules formed during this period and subsequently enriched in aggregates of fine-grained pyrite formed by replacement of organic materials.
- The granitoid rocks, consisting essentially of albitites, have intruded in the black shale rocks prior to the E-W compressive tectonic event (which occurred around 575 ± 83 Ma according to Walemba (2001)) which caused the formation of the main anticline structure (with the maximum deformation structures located in the hinge zone) that control the gold mineralization in the Twangiza deposit (Figure 6). This is supported by the fact that the albitites form sills which are folded together with the black shale host rocks and are intensively fractured in the anticline axial zone (Figure 5). The folding of sills indicates their pre-kinematic emplacement. The aggregates of diagenetic pyrite in spherical nodules were probably deformed during this period into sulphide-rich lenses. Deformation have changed the initially spherical pyrite aggregate shape to ellipsoidal shapes. Quartz was also precipitating during vein opening which led to the formation of quartz veins with comb structure (Figure 26B).
- The regional folding process have been followed by a low-grade metamorphism that affected the black shale and the granitoid sills. The hydrothermal fluid associated with the low-grade metamorphism of probably H_2O-NaCl±halite composition (Walemba, 2001) caused the alteration of the granitic assemblage to form albitite. The albitization was accompanied by the formation of the aggregate of fine-grained anhedral crystal in the host rock matrixes and the growth and annealing of fine-grained pyrite aggregated in lenses.

- Later on, the deposit formations were reactivated into strike-slip dominated tectonics from compressional thrust (Walemba, 2001), and due to the hydraulic fracturing, hydrothermal fluids pathways were created mainly in the hinge zone. Dilation zones were thus created in the anticline axial zone and quartz veins were fractured as attested by fractures cutting along the length of the veins and usually occupied by overgrowing carbonate (Figures 10B and 27C).
- The CO_2-rich hydrothermal fluids of H_2O-NaCl-CO_2±halite (522 ± 15 Ma according to Walemba (2001) composition circulated through the reactivated structures leading to the precipitation of anhedral to subhedral pyrite along the vein selvedge by wall-rock interaction, growth and zonation of pyrite in veins, elongated pyrite within deformation structures in the form of stringers, the massive sulphide bodies, arsenopyrite, chalcopyrite, rare cobaltite, and also caused the formation of pyrrhotite by sulphur liberation window from early aggregate of anhedral pyrite crystals in the rock matrix. The euhedral to subhedral pyrite in the host rock matrix probably formed later by retrograde cooling of pyrrhotite. Native gold grains precipitated from the hydrothermal fluid flow through crosscutting reactivated veins within the lens pyrite which constituted the trap area. In addition, abundant disseminated pyrite precipitated within albitite fractures, due probably to their chemical and physical properties such as brittleness and permeability. This is the reason why most of the pyrite found in the albitite appears to be associated with fractures. The pyrrhotite, cobaltite and rutile are stable at high temperature (Deer et al., 1992; Anthony et al., 1990) suggesting that the hydrothermal fluids from which these minerals precipitated was probably hot in nature ranging from 280^{o} to >450^{o} C according to Walemba (2001).
- The carbonation process took place from the hydrothermal influx of CO_2-rich fluids into the rock formations and led to the formation of dolomite, ankerite, siderite and magnesite which overgrow albite and quartz suggesting a late emplacement. However, the carbonation process in the Twangiza deposit might have been responsible of the mobilization and concentration of gold from the sedimentary host rocks (Boskabadi et al., 2017; Steadman, 2015) into the trap areas such as sulphide-rich lenses and the formation of hydrous silicates such as pyrophyllite, phlogopite, and some muscovite. The hinge zone

of the anticline axial zone constituted the preferential mineralization trap zone due to maximum fracturing therein.

Chuwa (2011) proposed a reduced intrusive-related gold deposit and orogenic gold deposit type for Twangiza deposit. However, according to the classification of orogenic gold deposits proposed by Groves et al. (1998), the following features can be pointed out in relation to the Twangiza deposit:

- It has been formed during compressional deformation processes at convergent plate margins in accretionary and collisional orogens resulted in the compressive movement which led to the folding of deposit formations;
- It is associated with deformed metamorphic terranes of Proterozoic age where gold is associated with low-grade metamorphic environment;
- Quartz is the dominant vein system with ~ 3% sulphide, though locally sulphide content may reach 30% of a 1 m core sample. Abundant carbonate minerals (dolomite, ankerite, siderite, and magnesite) are recognized in the deposit formations as well as albite and minor mica, chlorite and tourmaline. Sulphide mineralogy consist of pyrite, arsenopyrite and minor pyrrhotite and chalcopyrite;
- The hydrothermal alteration showing a lateral zonation from proximal to distal assemblage is recognized. The carbonate alteration include dolomite, ankerite, siderite and magnesite, whereas the alkali metamorphism include the albitization and sericitization;
- The structural control of the mineralization consists of second to third order structures near commonly large scale compressional structure consisting of the fold hinge zone.

Hence, based on the proposed model and the above mentioned features, an orogenic gold deposit type can be considered for the Twangiza deposit.

V. CONCLUSIONS AND RECOMMENDATIONS

The Twangiza Mine deposit sulphides consist of pyrite, arsenopyrite, pyrrhotite, chalcopyrite, and occasionally cobaltite.

The different types of pyrite textures identified in the Twangiza deposit consist of:

- aggregate of fine-grained anhedral pyrite crystals in spherical nodules recognized in the unmineralized black shale;
- aggregate of annealed anhedral pyrite crystals into sulphide-rich lenses recognized in mineralized and unmineralized black shale;
- distribution of elongated anhedral pyrite crystals in the form of short stringers in the unmineralized black shale, unmineralized granitoid and mineralized granitoid;
- aggregate of fine-grained anhedral crystal in the matrix of mineralized granitoid and unmineralized granitoid
- euhedral zoned pyrite crystals in veins which crosscut the mineralized black shale, unmineralized black shale, and hydrothermal veins;
- dissemination of abundant fine-grained subhedral to anhedral crystals of pyrite along the contact selvedge of the hydrothermal vein with the host rock;
- massive sulphide bodies of pyrite recognized in hydrothermal veins; and
- subhedral to euhedral fine-grained pyrite randomly distributed in the matrix of mineralized blackshale, unmineralized black shale, mineralized granitoid and unmineralized granitoid.

The composition of pyrite in the different textures and rock types is uniform with major elemental compositions ranging from 44.57 to 46.40 wt. % for Fe and 53.75 to 55.25 wt. % for S. However, the concentration of As is relatively higher (~ 1 wt. %) in mineralized black shale and hydrothermal veins than in other rock type samples.

The arsenopyrite commonly occurs as inclusions within pyrite in mineralized black shale, mineralized granitoid and hydrothermal veins, or intergrowing with pyrite in unmineralized and mineralized black shale, and in massive sulphide veins. The coarse-grained massive arsenopyrite bodies are recognized within massive sulphide veins where arsenopyrite is the most predominant sulphide. The composition of arsenopyrite is uniform in all rock types with Fe content ranging

from 33.44 to 35.20 wt. %, S content ranging from 21.13 to 22.55 wt. % and As content ranging from 42.20 to 43.97 wt. %. It shows, however, minor concentrations of Ni in the mineralized (0.39 wt. %) and unmineralized (0.70 wt. %) black shale rocks.

The pyrrhotite is sparsely disseminated in the rocks matrix of the unmineralized black shale and unmineralized granitoid. It is also rarely found as inclusion in pyrite in mineralized granitoid. The pyrrhotite shows minor concentrations of Ni (2.06 wt. %) in unmineralized granitoid whereas its composition is uniform in unmineralized black shale and mineralized granitoid.

Chalcopyrite is exclusively found as inclusion within pyrite, especially the secondary pyrite texture. Chalcopyrite composition does not vary significantly with the pyrite textures associated with and/or sample types.

The cobaltite is occasionally distributed in the granitoid matrix as fine-grained crystals associated with pyrrhotite. The cobaltite is enriched in Ni and Fe.

The aggregate of fine-grained anhedral pyrite in spherical nodules are interpreted as the primary diagenetic pyrite texture. This diagenetic pyrite formed during the diagenesis process following the sediments depositional period by replacement of organic materials. No primary pyrite texture has been identified in the granitoid samples. The aggregate of fine-grained pyrite into spherical nodules have been deformed into lenses parallel to the lamination during the deformation that caused the formation of the main anticline structure which controls the mineralization within the deposit. These lenses are crosscut by quartz veins with comb structures formed by precipitation of quartz during the vein opening.

The folding process were followed by a low-grade metamorphism associated with the hydrothermal fluid which led to the albitization of the deposit rocks and the precipitation of aggregate of fine-grained anhedral crystal in the host rock matrixes and the growth and annealing of fine-grained pyrite aggregated in lenses.

A second CO_2-rich hydrothermal fluid circulated later on within the rock deposit through reactivated structures, including quartz veins. This hydrothermal fluid have been responsible of the precipitation of elongated anhedral pyrite in the form of short stringers into deformational structures within the black shale and granitoid rocks, the growth and zoning of early pyrite into the hydrothermal veins and veins crosscutting the host rock matrix, dissemination of fine-grained

subhedral to anhedral pyrite along the hydrothermal vein contact selvedge in the host rock; coarse-grained massive pyrite and arsenopyrite bodies in hydrothermal veins, arsenopyrite and chalcopyrite as inclusions in pyrite, and cobaltite. Pyrrhotite resulted from the desulphurization of the aggregate of anhedral pyrite crystals in the host rock by these fluids and scavenged traces elements of As, Au etc. The euhedral to subhedral fine-grained pyrite in the host rock matrix resulted commonly from the retrograde cooling of the pyrrhotite.

The native gold grains have been recognized within the pyrite interface area. Gold have precipitated from the hydrothermal fluids and deposited into the pyrite interface area forming a suitable trap. However, the sediments which led to the formation of black shale might have been initially enriched in gold. Gold might have been mobilized from the sedimentary black shales by the CO_2-rich fluid influx and redeposited into the trap areas.

Additional work needs to be conducted in the area to complete this study in order:

- To analyze trace elements in the different pyrite textures, especially the gold concentration, by advanced reliable methods such as LA-ICPMS to evaluate whether the primary and secondary textures are enriched. This will help to understand whether the initial sediments were enriched in gold or not and whether gold have been leached from the sediments host rocks and concentrated into gold mineralization traps;
- To investigate the sulphur isotope signature of all the different sulphide textures of different rock types to decipher their origin;
- To specify the nature and the origin of carbonate-bearing fluids, the extent of the alteration and its implication for gold mineralization;
- To proceed on to the dating of zircon and monazite for the estimation of the age of the deposit.

REFERENCES

Altigani M.A.H., Merkle R.K.W., and Dixon R.D., 2016, Geochemical identification of episodes of gold mineralization in the Barberton Greenstone Belt, South Africa, *Ore Geology Reviews* 75, pp. 186 – 205.

Andras P. and Chovan M., 2005, Gold incorporation into sulphide minerals from the Tatric Unit, the Western Carpathians, with respect to their chemical composition, *Journal of Czech Geological Society*, pp. 143-144.

Anthony J.W., Bideaux R.A., Bladh K.W., and Nichols M.C., 1990, Eds., Handbook of Mineralogy, Mineralogical Society of America, Chantilly, VA 20151-1110, USA.

Banro Corporation, 2017, Investing in community development, Sustainability Report.

Banro, 2017, www.banro.com/operations/twangiza-mine (accessed 29/07/2017).

Basori M.B.I., Gilbert S., Large R.R., and Zaw K., 2018, Textures and traces elements composition of pyrite from the Bukit Botol volcanic-hosted massive sulphide deposit, Peninsular Malaysia, *Journal of Asian Earth Sciences* 158, pp. 173-185.

Björn S. Harðarson, 2014, Structural Geology of the Western Branch of East African Rift: Tectonics, Volcanology and Geothermal activity. Short Course IX on Exploration for Geothermal Resources, pp. 1-14.

Boskabadi A., Pitcairn I. K., Broman C., Boyce A., Teagle D.A.H., Cooper M.J., Azer M.K., Stern R.J., Mohamed F.H. & Majka J., 2017, Carbonate alteration of ophiolitic rocks in the Arabian–Nubian Shield of Egypt: sources and compositions of the carbonating fluid and implications for the formation of Au deposits, *International Geology Review*, 59:4, 391-419, DOI: 10.1080/00206814.2016.1227281, pp. 391-419.

Bureau d'Etudes Environnementales du Congo (BEEC), 2017, Etude d'impact environnemental Twangiza/Province du Sud Kivu.

Büttner S.H., 2012, Rock Maker: an MS Excel spreadsheet for the calculation of rock compositions from proportional whole rock analyses, mineral compositions, and modal abundance, *Mineralogy and Petrology* 104, pp. 129–135.

Büttner S.H., Reid W., Glodny J., Wiedenbeck M., Chuwa G., Moloto T. and Guscik A., 2016, Fluid sources in the Twangiza–Namoya Gold Belt (Democratic Republic of Congo): Evidence from tourmaline and fluid compositions, and from boron and Rb–Sr isotope systematics, *Precambrian Research* 280, pp. 161–178.

Cahen L., 1954, Géologie du Congo Belge, Liège : H. Vaillant-Carmanne SA., 575 p.

Chen T.T., Cabri L.J., and Dutrizac J.E., 2002, Characterizing Gold in Refractory Sulfide Gold Ores and Residues, *Journal Of the Minerals*, pp. 20-22.

Chuwa G. M., 2011, A review of gold deposits in the Twangiza-Namoya gold belt, eastern Democratic Republic of Congo, with emphasis on grass-root exploration models, MSc, Rhodes University, Grahamstown, South Africa, 184 p.

Craig J.R. and Vokes F.M., 1993, the metamorphism of pyrite and pyritic ores: an Overview, *Mineralogical Magazine*, Vol. 57, pp. 3-18.

Craw D., Upton P., and Mackenzie D.J., 2009, Hydrothermal alteration styles in ancient and modern orogenic gold deposit, New Zealand, *New Zealand Journal of Geology & Geophysics*, Vol. 52, pp. 11-26.

Cui X., Nabelek P.I. and Liu M., 2003, Reactive flow of mixed CO2–H2O fluid and progress of calc-silicate reactions in contact metamorphic aureoles: insights from two-dimensional numerical modeling, *Journal of Metamorphic Geology.*, 21, pp. 663-684.

Deblond A. (2013), Updated geological framework of central Africa, Geonet, Scientific case study n°7, Section 5, Annexe 3, African Museum Tervuren, 91p.

Deer W.A., Homie R.A. Zussman J., 1992, *An introduction to the rock-forming minerals, 2nd ed*. Prentice Hall. 696 pp.

Dewaele S., De Clercq F., Muchez P., Schneider J., Burgess R., Boyce A., Fernandez-Alonso M., 2010, Geology of the cassiterite mineralisation in the Rutongo area, Rwanda (Central Africa): current state of knowledge, *Geologica Belgica* 13/1-2, pp. 91-112.

Diehl S.F., Goldhaber M.B., Koenig A.F., Tuttle M.L.W., and Ruppert L.F., 2005, Concentration of Arsenic, Selenium, and other trace elements in pyrite in Appalachian coals of Alabama and

Kentucky; Paper presented at the 2005 National Meeting of the American Society of Mining and Reclamation, ASMR, 2005 pp. 283-301

Dolansky L.M., 2007, Controls on the genesis of hydrothermal cobalt mineralization: insights from the mineralogy and geochemistry of the Bou Azzer depsoits, Morocco, MSc, McGill University, Montreal, Canada, 162 pp.

Ebinger, C.J., 1989, Tectonic development of the western branch of the East African rift system, *Geological Society of America Bulletin*, 101, pp. 885-903

Fall H.G., 2007, Petrographic and chemical study of gold mineralization, Twangiza project, Company report, Banro Corporation.

Fleet M.E. and Mumin A.H., 1997, Gold-bearing arsenian pyrite and marcasite and arsenopyrite from Carlin Trend gold deposits and laboratory synthesis, *American Mineralogist*, Volume 82, pp. 182-193.

Graham U.M. and Ohmoto H., 1994, Experimental study of formation mechanisms of hydrothermal pyrite, *Geochimica et Cosmochimica Acta*, Vol. 58, No. 10, pp. 2187-2202.

Groves D.I., Goldfarb R.J., Gebre-Mariam M., Hagemann S.G., and Robert F., 1998, Orogenic gold deposits: A proposed classification in the context of their crustal distribution and relationship to other gold deposit types, *Ore Geology Reviews* 13, pp. 7-27.

Hammond N.Q. and Tabata H., 1997, Characteristics of ore minerals associated with gold at the Prestea mine, Ghana, *Mineralogical Magazine*, Vol. 61, pp. 879-894.

MacLean P.J., 1991, Characterization of pyrites from gold deposits, Phd, University of Western Ontario, 336p.

Moloto, T.R.P., 2017, Sulphur isotope study of pyrite from the Twangiza-Namoya Gold Belt, (South Kivu, DRC): a proxy of gold provenance, MSc, Rhodes University, Grahamstown, South Africa, 146p.

Phillips G.N., and Brown I.J., 1987, Host rock and fluid control on carbonate assemblages in the golden mile dolerite, Kalgoorlie gold deposit, Australia, *Canadian Mineralogist*, Vol.25, pp. 265-273.

Pohl W.L., 1994, Metallogeny of the northeastern Kibaran belt, Central Africa- Recent perspectives. *Ore Geology Reviews*, 9, pp. 105- 130.

Pohl W.L., Biryabarema M., and Lehmann B., 2013, Early Neoproterozoic rare metal (Sn, Ta, W) and gold metallogeny of the Central Africa Region: a review, *Applied Earth 66 Science* (Trans. Inst. Min. Metall. B), VOL 122 NO 2, pp. 66-82.

Rautenbach R., Bundo P., Pittuck M. and Sturgeon M., 2011, Preliminary assessment NI43-101, technical report, Banro Corporation.

Saunders C. M., Tuach J., 1991, Potassic and sodic alteration accompanying gold mineralization in the Rattling Brook Deposit, western White Bay, Newfoundland Appalachians. *Economic Geology*, Vol. 86 (3): pp. 555–569.

Steadman J.A., 2015, Banded iron formations, pyritic black shale, and gold deposits: A re-evaluation, PhD, University of Tasmania, Tasmania, Australia, 185p.

Tack L., Liegeois, J.P., Deblond, A. and Duchesne, J.C., 1994, Kibaran A-type granitoids and mafic rocks generated by two mantle sources in a late orogenic setting (Burundi), *Precambrian Research*, 68, pp. 323-356.

Tack L., Wingate M.T.D., Dewaele B., Meert J., Belousova E., Griffin B., Tahon A., and Fernandez Alonso M., 2010, The 1375Ma "Kibaran event" in Central Africa: Prominent emplacement of bimodal magmatism under extensional regime, *Precambrian Research* 180 pp. 63–84.

Takeshi K. and Ohmoto H., 1999, Sulphur isotope evidence for the origin of 3.4 to 3.1 Ga pyrite at the Princeton gold mine, Barberton Greenstone Belt, South Africa, *Precambrian Research*, 96 (3-4), pp. 209-224

Taylor K.G. and Macquaker J.H.S., 2000, Early diagenetic pyrite morphology in a mudstone-dominated succession: the Lower Jurassic Cleveland Ironstone Formation, eastern England, *Sedimentary Geology* 131, pp. 77–86.

Tibane L.V., 2013, The characterizations of pyrite from the Ventersdorp Contact Reef of the Kloof Gold Mine in the Witwatersrand Bassin in South Africa, MSc, University of Pretoria, Pretoria, South Africa, 164 p.

Villeneuve M., 1987, Geologie du synclinal de l'Itombwe (Zaire oriental) et le probleme de l'existence d'un sillon plisse pan-africain, *Journal of African Earth Sciences*, Vol. 6, No. 6, pp. 869-880.

Walemba K.M.A., 2001, Geology, geochemistry, and tectonometallogenic evolution of Neoproterozoic gold deposits in the Kadubu Area, Kivu, Democatic Republic of Congo, PhD, University of Witwatersrand, 491pp.

Walemba K.M.A. and Master S., 2005, Neoproterozoic diamictites from the Itombwe Synclinorium, Kivu Province, Democratic Republic of Congo: Palaeoclimatic significance and regional correlations, *Journal of African Earth Sciences* 42, pp. 200–210.

Zanin N. Yu., Zamirailova A. G., and Eder V. G., 2017, Nickel, Molybdenum, and Cobalt in the Black Shales of the Bazhenov Formation of the West Siberian Basin, *Geochemistry International*, Vol. 55, No. 2, pp. 195–204.